SCUOLA DI DOTTORATO
UNIVERSITÀ DEGLI STUDI DI MILANO-BICOCCA

Department of Materials Science

PhD program in Materials Science and Nanotechnology Cycle: 35

Atomistic simulations of Ge-rich GeSbTe alloys for phase change memories

Surname: Abou El Kheir Name: Omar

Registration number: 786168

Tutor: Prof. Marco Bernasconi

Coordinator: Prof. Marco Bernasconi

2021/2022

Università degli studi di Milano-Bicocca

Department of Materials Science
PhD program in Materials Science and Nanotechnology

Atomistic simulations of Ge-rich GeSbTe alloys for phase change memories

Supervisor:
Prof. Marco Bernasconi

Candidate:
Omar Abou El Kheir

Academic Year
2021-2022

Contents

Introduction

In this thesis, we have studied the structural and functional properties of GeSbTe (GST) alloys by means of atomistic simulations. These alloys belong to the class of phase change materials which have been employed for data storage applications such as rewritable optical disks (CD-RW, DVD-RW) since the '90 and more recently in electronic non-volatile memories named Phase Change Memories (PCM) [1, 2, 3]. These applications rely on the ability of chalcogenide alloys to switch rapidly and reversibly between the crystalline and the amorphous phases upon heating. The two phases differ in their optical and electrical properties which allows encoding binary a information. The switching operation is induced by laser pulses in optical disks or current pulses in electronic memories. The crystalline low resistance phase corresponds to the 1-bit state of memory which turns into the amorphous upon proper heating in the RESET operation. On the contrary, the SET operation consists of the phase transition from the amorphous high resistive phase (0-bit) to the crystalline one.

Non-volatile electronic memories based on phase change materials gained increasing attention in the early 2000s as a consequence of some limitations of the flash memories at that time and due to several advantages that PCMs offer, such as fast programming time, high reliability, superior cycling endurance and easy integration in microelectronics based on silicon.

The material of choice for PCMs is the $Ge_2Sb_2Te_5$ (GST225) compound which can be seen as a pseudobinary alloy on the GeTe-Sb_2Te_3 tie-line. Memories based on this alloy have already reached the global market. Indeed, in 2017 Intel and Micron have commercialized 3D cross-point standalone memories based on GST225 [4]. PCMs are also of interest for embedded memories applications for which we can envisage a very huge market ranging from internet of things to automotive applications. However, the crystallization temperature (T_x) of GST225, around 420 K, is too low for embedded-memories applications of interest for the automotive sector, which requires a higher operating temperature with respect to standalone applications.

To improve data retention at high temperatures of embedded PCMs several approaches have been proposed, such as doping GST225 with nitrogen or carbon, exploring other ternary alloys (InSbTe, InGeTe and GaSbTe) or

tuning the composition of GST alloys by increasing the content of Sb or Ge [5, 6, 7, 8, 9, 10]. Embedded memories based on Ge-rich GST alloys have already reached an advanced stage of development. A high-density embedded PCM on the 28 nm technological node has been demonstrated to be viable for automotive microcontroller applications [11].

It was shown that by increasing the fraction of Ge, T_x can be raised above 600 K [12]. The raise in the crystallization temperature has been ascribed to phase separation into Ge and a less Ge-rich GST alloy upon crystallization [13]. This phase separation enhances data retention but comes with some drawbacks such as an electrical resistance drift with time of the SET state and a high cell-to-cell variability [14]. In order to mitigate these drawbacks, a better understanding than currently available of the mechanism underlying the phase separation process is required. In this respect, atomistic simulations based on density functional theory (DFT) could provide useful insights on the properties of Ge-rich GST alloys as occurred for the stoichiometric GST225 compund [15, 16, 17, 3].

On these premises, in this thesis work we carried out a systematic study of the properties of Ge-rich GST alloys based on DFT calculations. We have first investigated the local structure of the amorphous phase of Ge-rich GST alloys as a function of Ge content by generating amorphous models for selected different compositions by quenching from the melt. Then, we investigated the thermodynamics of the possible decomposition channels of Ge-rich GST alloys. To this end, we used high-throughput DFT methods to explore the full ternary Ge-Sb-Te phase diagram. This comprehensive analysis allowed us to assign to each GST alloy a decomposition propensity based on DFT thermochemical data. This information, combined with the knowledge of the structural properties of the amorphous phase, allowed us to devise a possible strategy to tune the composition in order to limit the segregation of Ge by still keeping a high T_x.

This work on the Ge-rich GST alloys has been carried out within the European project BeforeHand (Boosting Performance of Phase Change Devices by Hetero- and Nano-Structure Material Design). The theoretical results on the decomposition pathways and the electrical properties of the amorphous phase have been compared with experimental data from other partners of the project.

Hitherto, we have introduced our approach to the study of the decomposition reactions of Ge-rich GST alloys based only on thermodynamics. However, kinetic effects related to the segregation of Ge might strongly affect the products resulting from of the decomposition process. The atomistic molecular dynamic simulation of such a complex process requires runs several ns long for several thousands of atoms, which is far beyond the reach of DFT methods. A possible route to overcome these limitations is the development of

reliable classical interatomic potentials. Behler and Parrinello have introduced a framework to develop high-dimensional interatomic potentials with close to ab-initio accuracy by employing artificial neural networks (NN) fitted on a DFT database [18]. This scheme was demonstrated to be suitable to describe the complexity of the chemical bonding in phase change materials such as GeTe [19] and Sb [20]. The direct simulations of the crystal nucleation and growth of GeTe and Sb based on NN potential were indeed reported in previous works [20, 21, 22].

In the perspective to extend this scheme to Ge-rich GST alloys, we developed a NN interatomic potential for the ternary compound GST225 by fitting a huge DFT database with the DeepMD code [23, 24]. The NN potential has been validated on the structural, dynamical and vibrational properties of liquid, crystalline and amorphous phases of GST225. We have then employed the NN potential to study the kinetics of homogeneous and heterogeneous crystallization in the supercooled liquid with supercells containing up to 12000 atoms for a few tens of ns which allowed us to estimate the crystal growth velocity in a wide range of temperatures. These results demonstrated the possibility to devise a reliable and computationally viable NN potential for a complex system such as GST225. This achievement represents a very crucial step toward the development of NN interatomic potential for Ge-rich GST alloys that will allow shedding light on the kinetics of the crystallization of these alloys by atomistic simulations.

The thesis is organized as follows. In Chapter 1 an overview of phase change materials and memories is provided. Chapter 2 is devoted to the theory and computational methods employed in this work. The results on the structural properties of the amorphous phase of Ge-rich GST alloys and the study of the decomposition reactions in the ternary phase diagram are reported in Chapter 3 while Chapter 4 is devoted to the development of the NN interatomic potential for GST225 and its application to the study of the crystallization process.

Chapter 1

Phase change materials and memories

In this chapter, an overview of phase change memories (PCMs) will be provided in the first section, followed by a section on the structural properties of the prototypical GeSbTe compounds on the GeTe-Sb_2Te_3 tie-line used in PCMs and finally, in the last section, we will discuss properties of Ge-rich GST alloys proposed for embedded memories applications refining a crystallization temperature higher than those achievable for stoichiometric GST alloys.

1.1 Overview

Phase change materials, typically consisting of chalcogenides alloys, are of keen interest for applications in optical discs (CD-RW, DVD-RW, DVD-RAM and Blue Rays) [25, 26] and electronic non-volatile memories named Phase Change Memories (PCMs) [1, 27, 28]. Both applications rely on a very rapid ($\sim$ 50 ns) and reversible transformation between the crystalline and amorphous states of phase change materials induced by heating via laser irradiation in the optical discs or the Joule effect in PCMs. The two logical states correspond to the two phases which are distinguishable thanks to the large contrast in their electrical resistivity (in PCMs) and optical reflectivity (for DVDs). Roughly speaking, the amorphous phase is insulating while the crystal is metallic, or to be more precise the amorphous phase is an intrinsic semiconductor while the crystal is a degenerate semiconductor for the reasons that will be discussed later on. The history of this technology dates back to the seminal work of Ovshinsky [29] in the '60s in which the author suggested to employ amorphous chalcogenides for data storage applications. This innovative idea captured the attention of researchers looking for recordable video discs. Initially, the development was slow and has been interrupted several times. In the late '80s, Yamada and co-workers [25] found very promising materials for data storage applications in the GeSbTe (GST) phase diagram which broadened the perspectives for the realization of these technologies. The amorphous phase of the alloys discovered by Yamada displays ideal properties for optical storage applications [30], such

as high thermal stability at room temperature and rapid crystallization with large optical changes upon laser irradiation. Afterwards, and in a very short time, optical discs based on $Ge_2Sb_2Te_5$ (GST225) were commercialized. Since then, GST225 has been the prototypical phase change material which attracted most of the efforts in the field. More or less at the same time when optical discs based on GeSbTe alloys entered the global market, the limitation in the scaling down of non-volatile memories technologies opened the route to the investigation of new technologies with high cell density, higher speed time and CMOS compatibility [31]. In this respect, phase change materials had already been proposed for electronic non-volatile memories since the '70s [32]. However, the programming time and programming energy at the actual technological nodes in the '70s were not competitive with silicon-based devices. In the early 2000s, the advance in materials exploration and the dramatic shrinking of the technological node, together with the need for new non-volatile memories, made PCMs an interesting new technology to be explored.

A PCM device is essentially a resistor of a GST alloy (active material) inserted between two electrodes (see Fig. 1.1). The phase transition occurs in a small portion of the active material which is heated by a heater located below the active zone due to electrical pulses induced by applying a bias between the two electrodes. The "0" logical state of the memory is encoded in the amorphous phase while the "1" logical state is encoded in the crystalline one. Readout of the memory consists of measuring the resistivity of the cell at low voltage which allows discriminating the logical state thanks to the difference of almost three orders of magnitude in the electrical resistivity. The cell programming consists of either the amorphization of the crystal (RESET process) or the recrystallization of the amorphous phase (SET process), see Fig. 1.2.

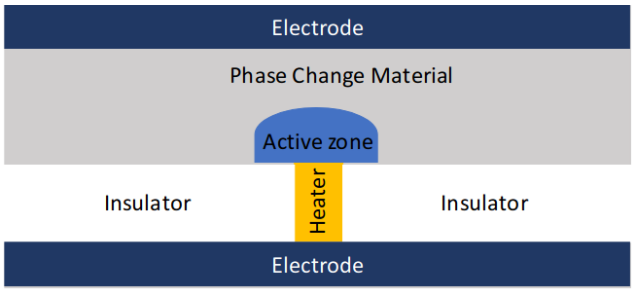

Figure 1.1: Cross section of a PCM memory cell in the so-called mushroom architecture. The cell consists of an active layer of a phase change material inserted between two electrodes. Upon electrical pulses, only a small portion (active zone) undergoes the phase transformation due to Joule heating.

In the RESET operation, the active region initially in the crystalline state is heated above the melting temperature (T_m) with a very short and intense electrical pulse (see Fig. 1.3). Only a small region of the active material melts upon heating giving rise to a huge temperature gradient inside the memory cell. The temperature gradient leads to high cooling rates and as a consequence, the temperature drops in a very short time, which hinders the crystallization and leads to the formation of the amorphous phase. In the reverse process (SET operation), the recrystallization of the amorphous phase is achieved by raising the temperature above the glass transition temperature (T_g) where the atomic mobility is high enough to allow for crystal nucleation and growth in a few tens of nanoseconds. To this aim, a longer and less intense electrical pulse is required as shown in Fig. 1.3.

The SET operation is possible at viable voltages thanks to a peculiar non-linear current-voltage (I-V) characteristics of GST alloys shown in Fig. 1.4. Should the amorphous phase behave as an ohmic resistance with an electrical resistivity of the order of $M\Omega$, one would need to apply a bias as large as 500 V to induce an electrical current of 0.5 mA used for recrystallization. GST alloys overcome this problem due to the presence of an electronic transition to a high conducting state beyond a threshold voltage (V_{th}) of the order of few Volts. This threshold switching is also named Ovonic switching after the name of Ovshinsky.

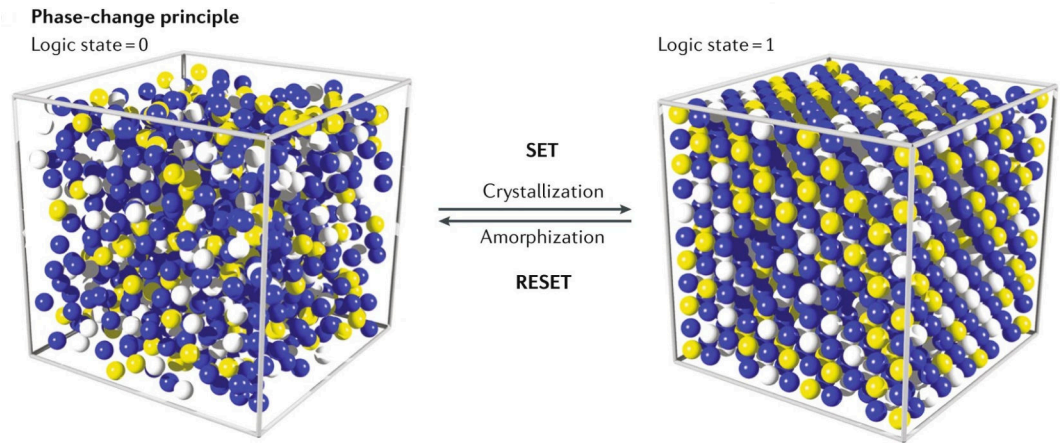

Figure 1.2: The two programming operations of PCM consist of the crystallization of the amorphous phase (SET operation) or the amorphization of the crystalline phase (RESET operation). This figure is taken from [3].

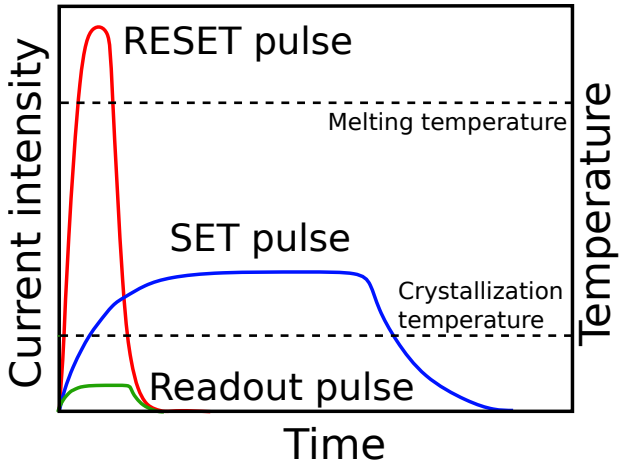

Figure 1.3: The profile of the electrical pulses used for the switching of PCM cells. A fast and intense pulse leads to the melting of the crystal and then to the amorphization of the active zone (RESET) while a longer and less intense pulse leads to recrystallization of the amorphous phase (SET).

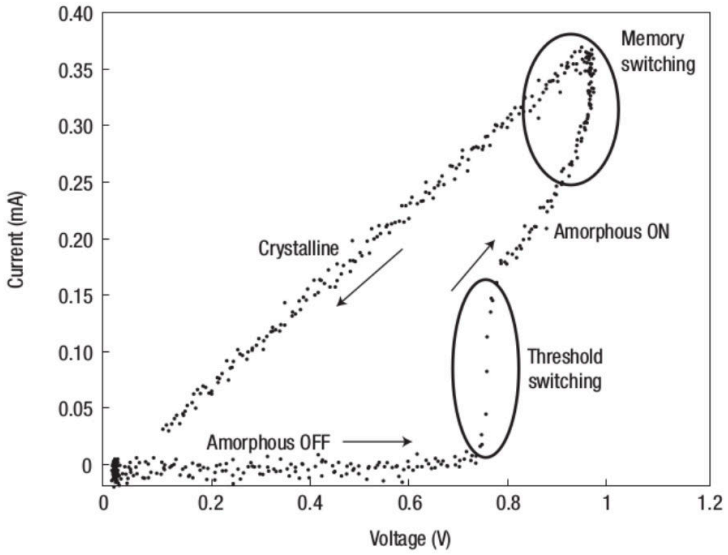

Figure 1.4: Typical I-V curve of phase change materials. Starting in an amorphous phase, upon applying a small voltage only low current flows through the material. Once the applied voltage reaches a threshold voltage of the order of a Volt, the electrical resistance undergoes an abrupt drop and the current increases promoting the crystallization due to Joule heating. Instead, the crystalline phase is metallic and exhibits a low Ohmic resistance. Figure taken from [1].

PCMs, based on GST alloys, feature a writing speed close albeit lower than that of the dynamic random access memories (DRAM) and much higher than that of FLASH memories, namely, 50 ns for PCMs against 1-100 μs for Flash

and 10 ns for DRAM. Besides that, PCMs have better endurance, cycling and scaling properties with respect to FLASH memories. All these features allowed PCMs to enter the global market of memories. The first commercialization was made by Numonyx in 2012 [33] for the cellular market with devices at 45 nm technological node. In 2017, Intel and Micron announced a product based on a 3D XPoint^{TM} technology with commercial name Optane^{TM} and Quantx^{TM}. A reverse engineering study [4] showed that these memories are based on GST225. 3D XPoint^{TM} technology belongs to the so-called storage class memories (SCMs) [34], which are capable of combining non-volatility with a speed close to that of DRAMs as shown in Fig. 1.5. Indeed, the 3D XPoint^{TM} memories are slightly slower than the DRAMs, but they exhibited a storage capacity up to 1Tb at a lower cost than DRAMs, at least in 2018. Further improvements in the performance of PCMs for applications in SCM are underway. For instance, subnanosecond switching of PCMs was achieved very recently [35]. Finally (and for completeness), one should highlight the fact that PCMs are not the only candidate for this kind of application (SCM) and for the replacement of flash memories. Several other technologies are under investigation, such as resistive-switching oxides [36, 37], spintronic technology [38, 39], ferroelectric materials [40, 41] and others [42, 43, 44, 45]. However, only PCMs technology among those listed above has reached the maturity and the stage to enter the market.

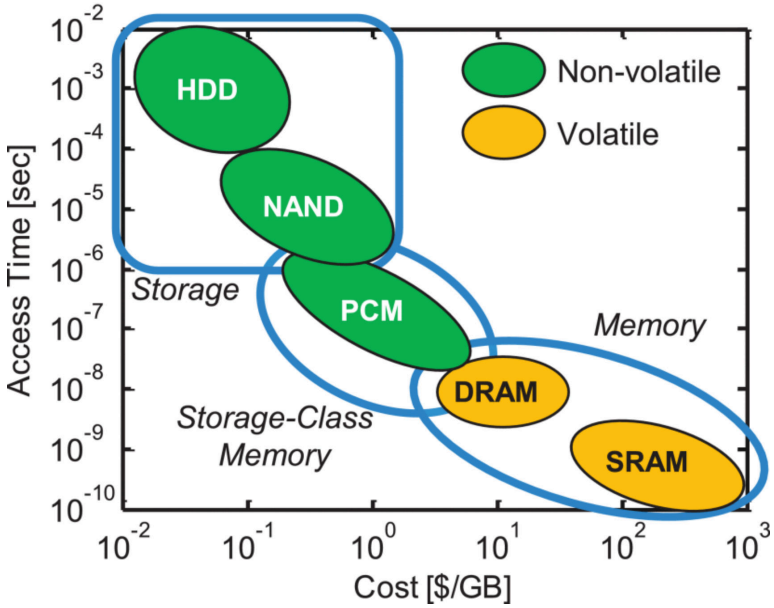

Figure 1.5: Map of the memory hierarchy based on the access time versus the production cost. The wide gap of performance between NAND FLASH memories and DRAM can be filled by the new class of memories known as storage class memory (SCM) which are based on PCMs. Figure taken from [34].

PCMs are of interest also for neuro-inspired computing. Nowadays, computers are based on the so-called von Neumann architecture in which the memory unit is separated from the processing unit. Every time a piece of information is processed it must be moved to the central processing unit (CPU) and then back to the memory unit. Time and energy used for this data exchange are now becoming the bottleneck for further improvement of the performances of computing devices. In this respect, neuro-inspired computing [46, 47, 48, 49] is a promising technology to overcome this limitation by unifying the processing and storage units into a single unit [42]. Neuro-inspired computing was achieved with PCMs devices by realizing the counterpart of biological neurons [50] and synapses [51, 52]. The integrate-and-fire behaviors of the biological neuron can be accomplished by the gradual crystallization of the active region in PCMs while the dynamical stochasticity of neurons can be achieved by the intrinsically stochastic crystallization behavior of GST alloys [53] controlled by a sequence of electrical pulses. Also, plastic synapses were realized thanks to the continuous nonlinear transition in the resistive state of PCMs devices which mimic the synaptic weight.

As already mentioned the alloy mostly used for PCMs is the GST225 compound, which displays a good compromise between the stability of the amorphous phase (at room temperature) and the crystallization speed. GST225 can be seen as an alloy on the $(GeTe)_m(Sb_2Te_3)_n$ tie-line in the ternary phase diagram as shown in Fig. 1.6. By changing the composition it is possible either to increase the crystallization speed by moving toward the Sb-Sb_2Te_3 tie-line at the expense of a lower thermal stability of the amorphous phase, or to raise the crystallization temperature by increasing the fraction of Ge. For instance, amorphous Sb is known to recrystallize extremely fast even at room temperature, while the crystallization temperature (T_x) of Sb_2Te_3 is around 360 K to be compared to that of GST225 which is of the order of 420 K.

In the last years, PCMs were investigated also for higher temperatures applications of interest for the automotive sector. This kind of application requires T_x higher than that of GST225 to ensure data retention at 450 K for ten years. Materials exploration provided several options to raise T_x such as using InSbTe, InGeTe or GaSbTe alloys [5, 6, 7], light doping GST225 with N, O [8], carbon doped GeTe [9] and Sb-/Ge-rich GST alloys [10]. All these alloys display higher T_x than GST225 to provide a better data retention thanks to the higher stability of the amorphous phase.

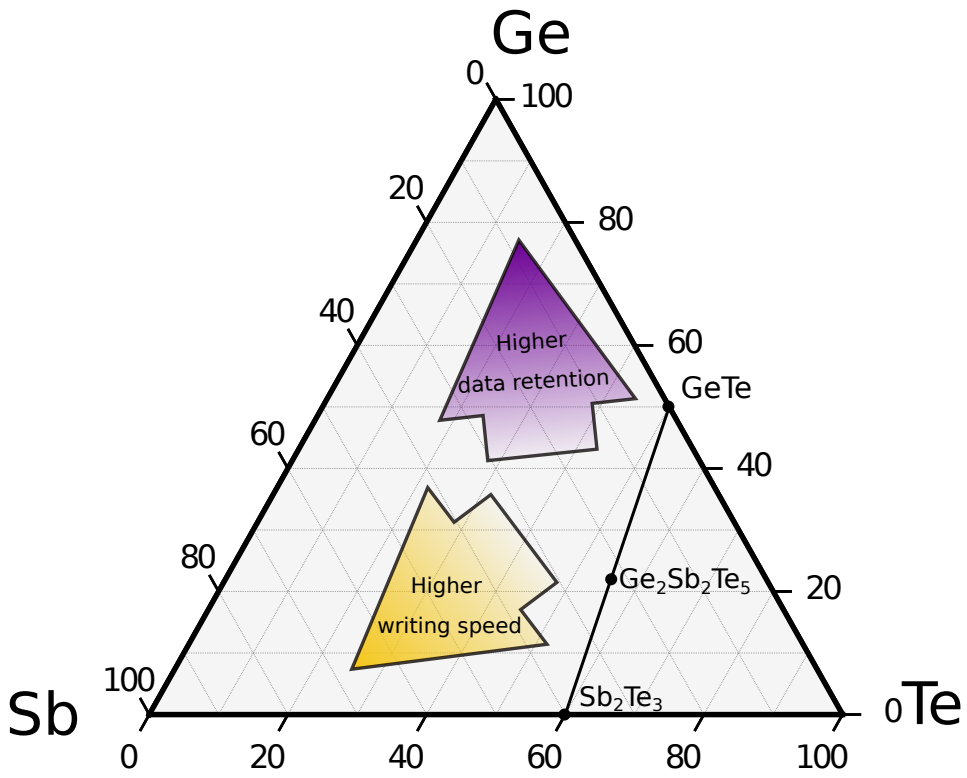

Figure 1.6: The GeSbTe ternary phase diagram highlights the compositions for PCMs with higher data retention and those with higher programming speed.

1.2 Structural properties of GeTe-Sb_2Te_3 pseudo binary phase change alloys

We here focus on the structural properties of pseudo-binary GeTe-Sb_2Te_3 alloys which encompass the GST225 composition mostly exploited in PCMs. For the sake of comparison, we first illustrate the crystalline structure of GeTe and Sb_2Te_3 parents compounds.

GeTe is the first phase change material discovered and suitable for PCMs. GeTe crystallizes in two crystalline phases. At normal pressure and temperature below 700 K, the stable structure is the rhombohedral phase (space group $R3m$) known as α-phase. α-GeTe contains two atoms per unit cell that can be seen as a distorted rocksalt geometry with a displacement of the Te atom, giving rise to GeTe bilayers stacked along the [111] direction of the original cubic phase which turns into the c-axis of the trigonal phase. The experimental lattice parameters are a = 4.31 Å and α = 57.9 ° [54]. In this crystalline phase, Ge forms three short GeTe intrabilayer bonds (2.84 Å) and three longer interbilayer GeTe bonds (3.17 Å). The rhombohedral phase can be represented in a hexagonal unit cell containing three formula units stacked along the c direction and separated by the long bonds. The atoms follow a stacking sequence

similar to that of FCC structure (i.e. ABCABC...). The rhombohedral and hexagonal cells of the α-phase are shown in Fig 1.7.

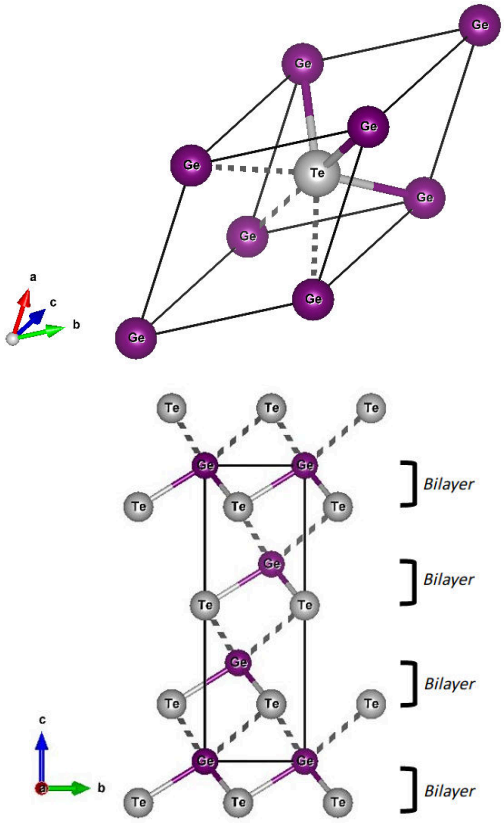

Figure 1.7: The primitive rhombohedral unit cell of α-GeTe (top) and the conventional hexagonal unit cell (bottom). Short and long bonds are depicted by solid and dashed lines. Ge and Te atoms are depicted by violet and grey spheres.

The α-phase undergoes a ferro-paraelectric transition at around 700 K. The resulting β-phase has a NaCl structure (space group $Fm\bar{3}m$) with a lattice parameter a=5.998 Å [55]. Extended X-Ray Absorption Fine Structure (EXAFS) measurements revealed that in the β-phase, Ge keeps a local 3+3 bonds environment with, however, a random orientation which destroys the ferroelectric order [56]. The β-phase of GeTe is the crystalline phase relevant for the operation of PCMs because this is the crystalline phase the amorphous transforms into during the SET operation.

GeTe lies in the zone of the phase diagram which exhibits relatively high data retention at room temperature. On the other side of the GeTe-Sb_2Te_3 tie-line, we find Sb_2Te_3 which instead displays lower data retention but higher programming speed (see Fig. 1.6).

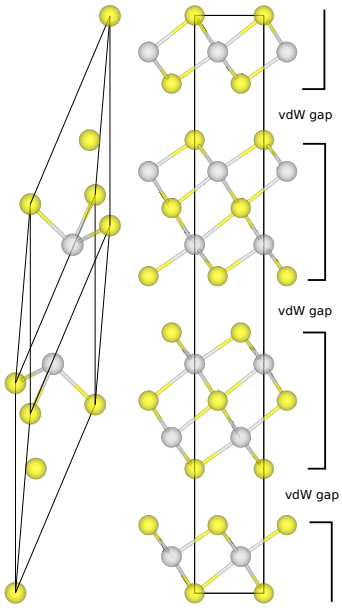

Figure 1.8: The primitive rhombohedral unit cell of Sb_2Te_3 (left) and conventional hexagonal unit cell (right) where three formula units are stacked along the c-direction and separated by weak Te-Te contacts. Short and long bonds are depicted by solid lines. Sb and Te atoms are depicted by yellow and grey spheres.

Sb_2Te_3 crystallizes in a rhombohedral structure (space group $R\bar{3}m$) with five atoms per unit cell. The experimental lattice parameter are a = 10.44688 Å and $\alpha = 23.5513$ ° [57]. Similarly to α-GeTe, Sb_2Te_3 can also be represented in a hexagonal unit cell containing three slabs of five atoms each stacked along the c direction and separated by a wide Te-Te vdW gap (Fig.1.8). The atoms are stacked along the c direction in an ABCABC sequence. In this structure, Sb is six-fold coordinated by Te forming three short (2.979 Å) and three slightly longer (3.168 Å) bonds similarly to Ge in α-GeTe. Moreover, there is a weak Te-Te contact 3.736 Å long across the vdW gap. Very recently, a metastable rocksalt phase of Sb_2Te_3 with one vacancy per formula unit on the cationic sites was found experimentally [58]. In this phase, the anionic sublattice is fully occupied by Te while Sb and vacancies occupy the cationic one.

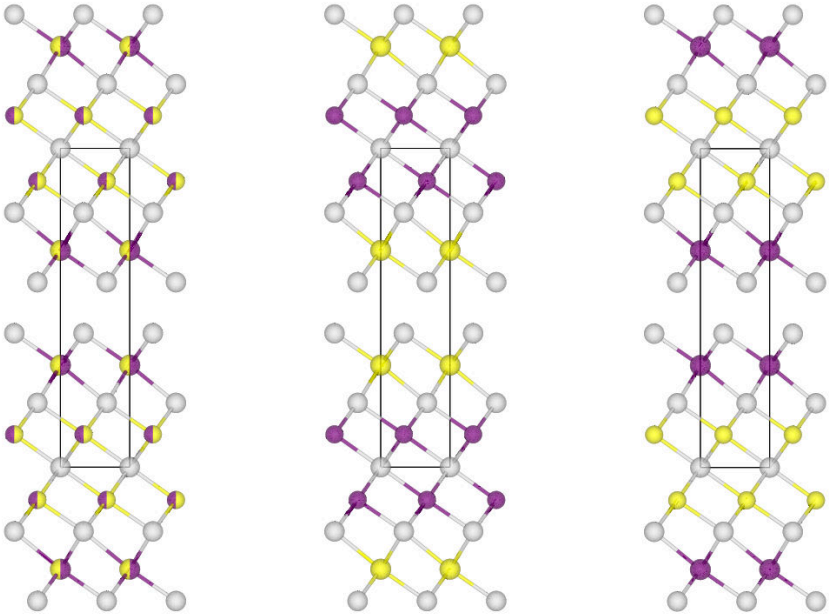

Figure 1.9: The hexagonal structure of $Ge_2Sb_2Te_5$ and the occupation sequences suggested in the literature. From the left: Matsunaga [59], Petrov [60] and Kooi model [61]. Ge, Sb and Te atoms are depicted by violet, yellow and grey spheres. In the model proposed by Matsunaga, Sb and Ge are distributed randomly in the cationic sublattice.

GST225, which is a pseudobinary compound on the GeTe-Sb_2Te_3 tie-line, displays a stable rombohedral phase and a metastable cubic phase similarly to the parent compounds. In the stable phase, GST225 has a hexagonal primitive unit cell (space group $P\bar{3}m1$) with 9 atoms stacked along the c-direction. Along the c-direction, each 9 atoms (formula unit) form a slab separated from adjacent slabs by a long weak Te-Te contact. The stacking sequence of atoms within the slab is again ABCABC. Several occupation sequences of the cationic sublattices have been proposed experimentally as shown in Fig. 1.9. The experimental lattice parameters due to Matsunaga [59] are a = 4.224 Å and c = 17.2391 Å. DFT calculations showed that the energetically most stable stacking sequence is the one proposed by Kooi. Although, the sequence suggested by Matsunaga is slightly higher in energy, the difference with Kooi is of the same order of the contribution of configurational entropy to the free energy at 300 K [62]. GST225 also displays a cubic NaCl metastable phase with 20% of vacancies on the cationic sublattice. Actually, the cubic phase is the relevant one for the operation of the memory [30] as it is the case for GeTe. The experimental lattice parameter of the metastable structure is a= 6.0293 Å [59]. XRD measurement showed that vacancies, Ge and Sb occupy randomly the cationic sublattice while the anionic sublattice is fully occupied by Te [59]. Similarly to GeTe, Ge in cubic GST225 displays locally 3+3 geometry with short and long bonds.

Concerning the amorphous phase of $Ge_2Sb_2Te_5$, EXAFS analysis [63, 64, 65, 66] revealed that Ge atoms are four-fold coordinated in amorphous GeTe and GST225, in contrast with the six-fold coordination typical of the crystalline phase. Although a four-fold coordinated Ge atom immediately suggests a tetrahedral coordination, reverse Monte Carlo (RMC) analysis of x-ray diffraction data on amorphous GST225 have been achieved [67] without including tetrahedral Ge. However, later XANES measurements supplemented with DFT calculations identified a typical edge that has been assigned to tetrahedral Ge [68].

In this respect, first principles Molecular Dynamics (MD) simulations provided helpful insights into the structure of the amorphous phase. Models of amorphous phase obtained by quenching the melt in few tens of ps revealed the coexistence of tetrahedral and defective octahedral-like structures [15, 16, 69, 70, 17]. Moreover, the analysis of these models indicates the presence in the amorphous phase of Ge-Ge, Sb-Sb and Ge-Sb bonds that were called "wrong bonds" because they are not present in the crystal. The presence of homopolar/wrong bonds can be seen in the partial radial distribution functions in Fig. 1.10 and from the average coordination number for each bond type in Tab. 1.1 taken from Ref. [70]. The distributions of coordination number (see Fig. 1.10) show also that Te atoms are three-fold coordinated while Ge, as well as Sb, are mainly four-fold coordinated. However, only one-third of Ge atoms are in a tetrahedral environment. The remaining fraction of four-coordinated Ge as well as all four-coordinated Sb atoms are in a defective octahedral-like environment with bond angles typical of the octahedral geometry, but coordination lower than six. Three-fold coordinated atoms (Ge, Sb, and Te) have a pyramidal bonding geometry (see Fig. 1.11). It was shown that the tetrahedral configuration of Ge atoms is favored by Ge-Ge bonds [70, 71].

Turning to the medium-range order, amorphous models generated with molecular dynamic simulations showed that four-membered rings are the most abundant in the amorphous phase of GST225 (Fig. 1.12) [69, 70, 17]. Most of these rings are of the ABAB type (where A is Ge or Sb and B is Te) which is the building block of the cubic crystalline phase. It was shown that four-membered rings survive in the supercooled liquid phase above the glass transition temperature (T_g) and they act as nucleation sites for the formation of cubic crystallites [3, 17]. For instance, highly ordered and connected four rings from a snapshot of the liquid are shown in Fig. 1.13. It was also proposed that the presence of nanocavities would favor the reorientation of four-membered rings promoting the formation of crystalline nuclei [69]. Direct DFT simulations of the crystallization of the amorphous phase of GST225 shed light on the kinetics of formation of critical nuclei and crystal growth [17, 72, 73]. More about crystallization will be discussed in the following section.

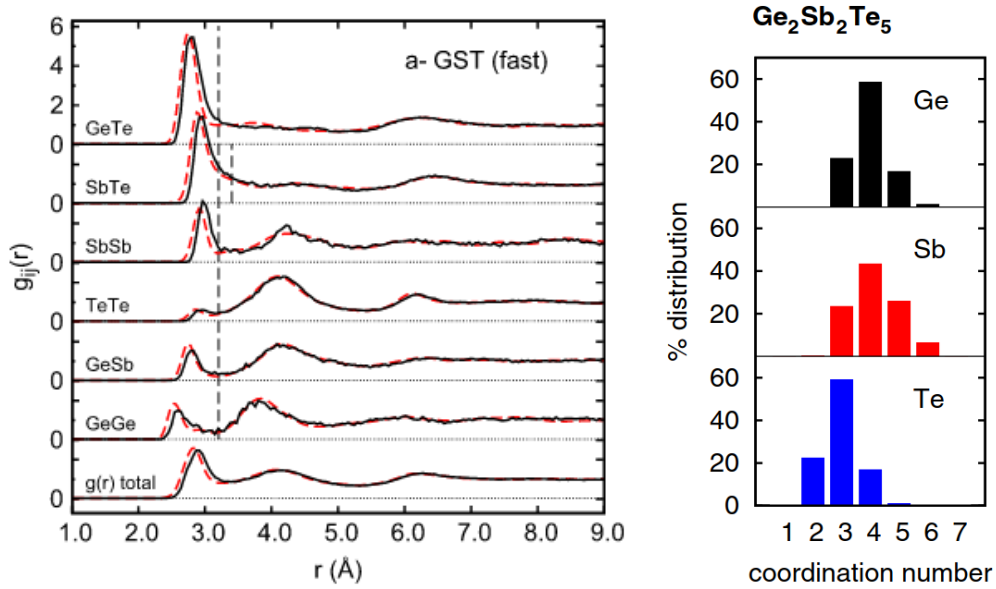

Figure 1.10: Partial and total pair correlation functions (left) and coordination number distributions (right) of amorphous GST225 from DFT simulations from [70].

Table 1.1: Partial average coordination numbers of amorphous GST225 as obtained from DFT simulations in Ref. [70].

	with Ge	with Sb	with Te	total
Ge	0.29	0.36	3.31	3.96
Sb	0.36	0.43	3.36	4.15
Te	1.33	1.34	0.30	2.97

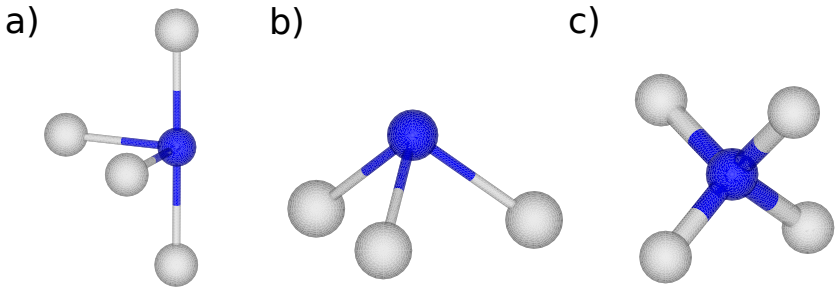

Figure 1.11: The typical local neighborhoods of atoms in the amorphous phase of GST alloys. a) Atom in defective octahedra with four neighbors, b) three-fold coordinated atom in a pyramidal geometry and c) four-fold coordinated atom in a tetrahedral geometry.

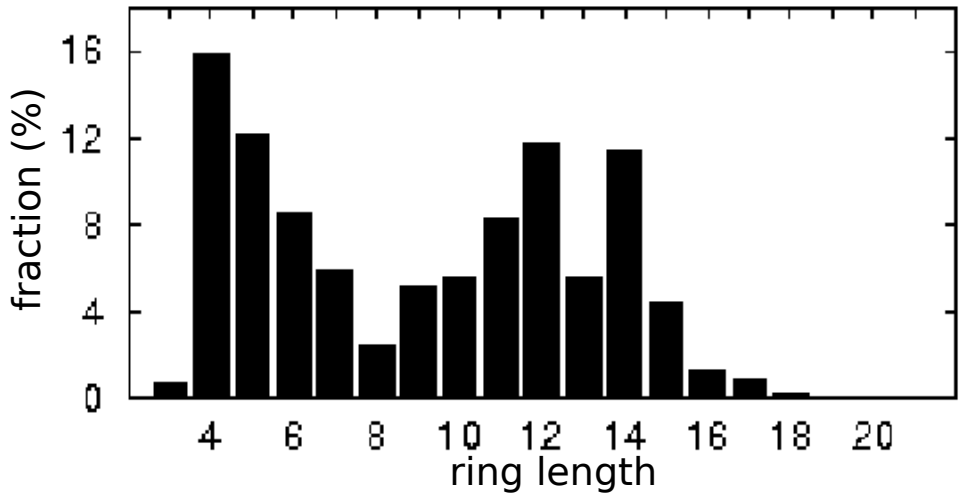

Figure 1.12: Distribution of the ring lengths in amorphous GST225 from DFT simulations from [15].

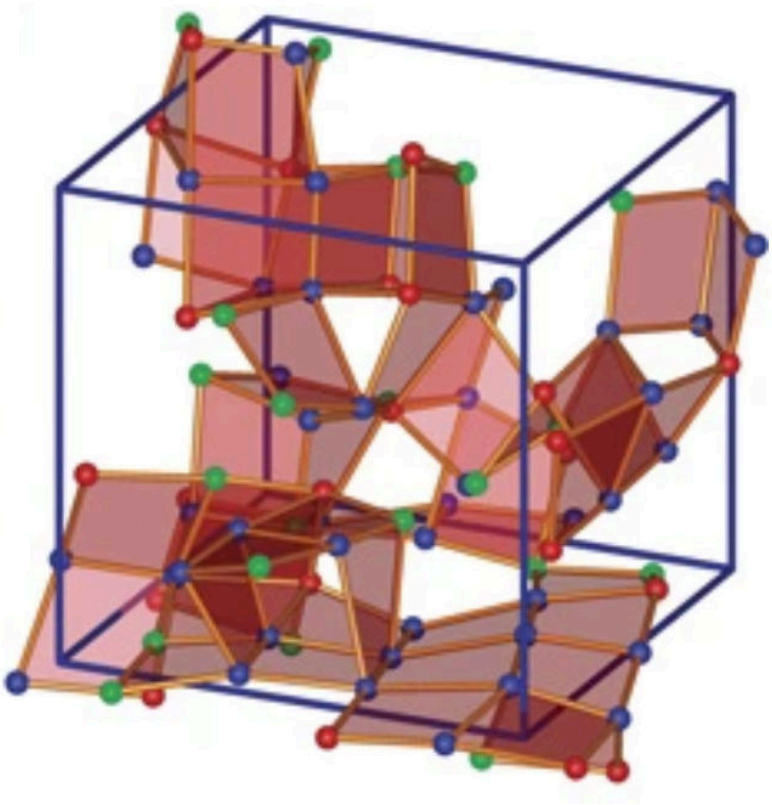

Figure 1.13: A snapshot of connected four-membered rings in the liquid phase of GST225. Taken from [17].

Concerning the electronic properties, GST225 is a degenerate p-type semiconductor in the cubic crystalline phase and an intrinsic semiconductor in the

amorphous phase [74] with an optical band gap of 0.5 and 0.7 eV in the two phases [75]. The stoichiometric compound in the cubic crystalline phase is an intrinsic semiconductor as was shown by DFT calculations [70]. The shift of the Fermi level into the valence band in the cubic phase is ascribed to defects of stoichiometry such as Sb and Ge deficiency. On the other hand, the Fermi level in the amorphous phase is pinned at around mid-gap, as defects in stoichiometry can be accommodated in the amorphous network by still remaining insulating. Actually, in the amorphous phase localized states are present in the mobility gap [70, 74] as shown in Fig. 1.15. In Fig. 1.14 we show x-ray photoemission spectroscopy (XPS) data and DFT electronic density of states (DOS) of crystalline and amorphous GST225 calculated with the PBE functional taken from Ref. [76] and Ref. [16]. The DFT band gaps, as usual, are underestimated (of about 0.2 eV) and the position of the Fermi level is in the gap. The shape of the electronic DOS is due to s- and p-like states of the atomic orbitals of Ge, Sb and Te as shown in Fig. 1.15.

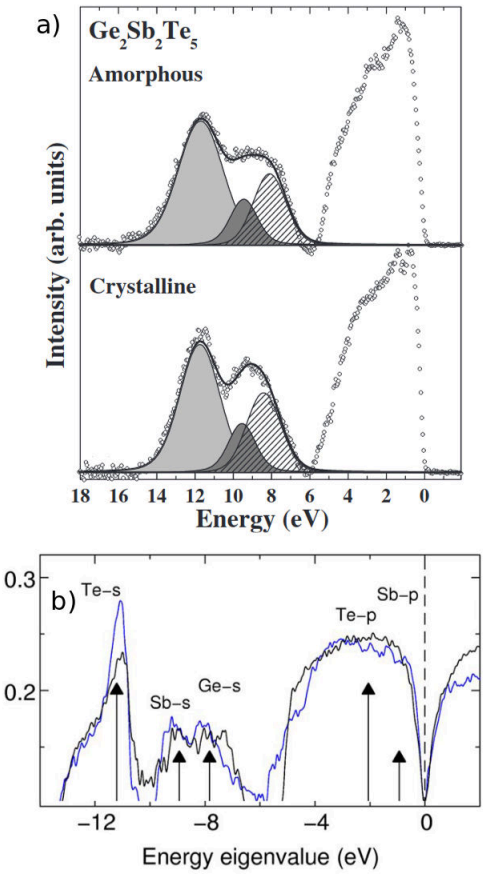

Figure 1.14: a) XPS data for amorphous (top) and crystalline (bottom) GST225 from Ref. [76]. b) DFT electronic DOS of amorphous (black) and crystalline (blue) GST225. The position in energy of atomic-like levels shown with vertical arrows. Adapted from [16, 76].

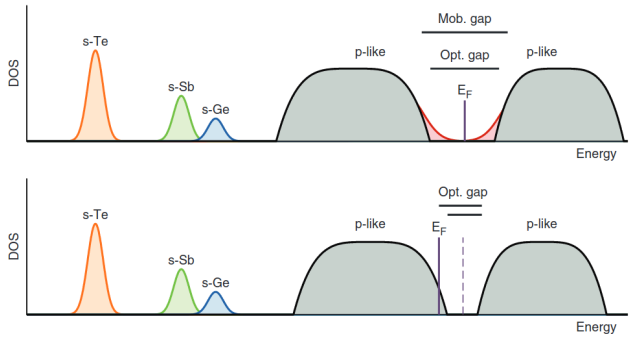

Figure 1.15: Sketch of electronic DOS in the amorphous (top) and crystalline (bottom) phase of GST alloys. Localized states are shown in red within the mobility gap while the Fermi level is pinned in the mid-gap. In the crystalline state, the Fermi level is typically shifted into the valence band due to defects in stoichiometry. Taken from [74].

Although the electronic DOS is very similar in the crystalline and the amorphous phase, there is a significant contrast in the optical absorption between the two phases due to an enhancement of the optical matrix elements in the crystalline phase [77]. This was ascribed to the presence in the crystalline phase of a new type of bonding named metavalent bonding (partially metallic, partially covalent) [78, 79, 80, 81]. In the metavalent bonding a half pair of electrons is shared between two atoms (3c-2e bonds) and the atoms are typically over-coordinated in geometries incompatible with the 8–N rule giving rise to peculiar behavior such as large effective charge, large Grüneisen parameter and large ϵ_∞ which are typical features of crystalline phase change materials. A different picture was recently proposed involving hyperbonds in the form of 3c-2e bonds originated from dative bonds from lone pairs of p and s orbitals [82, 83, 84].

1.2.1 Crystallization process

In GST alloys, at the operation condition of the memory device the crystallization proceeds via nucleation and growth. The nucleation process consists of the formation of a postcritical crystalline nucleus that is able to grow. The crystal growth velocity (v_g) depends on the driving force for crystallization, which is the difference in the chemical potential ($\Delta\mu$) between the supercooled liquid and the crystalline phase, and the self-diffusion coefficient (D) as given by the phenomenological Wilson–Frenkel (WF) expression [85] $v_g = u_{kin}(1 - e^{-\frac{\Delta\mu}{k_B T}})$ where the kinetic prefactor is given in turn by $u_{kin} = 4D/\lambda$ and λ is a typical atomic jump length in the diffusion process.

The crystallization process can be described by the classical nucleation theory [86, 87] where the formation of a crystalline nucleus depends on the free energy gain due to the crystallization and the free energy loss due to the

formation of a liquid-crystal interface. The formation free energy, assuming a spherical shape of the nucleus, is given by [88]:

$$\Delta G = -\frac{4\pi}{3} R^3 \rho_{crys} \Delta\mu + 4\pi R^2 \gamma \tag{1.1}$$

where R is the radius of the nucleus, ρ_{crys} is the atomic density, and γ is the liquid-solid interfacial energy. The maximum of $\Delta G^c = 16\pi\gamma^3/3(n_{crys}\Delta\mu)^2$ is the barrier for the formation of a critical crystalline nucleus with radius R_c=$2\gamma/n_{crys}\Delta\mu$. Classical nucleation theory provides also an expression for the steady state nucleation rate (I_{ss}) given by [88]:

$$I_{ss} = s_c \Gamma_z \frac{6D}{\lambda^2} e^{(\frac{-\Delta G^c}{k_B T})} \tag{1.2}$$

where s_c is the number of surface sites in the critical cluster. I_{ss} as a function of temperature is controlled by $\Delta\mu$ and D. The contribution of $\Delta\mu$ increases by cooling the system while that of D displays an opposite trend. The nucleation rate and the growth velocity have a different dependence on temperature and their maximum value is typically at two different temperatures. This gives rise to two different crystallization behaviors that can be present in different materials: nucleation- and growth-dominated crystallization. In nucleation-dominated crystallization, several postcritical nuclei form and the crystallization time does not depend on the volume of the sample. On the contrary, in growth-dominated crystallization, the process proceeds from the edges of preformed crystalline seed and therefore the crystallization time depends on the volume of the system. GST225 displays a nucleation dominated crystallization [1].

The crystallization of GST225 has been studied experimentally over a wide range of temperatures by means of ultrafast differential scanning calorimetry (DSC) measurements. Ultrafast DSC employs high heating rates necessary to investigate the crystallization of GST225 between 450 and 650 K where the crystallization is extremely fast and not accessible by traditional DSC measurements [89]. Then, under several assumptions, Ovara et al. extracted crystal growth velocity (v_g) as a function of temperature from the DSC data as shown in Fig. 1.16 [89].

Direct ab-initio molecular dynamics (AIMD) simulations of the crystallization of GST225, although computationally demanding, have been reported in literature. The first attempt employed small cells with a number of atoms ranging from 63 and 180 [17, 90, 91]. The small size of the cell enhanced the nucleation rate at the simulation temperature (600 K) due to fictitious interaction of the crystalline nucleus with its periodic images, which allowed the formation of a crystalline nucleus on a time scale of 0.5 ns. These simulations shed light on the mechanisms involved in the early stages of the formation of a postcritical nucleus. In particular, the analysis of the AIMD trajectory suggested that four-membered ABAB rings, which are the building blocks of the

crystal, are present in the supercooled phase as well and they play a crucial role in the formation of the medium-range ordered planar structures which form a seed for a fast crystallization. Subsequently, larger models (460- and 648-atom supercells) and longer simulations (up to 8 ns) [72, 92, 93] were employed to study the crystallization of GST225 at several temperatures in the range 500-700 K, confirming the important role of the four-membered rings in the nucleation process. Finally, in Refs [73, 94] MD simulations with large models up to 900-atoms supercell were employed to study the crystallization of amorphous GST225. In these works, the crystallization growth velocity in the bulk and from the liquid-crystal interface were studied. For the crystallization in the bulk, a postcritical nucleus was generated by means of metadynamics techniques. It was found that the crystal growth velocity is very similar in the two cases, from the growth of an postcritical nucleus in the bulk and from the movement of the crystal-liquid interface both at 6000 K is about 1 m/s [73]. Moreover, by comparing the value of the crystal growth velocity obtained from small (460-atoms) and larger (900-atoms) models, it was observed that the smaller models overestimate the crystal growth velocity by a factor of two due to finite size effects.

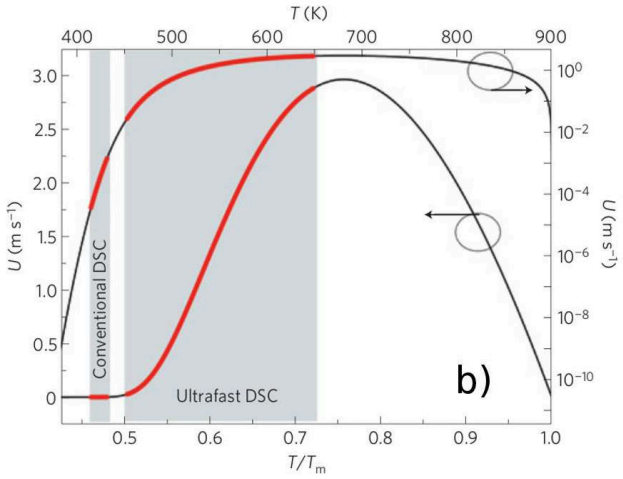

Figure 1.16: Temperature dependence of the crystal growth velocity of GST225 based on DSC analysis. Taken from [89].

1.3 Ge-rich GeSbTe alloys for embedded memories

The search for new memory technologies was prompted about two decades ago by the need to get around the scaling limitations of flash memories based on the floating gate MOS transistors. Several technologies have been proposed, such as ferroelectric magnetic RAM (MRAM), ferroelectric RAM (FRAM), resistive-switching oxides (ReRAM), and PCMs. PCMs are the most mature option among emerging memory technologies. PCMs have also shown the

possibility to fill the performance gap between the flash and DRAM memories giving rise to a new class of memories called "Storage class memories".
In the same years that PCM technology for stand-alone applications made significant progress and demonstrated to be a reliable technology with elevated manufacturability and high production volume, the semiconductors industry started to develop increasingly sophisticated Systems on Chip (SoC). A SoC is an integrated circuit that bundles several components such as CPU, memory, signal processor and others to add functionality to electronic devices. Today, almost every, if not all, electronic device is based on SoC. PCMs made their way also into this market and the first embedded PCM, based on GST225, was presented in 2009 [95] thanks to its capability to compete with the conventional embedded flash memories and all the other candidates discussed above. Indeed, in principle, all the new technologies initially proposed for memory applications to replace flash memories are suitable for embedding applications thanks to their common advantages as shown in Fig. 1.17. Nevertheless, PCMs have a larger read window than MRAMs and ReRAMs thanks to the larger change in the resistance between the two logical states with respect to MRAM and the low resistance noise with respect to ReRAMs. PCMs encode the information employing phenomena observed in the bulk, which makes these memories less sensitive to point defects down to a few nanometers. On the other hand, MRAMs functionality is based on an ultra-thin tunnel dielectric layer while ReRAMS, more specifically filament ReRAMS, exploit the migration of a few tens of atoms (or ions) which makes them less reliable.

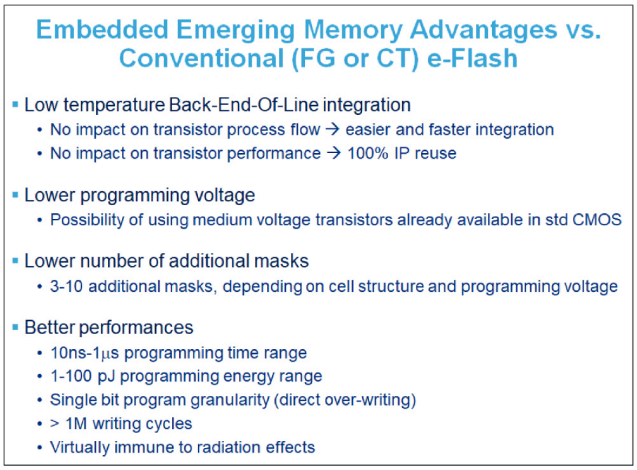

Figure 1.17: Common advantages of the emerging memory technologies (MRAM, FRAM, ReRAM and PCMs) for embedded applications compared with the conventional flash technologies. Taken from [95].

The soldering problem in embedded PCMs (ePCMs) requires, however, data retention at temperatures much higher than the T_x of GST225. Higher T_x are also needed for ePCMs of interest for automotive sector. Several strategies to enhance the T_x of phase change materials have been pursued. As already anticipated, several materials have been explored such as InSbTe [6], InGeTe

[5] or GaSbTe [7] alloy, light doping GST225 with N, O [8] or employing Sb-/Ge-rich GST alloys [10]. Among these materials, Ge-rich GST alloys are the most promising candidates for high-temperature applications. Indeed, several proofs of concepts of embedded memories based on Ge-rich GST alloys are reported in literature [10, 12, 13, 96, 97, 98].

A few years ago, a 'golden composition' for high-temperature PCM applications was obtained starting from Ge_2SbTe_2 by increasing the fraction of Ge [10]. Ge_2SbTe_2 is an isoelectronic alloy on the Sb-GeTe isoelectronic tie-line which corresponds to a fixed average number of three p electrons for each crystalline site. The golden composition showed a reasonable compromise between switching speed ($\sim$ 80 ns) and thermal stability (T_x of about 520 K). Further exploration showed that T_x can reach up 600 K (see Fig. 1.18) by increasing further the fraction of Ge [13, 12, 99, 100]. A composition among those screened was employed in a 4-Mb chip. The resulting embedded PCM displayed enhanced data retention although with a switching speed three times slower than that of GST225, an endurance of 10^8 cycles and a well-defined reading window (see Fig. 1.19) [13]. Despite the programming speed reduction, this prototypical embedded PCM competes with flash-embedded memories and is compatible with the tight requirements of automotive applications.

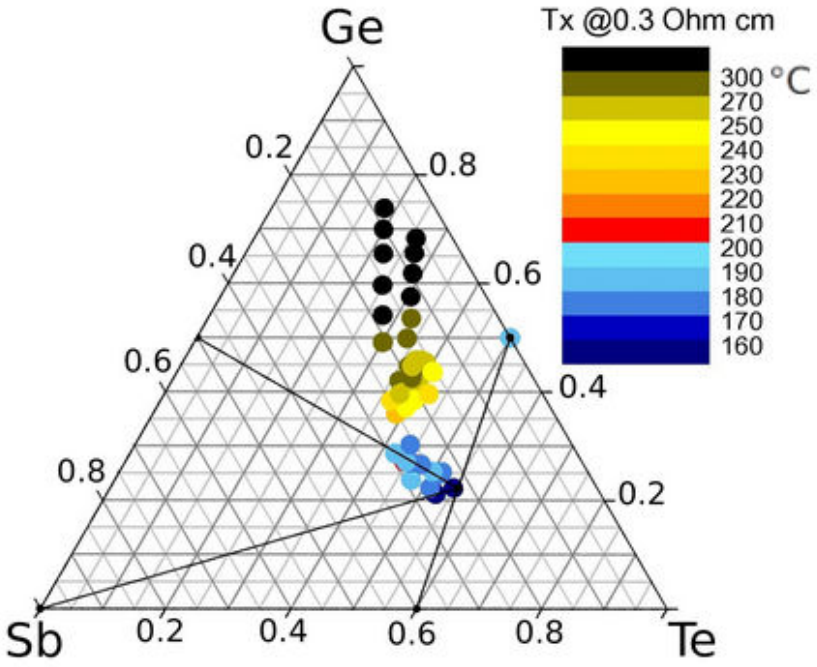

Figure 1.18: T_x of Ge–rich alloys from Ref. [13].

The high T_x of Ge-rich GST alloys has been ascribed to a phase separation into Ge and less Ge-rich GST alloys [12, 101, 102, 103, 104, 105]. The mass transport involved in the phase separation slows down the crystallization

kinetics as the segregation phenomena require a long diffusion length of the atoms, which would imply a longer incubation time to form crystalline supercritical nuclei. The phase separation was observed after the crystallization of as-deposited amorphous films [102, 103, 104, 101] and during forming (initialization) of the memory cells [12, 98]. The inhomogeneity resulting from the phase separation in PCM cells based on Ge-rich GST alloys has some drawbacks such as the resistance drift in the SET (crystalline) state [14]. The resistance drift is present also in the memories based on GST225, but only in the RESET state due to the aging of the amorphous phase that evolves with time towards a more stable amorphous structure with a larger electronic gap and a higher electrical resistivity. In the Ge-rich PCMs, the drift affects the SET and RESET states which brings some additional reliability problems. Furthermore, PCMs based on Ge-rich GST display a high cell-to-cell variability possibly due to the inhomogeneities of both SET and RESET states. Therefore, further investigations have been carried out on Ge-rich GeSbTe films required to better understand this segregation processes and to improve the choice of GST composition in order to minimize these detrimental effects.

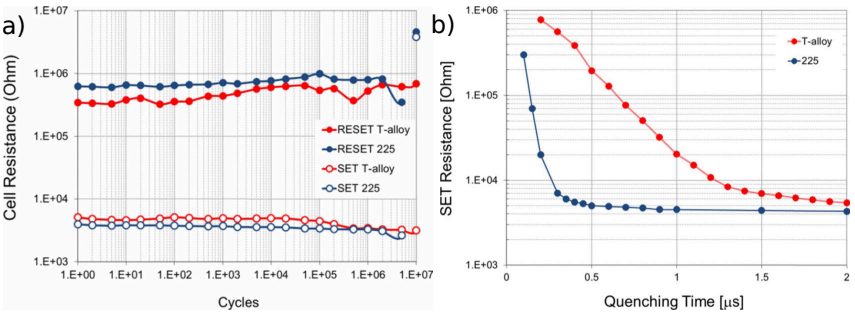

Figure 1.19: a) Cycling performances of a prototypical memory cell based on a Ge-rich GST alloy compared with that of GST225. b) SET resistance as a function of the quenching time for the same two cells. Adapted from [13].

Several experimental works have been devoted to the investigation of the phase separation phenomena. In Ref. [10], time-resolved XRD data indicate the formation of crystalline Ge and cubic GST alloy at about 540 K starting from Ge-rich Ge_2SbTe_2 amorphous alloy. In Ref. [98], the crystallization of an amorphous film of a GST alloy with 45% Ge excess with respect to GST225 gives rise to a cubic GST alloy at around 620 K, while the formation of crystalline Ge is observed at 670 K. In Ref. [102, 104] the crystallization of a GST amorphous film with 45% excess of Ge with respect to GST225 and 4% of nitrogen doping was studied both by annealing the as-deposited material and by subsequent crystallization and amorphization cycling by laser irradiation in GST alloys in the cubic phase with different compositions were observed, along with the formation of Ge crystallites embedded in the GST matrix as shown in Fig. 1.20. The compositional map was obtained from EELS measurements which might be affected by the presence of grains with different compositions along the section of the sample over which the spectra are recorded.

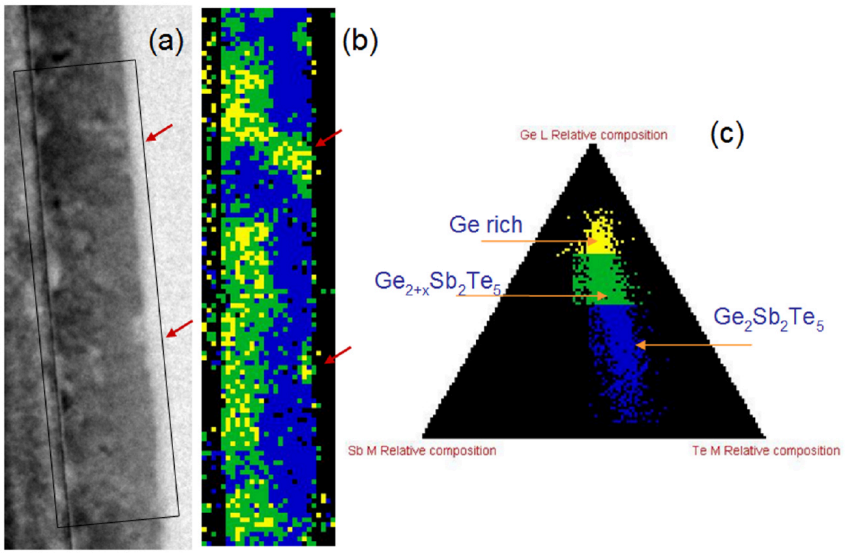

Figure 1.20: (a) TEM micrograph of the Ge-rich GST film after laser irradiation with a low energy density. Crystalline regions are indicated with red arrows. (b) Compositional map obtained from EELS spectra. Blue regions correspond to GST alloys with less than 45% content of Ge while yellow ones are richer in Ge (around 65%) (c) Compositions according to the EELS map. Taken from [102].

The first annealing of the as-deposited material leads to the formation of Ge crystallites that survive the subsequent cycling process which involves a GST alloy with a lower fraction of Ge with respect to the initial one. The initial annealing of the as-deposited material corresponds to the so-called forming operation of the memory [12].

More recently, Luong and et al. [101] have studied the crystallization of Ge-rich GST225 with Ge content above 30%. The crystallization process was studied by several long annealing. The XRD data in Fig.1.21 suggested the following scenario for the phase separation. First, Ge diffuses out from the GST matrix at around 590-610 K. At this temperature, the small regions of pure Ge start to crystallize which enhances the Ge diffusion towards these crystallites and hence the impoverishment of the amorphous GST matrix. Once the Ge content in the GST regions is low enough, the GST matrix starts to crystallize in cubic GST225. This composition was inferred from the lattice parameter which, however, is very similar for a wide range of the compositions along the GeTe-Sb_2Te_3 pseudobinary line. A very recent paper [106], suggests a scenario very similar to that proposed by Luong et al. with an intermediate step between the crystallization of Ge and that of the GST matrix. This additional step consists of the formation of GeTe in regions very rich in Ge, which allows the further impoverishment in Ge of the amorphous regions as shown in Fig. 1.22.

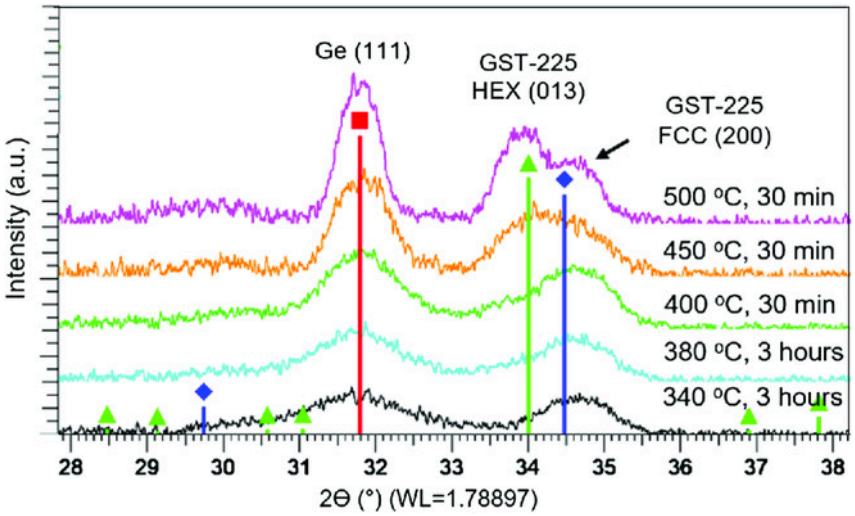

Figure 1.21: XRD patterns of Ge rich GST films annealed at different temperatures in the range between 610 and 770 K with different annealing times in the range between 0.5 up to 3 hours in nitrogen atmosphere. The vertical lines with red squares, green triangles, and blue diamonds show the expected angular positions of the diffraction peaks corresponding to the Ge (111), GST225 Hexagonal (HEX–013), and GST-225 Face Centered Cubic (FCC–200) planes, respectively. Taken from [101].

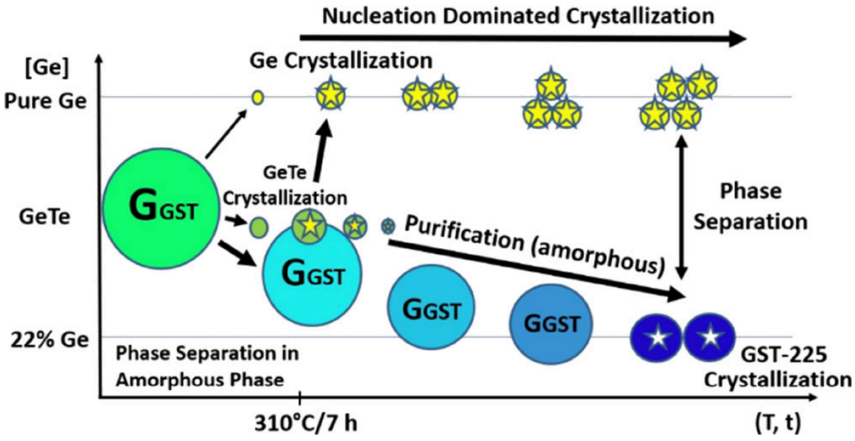

Figure 1.22: The suggested crystallization mechanism for Ge-rich GST alloys based on synchrotron X-ray data obtained during isothermal annealing. Taken from [106].

In Fig. 1.21 one observes that after further prolonged annealing time at higher temperature the formation of hexagonal GST225 was detected at almost 720 K [101], which is roughly 100 K higher than cubic-hexagonal transition temperature in GST225 [107]. This may suggest that the cubic phase might have a different composition than GST225. Nevertheless, GST alloys on the GeTe-Sb_2Te_3 tie-line are the only ternary compounds in the Ge-Sb-Te phase

diagram which are thermodynamically stable and which a Ge-rich off stoichiometric GST alloys is supposed to crystallize into if the sample is annealed at a sufficient high temperature and for a sufficiently long time. Although this might be the case for the long annealing protocol performed in Ref. [101], the operation conditions of the memory are quite different, leading to a rapid rise of temperature with a crystallization time of a few μs at most. In this respect, the laser irradiation annealing used in Refs [102, 104] are somehow closer to the operation conditions of PCMs.

Several questions regarding the phase separation process emerge naturally from the experiments summarized above. For instance, it is not clear yet to which extent the phase separation is reversible during SET/RESET operations. What are the compositions and phases of the resulting crystalline GST alloy? What crystallizes first, Ge or GST?

Theoretical calculations might provide a deeper insight into the phase separation as already done for other properties of GST alloys. In this respect, a recent theoretical work [108] investigated the stability of the amorphous phase of Ge-rich GST alloys along the Ge-$GeSb_2Te_4$ tie-line based on first principles calculations. This study showed, based on energetic analysis, that alloys with Ge content above 50 % are thermodynamically unstable with respect to phase separation into amorphous Ge and amorphous $GeSb_2Te_4$ (see Fig. 1.23).

This work suggests that phase separation of highly Ge-rich GST alloys could take place in the amorphous phase itself. It remains to be seen whether Ge-rich GST with Ge content close or slightly below 50% could remain a metastable composition during the crystallization in the cubic phase. In PCMs the phase separation is believed to occur during the crystallization process which is slowed down because of the mass transport involved in the segregation of Ge. In the operation conditions of the memory, it is still unclear whether phase separation occurs first in the amorphous phase or it is concomitant with the crystallization process

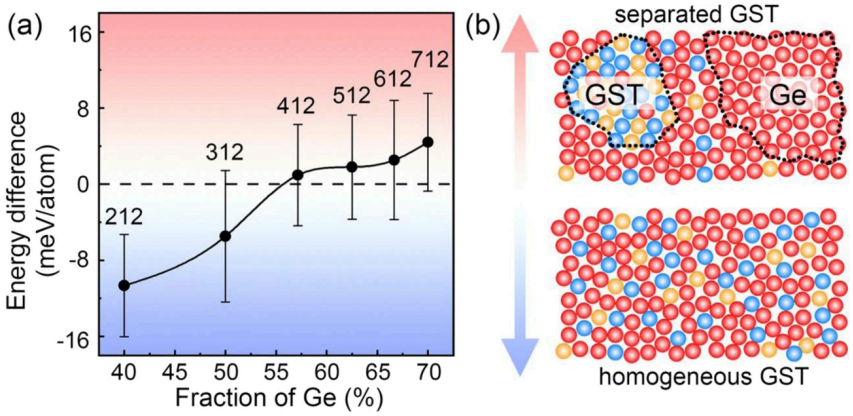

Figure 1.23: DFT formation energy of amorphous GST alloys along the Ge-$GeSb_2Te_4$ tie-line with respect to Ge and $GeSb_2Te_4$ (both in the amorphous phase). Alloys with a fraction of Ge larger than 50% are unstable upon decomposition into amorphous Ge and amorphous $GeSb_2Te_4$. Taken from [108].

In the previous DFT work of Ref. [108] the structural properties of the amorphous phase of the alloys along the Ge-$GeSb_2Te_4$ tie-line was studied as well. It was shown that by increasing the fraction of Ge the local structure of the amorphous phase becomes more and more dissimilar from the octahedral-like geometry in four-membered rings of the cubic phases. Namely, by increasing the fraction of Ge, one observes an increase of Ge-Ge homopolar bonds, of Ge atoms in tetrahedral geometry and of long-membered rings at the expense of four-membered rings (see Fig.1.24).

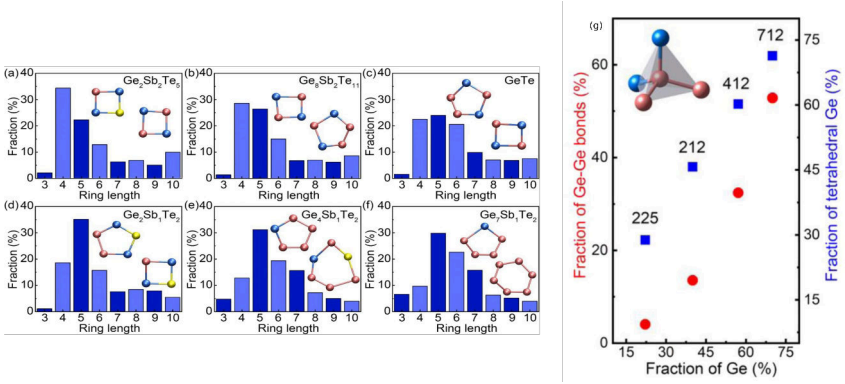

Figure 1.24: From (a) to (f): the distribution of rings length in DFT models of amorphous phase of alloys along the Ge-$GeSb_2Te_4$ and GeTe-Sb_2Te_3 tie-lines. Typical rings in each model are shown in the insets. Ge, Sb, and Te atoms are shown with red, yellow, and blue spheres. (g) Fraction (%) of Ge-Ge homopolar bonds and Ge in tetrahedral geometry in amorphous Ge-rich GST alloys. Taken from [108].

The work on Ref. [108] was published a few months after we submitted our paper on the simulations of Ge-rich GST alloys [109] that will be discussed in

Sec. 3. Both Ref. [108] and our paper [109] addressed the structural properties of the amorphous phase of Ge-rich GST alloys and very similar results were observed in our simulations as will be discussed in more detail in the following chapters.

Chapter 2

Methods

In this thesis, we performed electronic structure calculations on the properties of GeSbTe alloys. We used density functional theory (DFT) as described in Sec. 2.1 to optimize the structure of the crystalline phase and to compute phonons as described in Sec. 2.2. From DFT phonons and the semiempirical Bond polarizability model (see Sec. 2.3), we computed Raman spectra of GeSbTe alloys. Models of the amorphous phase of GeSbTe alloys have been quenched by molecular dynamics simulations as described in the Sec. 2.4. Finally, to enlarge the scope of DFT method, we employed a machine learning technique to develop a Neural Network interatomic potential for the GST225 compound using the scheme described in Sec. 2.5.

2.1 Density functional theory

The objective of condensed matter physics is to explain the physical and chemical properties of molecules and solid-state systems at the atomic level. Most of these properties are governed by quantum effects, making this fundamental theory the best tool to investigate materials. In the original formulation of quantum mechanics, the fundamental equation to study a system is the Schrödinger equation where the unknown object that governs the system evolution is the wavefunction. The wavefunction of a system depends on the coordinates of all the nuclei and electrons that make it up. In the Born–Oppenheimer (BO) approximation [110] the dynamics of the electrons and nuclei are decoupled thanks to the large differences in masses between the nuclei and electrons. This approximation allows the factorization of the wavefunction into electronic and nuclear components. Yet, the BO problem is still a differential eigenvalue equation depending upon a large number of variables, three for each electron. Therefore, a reformulation of the problem is required to reduce its complexity.

In this respect, Hohenberg and Kohn in the mid '60s proposed a framework in which the electronic density replaces the wavefunction as an unknown variable of the problem [111]. This new framework is known as Density Functional Theory. Within this scheme, the energy of an electronic gas subject to

an external potential V_{ext} is given by:

$$E[n(x)] = F[n(\mathbf{r})] + \frac{1}{2}\int d\mathbf{r}d\mathbf{r}'\frac{n(\mathbf{r})n(\mathbf{r}')}{\mid \mathbf{r}' - \mathbf{r}' \mid} + \int d\mathbf{r}n(\mathbf{r})V_{ext}(\mathbf{r}) \tag{2.1}$$

where $n(\mathbf{r})$ is the electronic density and $F[n(\mathbf{r})]$ is a unique and universal functional independent of the external potential. $F[n(\mathbf{r})]$ describes the kinetic, exchange and correlation terms of energy. The second term in Eq. 2.1 is Hartree energy while the third one is due to the interaction of electrons with the external potential (the presence of nuclei, for instance). In this framework, the energy is a functional of the electronic density and the explicit knowledge of the wavefunction is not necessary to calculate the energy of a system. Thus, the solution of the problem is obtained from the knowledge of a function of three variables instead of the 3N variables that the wavefunction depends on. The ground state energy of a system can be obtained by minimizing the energy functional with respect to the electronic density with the constraint of a fixed number of electrons, thanks to the variational property of the emerging framework. Unfortunately, the analytical form of $F[n(\mathbf{r})]$ is unknown, so approximations are needed.

The actual implementation of DFT for ground state electronic structure is based on the Kohn-Sham (KS) scheme [112]. In this scheme, the N-electrons interacting system is mapped into a system of non-interacting electrons subject to an effective potential V_{eff} (auxiliary system) under the constraint that the densities of the auxiliary system and the real one are the same. This mapping between the two systems results in a Schrödinger-like single particle equation:

$$\hat{H}_{ks}\phi_i(\mathbf{r}) = (-\frac{1}{2}\nabla_r^2 + V_{eff}(\mathbf{r})\Big)\phi_i(\mathbf{r}) = \epsilon_i\phi_i(\mathbf{r}) \tag{2.2}$$

where $\{\phi_i\}$ and $\{\epsilon_i\}$ are KS orbitals and energies of the auxiliary system. The constraint that the auxiliary and the real densities must obey yields the effective potential:

$$V_{eff}(\mathbf{r}) = V_{ext}(\mathbf{r}) + V_H(\mathbf{r}) + V_{xc}(\mathbf{r}) \tag{2.3}$$

where

$$V_H(\mathbf{r}) = \int d\mathbf{r}'\frac{n(\mathbf{r}')}{\mid \mathbf{r} - \mathbf{r}' \mid},$$

$$V_{xc}(\mathbf{r}) = \frac{\delta E_{xc}}{\delta n(\mathbf{r})},$$

with

$$n(\mathbf{r}) = \sum_i^N \mid \phi_i(\mathbf{r}) \mid^2 \tag{2.4}$$

Therefore the total energy of the system is given by:

$$E = \sum_{i=1}^{N} \epsilon_i - \frac{1}{2} \int d\mathbf{r} n(\mathbf{r}) V_H(\mathbf{r}) - \int d\mathbf{r} n(\mathbf{r}) V_{xc}(\mathbf{r}) \tag{2.5}$$

where i runs over the occupied KS orbitals. The only unknown term in Eq. 2.5 is the exchange and correlation energy functional $E_{xc}[n(r)]$. Several approximations have been proposed for this energy term such as the local density approximation (LDA) due to Kohn and Sham themselves [112] or the Generalized Gradient Approximation (GGA) [113, 114] whose most popular implementation is due to Perdew, Burke, and Ernzerhof (PBE) [115]. In the LDA approximation, the exchange and correlation energy is assumed to be that of a homogeneous electron gas with the same density:

$$E_{xc} = \int d\mathbf{r} n(\mathbf{r}) \epsilon_{xc}^{homo}(n(\mathbf{r})) \tag{2.6}$$

while in the GGA approximation, the exchange and correlation energy depends locally on the density and its gradient:

$$E_{xc} = \int d\mathbf{r} n(\mathbf{r}) \epsilon_{xc}^{homo}(n(\mathbf{r})) f(n(\mathbf{r}), \nabla n(\mathbf{r})) \tag{2.7}$$

The KS equations can be solved by a self-consistent procedure. First, an initial guess of the electronic density is employed to compute the effective potential. Then the KS secular equation is solved. The resulting KS orbitals are then employed to reevaluate the effective potential based on the new density, which is in turn employed to solve the KS equation at the second iteration and this procedure is repeated until self-consistency is reached (see Fig. 2.1).

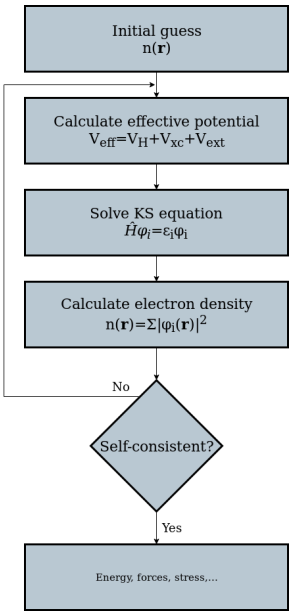

Figure 2.1: A sketch of the iterative self-consistent procedure employed to solve the KS equation. Initially, a guessed electronic density is used to evaluate the effective potential (electron density as a sum of atomic densities for an initial given nuclear configuration, for instance) and then to solve KS equation. The KS orbitals obtained from the previous step are used to compute a new density and subsequently a new effective potential. The new effective potential is plugged again into the KS problem and so on until convergence is reached.

2.1.1 Plane waves basis set

KS orbitals (ϕ_i) can be expanded in basis functions, which turns the solution of the KS secular equation into an algebraic eigenvalue equation. Expanding the KS orbitals in plane waves makes the calculation of the Hartree potential V_H and the exchange-correlation energy E_{xc} straightforward. This choice for a periodic system reads:

$$\phi_{i,k} = \sum_{\mathbf{G}} c_{i,\mathbf{k}}(\mathbf{G}) \frac{1}{\sqrt{\Omega}} e^{i(\mathbf{k}+\mathbf{G})\cdot\mathbf{r}} = \sum_{\mathbf{G}} c_{i,\mathbf{k}}(\mathbf{G}) \left|\mathbf{k}+\mathbf{G}\right\rangle \tag{2.8}$$

where $c_{i,\mathbf{k}}(\mathbf{G})$ are the expansion coefficients, $\mathbf{G}$ are the reciprocal lattice vectors and Ω is the volume of the system. In practical calculations, the basis set is truncated at a given cutoff E_{cut} and hence, only plane waves with kinetic energies $\frac{\hbar^2(\mathbf{k}+\mathbf{G})^2}{2m_e}$ smaller than the cutoff are included in the basis set. The value of the cutoff is optimized in order to converge the physical quantities under investigation.

In a periodic system the potential is periodic and it can then be expanded in plane waves as well as:

$$V_{Hxc} = \sum_{\mathbf{G}} V_{Hxc}(\mathbf{G}) e^{i\mathbf{G}\cdot\mathbf{r}} \tag{2.9}$$

where V_{Hxc}=V_H+V_{xc} and $V_{Hxc}(\mathbf{G})$ is given by:

$$V_{Hxc}(\mathbf{G}) = \frac{1}{\Omega_{cell}} \int_{\Omega_{cell}} d\mathbf{r} V_{Hxc}(\mathbf{r}) e^{-i\mathbf{G}\cdot\mathbf{r}} \tag{2.10}$$

Then, the KS eigenvalue problem (Eq. 2.2) turns into an algebraic expression:

$$\sum_{\mathbf{G}'} \langle \mathbf{k}+\mathbf{G} | \hat{H}_{KS} | \mathbf{k}+\mathbf{G}' \rangle c_{i,\mathbf{k}}(\mathbf{G}') = \epsilon_{i,\mathbf{k}} c_{i,\mathbf{k}}(\mathbf{G}) \tag{2.11}$$

where the matrix elements of the Hamiltonian are given by:

$$\langle \mathbf{k}+\mathbf{G} | \hat{H}_{KS} | \mathbf{k}+\mathbf{G}' \rangle = \frac{\hbar^2(\mathbf{k}+\mathbf{G}')^2}{2m_e} \delta_{\mathbf{G},\mathbf{G}'} + V_{Hxc}(\mathbf{G}-\mathbf{G}') + \langle \mathbf{k}+\mathbf{G} | V_{ext} | \mathbf{k}+\mathbf{G}' \rangle \tag{2.12}$$

2.1.2 Pseudopotentials

First-principles calculations including all electrons are very demanding. However, since most of the physical and chemical properties of interest depend only on the valence electrons, one can exploit pseudopotentials [116], which substitute the Coulomb interaction between the valence electrons and the ion (core electrons and nucleus) with an effective potential $V_{ps}(\mathbf{r})$. This effective potential acting on the valence electrons is smoother than the Coulomb potential due to the nucleus, as it incorporates both Coulomb interactions with the nucleus and the core electrons and the Pauli repulsion interaction between core and valence electrons (see Fig. 2.2). The resulting effective potential can be expanded in plane waves with a kinetic energy cutoff lower than that required for the original Coulomb potential with the nucleus. The pseudopotential acts on pseudo KS orbital and hence the KS equation (2.2) for an atom reads:

$$\hat{H}_{KS}\phi_i^{PS}(\mathbf{r}) = (\frac{-1}{2}\nabla_{\mathbf{r}}^2 + V_{PS}(\mathbf{r}) + V_H + V_{xc})\phi_i(\mathbf{r})^{PS} = \epsilon_i \phi_i^{PS}(\mathbf{r}) \tag{2.13}$$

The pseudo KS orbital ϕ^{PS} is built from the all-electron wavefunction outside the core region, up to a given cutoff radius (r_c) which in joint with a smoother function inside the core region. The pseudopotential V_{ps} is obtained by inverting Eq. 2.13 with ϵ_i equal to the all-electrons solution of the atomic problem.

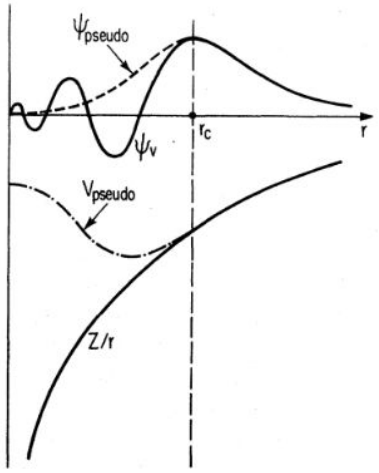

Figure 2.2: A comparison between a long-range $\frac{1}{r}$ potential and a smoother pseudopotential and their corresponding wavefunction.

2.1.3 The hybrid Gaussian and plane waves method

Electronic structure calculations based on DFT employing pseudopotentials and KS orbitals expanded in plane waves have achieved great success in the prediction of the properties of condensed matter systems. This method displays several advantages: the solution of the Poisson equation is very simple with plane waves, the basis set is unbiased and does not depend upon the atomic coordinates which makes the evaluation of the derivatives of the energy simpler. Moreover, this basis set allows employing the fast Fourier transform techniques and testing the convergence in a simple way. However, this basis also features some drawbacks, as the size of the basis set is typically large, which makes the calculation demanding.

On the other hand, one might use a Gaussian type atomic basis set for the expansion of the KS orbitals, which is typically smaller than the plane wave basis set. The Gaussian basis set is local and it depends on the number of atoms and not on the system volume, as it is the case for the plane waves basis. However, this basis set is not orthogonal, depends explicitly on the atomic positions and requires a solution of the Poisson equation in the real space which is more demanding than in the reciprocal space.

A way to merge the benefits of the two approaches is the so-called hybrid Gaussian and plane waves method [117] in which KS orbitals (ϕ_i) are expanded in a Gaussian basis set and the electronic density is expanded in plane waves basis as:

$$\phi_i(\mathbf{r}) = \sum_\mu c_{i\mu}\psi_\mu(\mathbf{r}) \Rightarrow n(\mathbf{r}) = \frac{1}{\Omega}\sum n(\mathbf{G})e^{i\mathbf{G}\cdot\mathbf{r}} = \sum_{ij} P_{ij}\phi_i(\mathbf{r})\phi_j(\mathbf{r}) \quad (2.14)$$

where $\psi_\mu(\mathbf{r})$ are Gaussian-like orbitals, $c_{i\mu}$ are the expansion coefficients, $n(\mathbf{r})$ is the electronic density, Ω is the volume and $P_{ij} = \sum_\mu c_{i\mu} c_{j\mu}$ is an element of the density matrix. Once the KS orbitals are determined in the Gaussian basis set, also the electronic density can be evaluated on a grid in the reciprocal space. Then, each term of the energy can be computed within the representation which minimizes the computation effort. Hence the DFT total energy in this hybrid method is given by:

$$\begin{aligned} E[n] = & \; E[T] + E_{eI}[n] + E_H[n] + E_{xc}[n] \\ = & \sum_{ij} P_{ij} \left\langle \phi_i(\mathbf{r}) \right| - \frac{1}{2}\nabla_r^2 \left| \phi_j(\mathbf{r}) \right\rangle + \sum_{ij} P_{ij} \left\langle \phi_i(\mathbf{r}) \right| V_{loc}^{PP} \left| \phi_j(\mathbf{r}) \right\rangle \\ + & \sum_{ij} \left\langle \phi_i(\mathbf{r}) \right| V_{nl}^{PP} \left| \phi_j(\mathbf{r}') \right\rangle + 2\pi\Omega \sum_{\mathbf{G}} \frac{n(\mathbf{G})^* n(\mathbf{G})}{G^2} \\ + & \int d\mathbf{r} n(\mathbf{r}) \epsilon_{xc}(n(\mathbf{r})) \end{aligned} \tag{2.15}$$

where $E_{eI}[\{\phi_i\}]$ is the electron nuclei interaction and has been split into its local V_{loc}^{PP} and non-local V_n^{PP} terms coming from the pseudopotential. In this hybrid scheme, the pseudopotentials are obtained as a linear combination of Gaussian functions as well [118, 119].

2.1.4 Brillouin zone integration

In solid state physics, several properties of a system are obtained by integrating over the Brillouin zone (BZ). Numerically, this integration is performed over a discretized mesh. Therefore, the integral is substituted by a sum over a set of k-points. By exploiting the symmetry of the system, only k-points laying in the irreducible Brillouin zone are considered, which allows reducing the computational effort of the calculation. Each point of the k-mesh within the irreducible BZ is weighted according to its multiplicity, which is given by the symmetry operations of the point group. Therefore, a generic physical quantity (A), which depends on the integration over the BZ can be evaluated as:

$$A = \frac{1}{\Omega} \int_{BZ} a(k) dk \rightarrow \frac{1}{N_k} \sum_k^{BZ} a(k) = \sum_k^{IBZ} w_k a(k)$$

where w_k is the weight of the k-th point. The KS equation is actually solved for each k-point in the mesh. As for the energy cutoff, the size of the k-point mesh must be tuned to guarantee the convergence of the physical quantity of interest. In this work, the Monkhorst-Pack method [120] was used to generate an optimal k-point mesh for integrations over the BZ.

2.2 Lattice dynamics from finite displacements

As discussed above, within the BO approximation the dynamics of nuclei and electrons are decoupled. First, the electronic eigenproblem is solved. The resulting ground state energy $E_{elec.}(\{\mathbf{R}\})$ (also known as Born-Oppenheimer energy surface) depends parametrically on the nuclear positions $\{\mathbf{R}\}$ and it corresponds to the interaction potential among the nuclei. So the force acting on the j-th atom is given by:

$$\mathbf{F_j} = -\frac{\partial E_{elec.}(\{\mathbf{R}\})}{\partial \mathbf{R}_j} \tag{2.16}$$

Then, it is possible to go further and compute the vibrational frequencies and the corresponding displacement patterns via the hessian of the BO potential energy surface at equilibrium condition ($\mathbf{F}_j = 0 \; \forall j$) such that:

$$det\Big|\frac{1}{\sqrt{M_i M_j}}\frac{\partial^2 E(\{R\})}{\partial \mathbf{R}_i \partial \mathbf{R}_j} - \omega^2\Big| = 0 \tag{2.17}$$

The matrix elements $\frac{\partial^2 E(\mathbf{R})}{\partial R_{i,\alpha} \partial R_{j,\beta}}$ can be evaluated by computing numerically the derivative of the force acting on the i-th atom due to a finite atomic displacement (u) of the the j-th atom along Cartesian direction α.

To construct the full dynamical matrix, 6N single point energy calculations are required. Within this method the dynamical matrix is accessible at the suepercell Γ-point only.

2.3 Bond polarizability model

From DFT phonons we computed the Raman spectra within the semiempirical Bond Polarizability Model (BPM) as discussed below.

The differential Raman cross section per unit volume in non-resonant conditions is given by:

$$\frac{d^2\sigma}{d\Omega d\omega} = \sum_j \frac{\omega_s^4}{c^4}\Big|\mathbf{e}_s \overline{\overline{R}}_j \mathbf{e}_i\Big|^2 \Big(n_B\Big(\frac{\hbar\omega}{k_b T}\Big) + 1\Big)\delta(\omega - \omega_j) \tag{2.18}$$

Where ω_s is the frequency of the scattered light, n_B is the Bose factor and e_i (e_s) is incident (scattered) polarization vectors. $\mathrm{R}_j^{\alpha\beta}$ is the element of the Raman tensor associated with the j-th phonon given by [62]:

$$R_j^{\alpha\beta} = \sqrt{\frac{V_0\hbar}{2\omega_j}} \sum_{k=1}^{N} \frac{\partial \chi_{\alpha\beta}^{\infty}}{\partial \mathbf{R}_k} \cdot \frac{\mathbf{e}(j,k)}{\sqrt{m_k}} \tag{2.19}$$

where α and β are Cartesian indexes, V_0 is the cell volume, ω_j is the frequency of the j-th phonon, χ^∞ is the electronic susceptibility, $\mathbf{R}_k$ is the coordinate of the k-th atom with a mass m_k and $\mathbf{e}$(j,k) is the eigenvector of the dynamical matrix corresponding to the j-th phonon. For insulators, the Raman tensor can be computed by electronic structure calculations from the electronic susceptibility, whose derivatives in turn can be calculated by finite differences moving the N atoms independent by symmetry. Thus, in order to compute the Raman tensor, one should perform 6N ab initio linear response calculations. For large systems, this approach is too demanding. An alternative semi-empirical approach is provided by the Bond Polarizability Model (BPM) [121] which assumes that the electronic susceptibility can be written as a sum of bond polarizabilities:

$$\chi^\infty = \frac{1}{V_0}\sum_i \alpha^i \tag{2.20}$$

where α^i is the polarizability tensor of the i-th bond, whose elements are given by:

$$\alpha^i_{\alpha\beta} = \alpha^i_\parallel \hat{\mathbf{d}}^i_\alpha \hat{\mathbf{d}}^i_\beta + \alpha^i_\perp(\delta_{\alpha\beta} - \hat{\mathbf{d}}^i_\alpha \hat{\mathbf{d}}^i_\beta) \tag{2.21}$$

where $\hat{\mathbf{d}}^i$ is the direction of i-th bond, $\alpha_\parallel$ is the longitudinal polarizability, $\alpha_\perp$ is the transversal polarizability. Then, the Raman tensor can be computed by taking the derivative of Eq. 2.21 which reads:

$$R = \frac{1}{\sqrt{V_0}}\sum_i \tilde{\alpha}^{i,\lambda} \tag{2.22}$$

where $\tilde{\alpha}^{i,\lambda}$ is the derivative of the polarizability of the i-th bond with respect to the displacement caused by the λ-th phonon. Assuming that α^i depends only on the bond length, the derivative $\tilde{\alpha}^{i,\lambda}$ can be written as

$$\begin{aligned}\tilde{\alpha}^{i,\lambda} = \sum_{\alpha,\beta} \frac{\alpha^i_\parallel - \alpha^i_\perp}{d^i} \cdot (u^{i,\lambda}_\alpha \hat{\mathbf{d}}^i_\beta + u^{i,\lambda}_\beta \hat{\mathbf{d}}^i_\alpha - 2(\mathbf{u}^{i,\lambda}\cdot\hat{\mathbf{d}}^i)\hat{d}^i_\alpha \hat{d}^i_\beta) \\ + ({\alpha'_\parallel}^i - {\alpha'_\perp}^i)\cdot(\mathbf{u}^{i,\lambda}\cdot\hat{\mathbf{d}}^i)\hat{d}^i_\alpha\hat{d}^i_\beta + {\alpha'_\perp}^i(u^{i,\lambda}\cdot\hat{\mathbf{d}}^i)\delta_{\alpha\beta}\end{aligned} \tag{2.23}$$

where $\alpha'_\parallel$ ($\alpha'_\perp$) is the derivative of $\alpha_\parallel$ ($\alpha_\perp$) with respect to the bond length and $\mathbf{u}^{i,\lambda}$ is the displacement of the atoms forming the i-th bond caused by the λ-th phonon. Equation 2.23 shows that BPM needs three parametersm namely $\alpha_\parallel - \alpha_\perp$, $\alpha'_\parallel$ and $\alpha'_\perp$ for each chemical bond in the system. The parameters for the BPM have been obtained for GST alloys in Ref [122] by fitting the DFT Raman spectra. The same parameters have been used in this thesis for Ge-rich GST alloys.

2.4 Molecular dynamics

Molecular dynamics is a computational method [123], which allows studying the evolution of a system of atoms numerically treating them as classical particles. Given an initial state (coordinates and momenta) of the system and the

interaction potential (force field) by discretizing the time scale Newton's equations of motion are integrated numerically. The choice of the force field, which drives the evolution of the system, might limit the system size and the accuracy of the computed properties. Empirical force fields, for instance, allows simulating large systems, up to a few millions of atoms for several microseconds. However, they are typically designed to reproduce a few properties and their reliability beyond these properties might be questioned. On the other hand, parameters free force-fields based on first principles methods are typically very demanding and limited to a few hundreds of atoms and simulations long up to nanoseconds.

The equation of the motion of each atom is integrated numerically considering a discrete timestep (Δt). There are several algorithms for the integration of the equation of motion. In this work, we employ the velocity Verlet algorithm [124] in which positions and velocities at the (n+1)-th timestep are given by:

$$\begin{aligned} r(t+\Delta t) &= r(t) + v(t)\Delta t + \frac{1}{2}a(t)\Delta t^2 \\ v(t+\Delta t) &= v(t) + \frac{a(t)+a(t+\Delta t)}{2}\Delta t \end{aligned} \tag{2.24}$$

where r is the coordinates vector of the i-th atom, v is the velocity and a is the acceleration evaluated from the force field. This algorithm provides stable numerical trajectories and has been shown to guarantee time reversibility and preserve the symplectic properties of the Hamiltonian with less error propagation with time compared to other methods.

In this thesis we performed both MD simulations with force fields (machine learning interatomic potential) and DFT MD in which the forces on ions are obtained at each step by solving the electronic problem within DFT.

2.5 Neural networks

The DFT scheme outlined in the previous sections is limited to the simulations of a few hundred atoms for at most a few ns. In the last 15 years, the scope of DFT simulations has been enlarged thanks to machine learning techniques following the seminal paper by Behler and Parrinello [18] which has shown that interatomic potentials with accuracy close to DFT methods can be achieved by fitting a large DFT database with a Neural Network (NN) method. In the following, we discuss the NN scheme that we used to generate a NN potential for the GST225 compound.

Artificial Neural Networks (NN) are a subclass of machine learning (ML) techniques, which in turn is a subclass of Artificial Intelligence (AI). AI is the

intelligence (or rationality) of a machine, which mimics the natural cognitive ability of natural intelligence associated with the human brain for instance. The goal of AI applications is to construct a model capable of inferring, predicting, sensing the environment, recognizing, classifying and decision making despite not being explicitly programmed to do that. This desire is motivated by considering that natural intelligence works in a completely different way from conventional computers and, very often, the brain is faster and more efficient (recognizing a familiar face, for instance) than the most powerful computer present nowadays. Indeed, NNs inspired by biological brains have reached a mature stage of development and are extensively employed in our everyday lives in facial recognition, self-driving cars, healthcare, market prediction, weather forecasting and many other applications. NNs have been also proven to be universal approximators capable to fit continuous, real-valued functions of any dimension to an arbitrary accuracy [125].

NNs were born in an attempt to emulate a nervous system [126]. Indeed, a general definition of NNs could be: a machine (hardware or software) modeled on the human brain and nervous system, which is capable of information processing according to its dynamical evolution as a response to an initial input.

NNs can be implemented with electronic components in hardware or simulated with mathematical models. The latter is the type of NNs used in this work. There are also several types of NNs differing on the learning procedure (supervised and unsupervised learning) and the architecture of the network itself. In this work, we are interested in NNs for fitting applications, which belong to the class of supervised learning and it is capable to infer and perform computations once a model is trained. These NNs acquire knowledge from some source and store it in the synaptic weights of the artificial neurons (the building block of the nervous system). The procedure used to build a NN model is the learning process and consists of tuning the synaptic weights of the network in order to attain a desired objective function. The learning process can be summarized in the following four steps:

(1) data collection
(2) model selection
(3) training
(4) validation

In our work, we employ NNs as a universal approximator to fit the potential energy surface (PES), which is a high dimensional continuous real-valued function aiming to generate an interatomic potential of a system. The idea is to fit a large database of DFT energies and forces to generate a classical interatomic potential with an accuracy close to that of the DFT level of theory. This NN interatomic potential can be used later to drive MD simulations without solving the demanding electronic problem at each time step.

NNs are not the only choice for this task. Indeed, several other options exist such as kernel-based methods [127], splines [128], multivariate Taylor expansions [129], fitting DFT data by an empirical analytical form of the potential energy and several others. However, most of these methods fail in the case of high dimensional functions, which is the case of PES of a model with several atoms, due to the so-called curse of dimensionality. In fact, by increasing the dimensions of a function, the space to explore increases exponentially. In the case of limited datasets for the fitting procedure, these data become sparse, which results in a bad representation of the function. NNs are less prone to suffer from this problem thanks to their flexibility. Indeed, biological nervous systems are known to be plastic and this plasticity allows them to adapt to their surrounding environment and it turns out to be essential for the functionality of the neurons to process information. In turn, artificial NNs inherit the plasticity of their natural counterpart as they have been thought to emulate natural behavior.

2.5.1 Feed-forward neural network

Most of the NN interatomic potentials methods proposed so far are based on a class of NN called feed-forward NN. In this framework, the information (atomic coordinates or atomic descriptors in our case) flows within the network from the input layer through the intermediate layers used to approximate the desired function f(x) (PES in our case), and finally to the output y (energy in our case) without any feedback connection to the output of the network to itself. This choice results in a deterministic function of the only input. More specifically, a feed-forward NN model can be represented by several layers with only one input layer and one output layer. Each layer contains several nodes. Each node is essentially a nonlinear function (also known as an activation function) and these nodes are fully connected. The connections between the nodes emulate the synapses of the brain and their weight controls the synaptic activity. Each node receives a linear combination of signals from the nodes in the previous layer in the NN. The resulting signal is the input of the nonlinear function, which controls the response of this neuron and hence the signal transmitted to the subsequent layer in the NN. Therefore, NN is essentially a representation of a nonlinear mapping from the input variables to the output. A sketch of sample feed-forward NN is shown in Fig. 2.3.

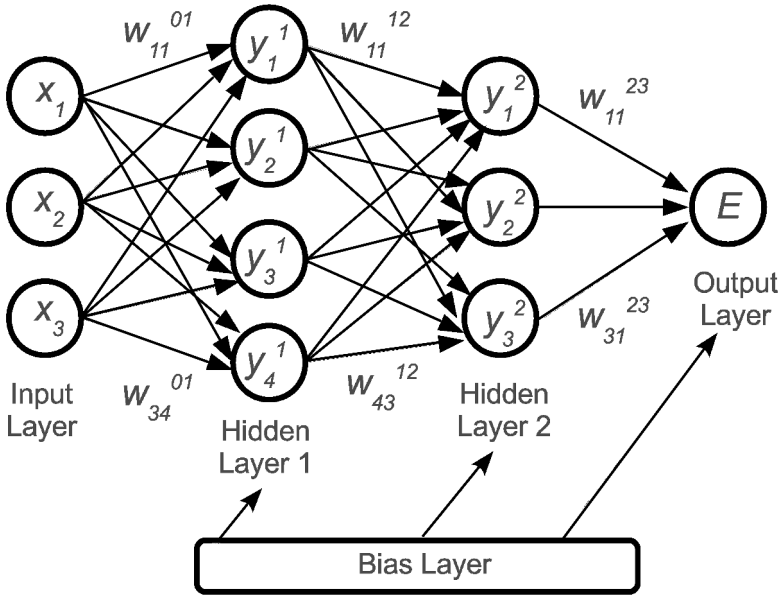

Figure 2.3: An illustration of a simple feed-forward NN model with two hidden layers.

The layers concatenated between the input layer and the output one are called hidden layers. The number of the hidden layers has to be determined for each model as well as the number of nodes of each layer. The nodes in the hidden layers provide the flexibility of NNs. As shown in Fig. 2.3, each node is connected to nodes in the previous and the following layers. These connections are called weights and each connection ($w_{j,k}^{i-1,i}$) controls the response strength of the node to the input coming from the one in the previous layer. In each node, before applying the activation function to the weighted signal from the previous layer, it is possible to apply a bias (b_j^i). Therefore, the output of the j-th node in the i-th layer can be written as

$$x_j^i = b_j^i + \sum_k w_{j,k}^{i-1,i} \cdot x_k \Rightarrow y_j^i = f_j^i(x_j^i) \tag{2.25}$$

where f_j^i is a nonlinear function, k runs over the nodes in the $(i-1)$-th layer. This is done for each node in the layer. Then, the outputs of a layer are transmitted to the following one in the network until the output layer is reached. Hence, the NN in Fig. 2.3 can be described by the following functional form:

$$E = f_1^3\left(b_1^3 + \sum_{i=1}^{3} w_{i,1}^{2,3} + f_i^2\left(b_i^2 + \sum_{j=1}^{4} w_{j,i}^{1,2} w_{j,i}^{1,2} f_j^1\left(b_j^1 + \sum_{j=1}^{3} w_{k,j}^{0,1} w_{k,j}^{0,1} x_k\right)\right)\right) \tag{2.26}$$

As anticipated, the activation functions are typically nonlinear. For this purpose, there are several possible choices such as exponential, Gaussian, trigonometric, sigmoidal and hyperbolic functions. These functions converge

to a constant number for very small or large input, which guarantees the stability of the NNs. However, their output is limited to a region, which is not necessarily that of the output values of the desired function. Therefore, one might employ a linear activation function for the output layer, data normalization techniques or shift the activation functions.

The number of parameters of the network (weights and bias) increases with the number of nodes and layers in the network itself, which increases the flexibility of the network and its capability to fit complicated functions. However, increasing the parameters of the network might lead to overfitting or learning degradation. Therefore, the number of hidden layers and nodes per layer needs to be tuned in order to guarantee the quality of the model.

The value of the weights and bias is determined in an iterative procedure during the learning process and they determine the ability of the NN to describe the function to be fitted.

For the learning process, the error backpropagation algorithm is used. In this algorithm, a loss function (also known as fitness function) is used to evaluate the quality of the prediction of NNs model and subsequently the optimization of the weights. For instance, a loss function could be the sum of squares errors between the prediction and the reference output of the function:

$$L(y_{ref}, y_{NN}) = \frac{1}{N} \sum_i (y_{ref,i} - y_{NN,i})^2 \tag{2.27}$$

where $y_{ref,i}$ is the reference output of the i-th data point, $y_{NN,i}$ is the predicated output and N is the number of data points in the dataset. As the activation functions of the NN are differentiable, so is the loss function is differentiable with respect to $y_{NN,i}$ and $y_{NN,i}$ is differentiable with respect to the parameters of the network using the chain rule. This allows minimizing the loss function (the error) by minimizing its derivative with any optimization method. In this work, we used the stochastic gradient descent algorithm [130] which consists of an iterative process in which the error is propagated backwards through the NN, the parameters are tuned, the model is reevaluated and so on until the optimization reaches a reasonable approximation.

As already discussed, by increasing the flexibility of the NNs, the learning process might result in overfitting. This happens when the model performs very well on the dataset points and poorly in the regions of the configurations spaces uncovered by the database, which corresponds to memorizing the database and not learning from it. In Fig. 2.4 we show the result of overfitting in the case of a simple polynomial fit (for the sake of visualization) where it is clear that the fitted-model predicts perfectly the dataset points and loses accuracy in the unvisited regions. In the poorly described regions, we can clearly see several fictitious local extremes. In high-dimensional functions with

sparse datasets, this problem is more pronounced. The overfitting might be avoided by separating a fraction of the dataset (testing set) and using this set to evaluate the quality of the model in the unvisited regions during the optimization process. As far as the errors on the data points employed for the optimization (training set) and the test set are the same, no overfitting issues are supposed to be present. Moreover, one might tune the so-called learning rate of the NNs during the optimization to slow down the evolution of the parameters as the learning process proceeds. This allows the parameters to change rapidly only during the early stage of training in order to find an optimal parametric region in the parameters space. After that, the parameters are allowed to change marginally to tune the finer details of the NNs without changing dramatically the model to prevent overfitting.

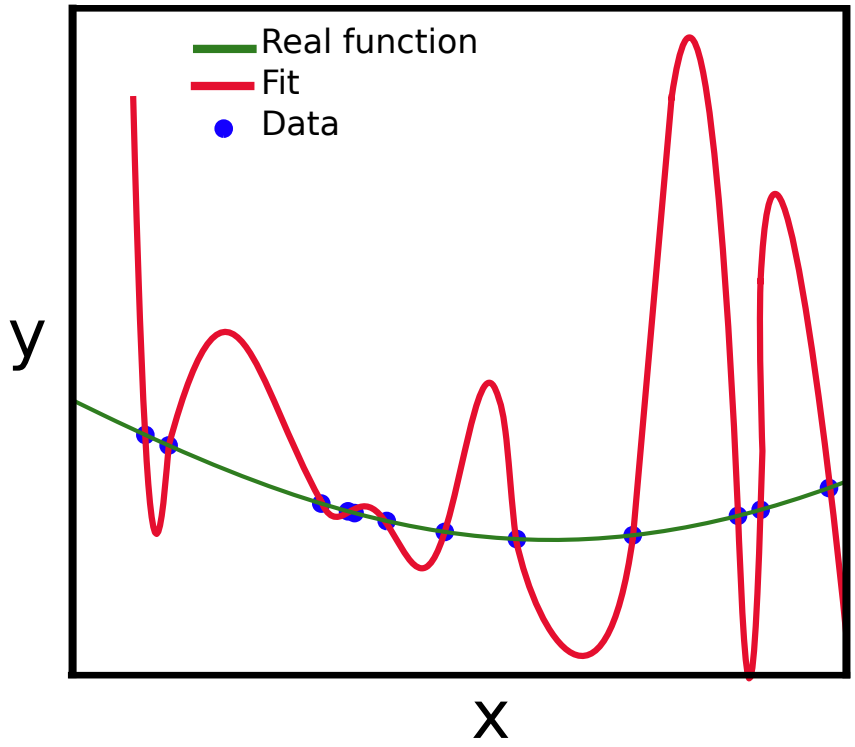

Figure 2.4: A schematic illustration of the overfitting of the desired function. Regions covered by the database are well described by the model. As far as the model exits these regions, the inference quality drops abruptly.

Residual neural network

Deep feed-forward NNs with a large number of hidden layers are tough to be optimized and suffer from learning degradation (see Fig. 2.5), vanishing gradients during the optimization and information loss through the network. For example, the learning degradation (also known as accuracy saturation) occurs when models with more layers display higher training errors than models with fewer layers. In order to deal with these problems, residual neural networks [131] (which are a subclass of feed-forward NN) have been proposed. Residual

NNs have skip connections (highway for the information) between layers, which allows a better propagation of the information in deep architectures. Mathematically, the residual connections correspond to the identity operation, hence, no more parameters in the network are required for their implementation. An illustration of the residual connections is shown in Fig. 2.6 and the resulting functional form of a node with a residual connection is similar to Eq. 2.25 and reads:

$$y_j^i = \sum_k x_k + f(b_j^i + \sum_k w_{j,k}^{i-1,i} \cdot x_k) \tag{2.28}$$

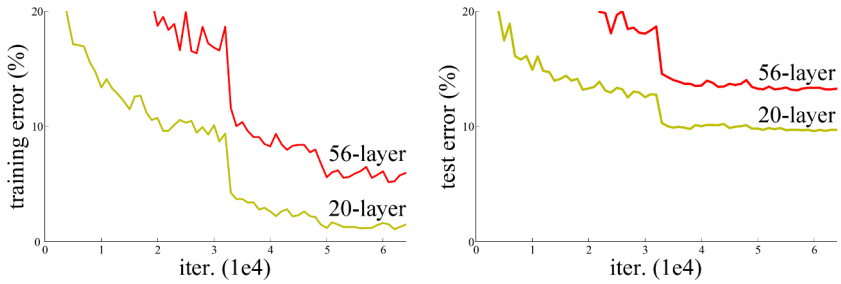

Figure 2.5: Training error (left) and test error (right) on NN models with 20 and 56 layers. The deeper network exhibits higher training and test error due to the learning degradation phenomena. Taken from [131].

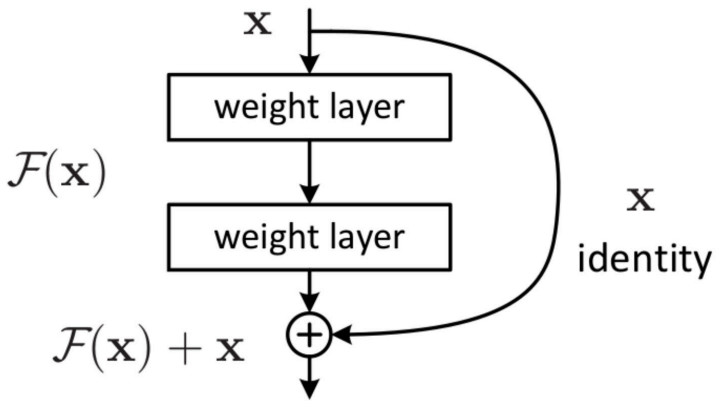

Figure 2.6: A schematic representation of a residual connection. Adapted from [131].

2.5.2 Neural network for potential energy surfaces

Today, there are several flavors proposed for NNs as approximators of the PES by fitting databases obtained from electronic structure calculations. The very first NN method for a condensed matter system was proposed by Blank et

al. [132] in the mid '90s. This work explored an interpolation method for low-dimensional PES of molecular systems to build an interatomic potential starting from a small dataset (or examples) with a feed-forward NN. The input (also known as descriptors) of the network was the position and the orientation of a molecule on a surface while the output was the total energy of the system. However, this first approach had a huge limitation as the NN was optimized for a fixed number of degrees of freedom (fixed number of atoms). Hence, once the network is optimized it is not possible to study systems of different sizes. A step forward to relax the limitations of this NN method by extending the NNs to high-dimensional ones was proposed in Ref. [133] with an analytical form similar to that of Tersoff [134] potential. The improvement of this new scheme is due to the factorization of the total energy into atomic energies, which allows addressing an arbitrary system size. Even if the number of inputs of the network is still fixed, the local environment of each atom can be evaluated separately to compute its atomic energy and therefore the total energy is given by:

$$E = \sum_i E_i \tag{2.29}$$

where E is the total energy, i is the atomic index and E_i is the atomic energy (the outputs of the modified Tersoff potential). The accuracy of this scheme is, however, limited as the functional form chosen considers only a few neighbors for each central atom and it displays low flexibility to address the possible chemical bonding variations. A few years later, a generalized neural-network method has been proposed by Behler and Parrinello [18], which inherits the idea of factorizing the energy into atomic contributions and improves the description of the atomic environments. In fact, in all the previous works the input of the NN (atomic descriptors) was typically inspired by the problem which caused limitations of the method and broke some physical symmetries (i.e. permutation, translational and rotational). The work of Behler and Parrinello [18] addressed this problem by suggesting generalized descriptors called symmetry functions G_i.

The symmetry functions proposed in Ref. [18] encode in a smooth manner the local chemical environment up to a given cutoff (r_c) according to the following cutoff function:

$$f_c(r_{ij}) = \begin{cases} 0.5[cos(\frac{\pi r_{ij}}{r_c} + 1) & for\ r_{ij} < r_c \\ 0 & for\ r_{ij} > r_c \end{cases}$$

where $\mathrm{r}_i j = |\overrightarrow{r_i} - \overrightarrow{r_j}|$, i is the central atom and j is a neighboring atom. The symmetry functions proposed in the Behler-Parrinello scheme include radial and angular information about the arrangement of neighbors around the central atoms and they belong to the two families two-body radial and three-body angular symmetry functions which were built in such a way that:

(1) Two structures with different energies give rise to different sets of symmetry function values.
(2) Symmetry functions yield the same set of values for identical local environments.
(3) The size of the input vector of the NN is independent of the number of neighboring atoms.
(4) The symmetry functions are invariant with respect to translation, rotation, and permutation.

With this in mind the following radial symmetry function was proposed in Ref [18]:

$$G_i^R = \sum_{j \neq i}^{all} e^{-\eta(r_{j,i}-r_s)^2} f_c(r_{j,i}) \tag{2.30}$$

where $\mathbf{r}_{j,i} = r_j - r_i$, η and r_s are Gaussian parameters. The angular symmetry function is given instead by:

$$G_i^R = \sum_{k,j \neq i}^{all} (1 + \lambda \cos\theta_{ijk}) e^{-\eta(r_{j,i}^2 + r_{j,k}^2 + r_{k,i}^2} f_c(r_{j,i}) f_x(r_{j,k}) f_x(r_{k,i}) \tag{2.31}$$

where $\theta_{ijk} = \frac{r_{j,i} r_{k,i}}{r_{j,i} r_{k,i}}$, λ, η, and ζ are parameters to be optimized for each symmetry function (also for the radial one) during the development of the interatomic potential. However, the symmetry functions proposed in Ref. [18] have some drawbacks. For instance, the number of symmetry functions required as input increases exponentially with the number of chemical species of the system of interest. The optimization of such a large number of symmetry functions is not a straightforward task. Indeed, a few years after Behler and Parrinello, Bartók et al. suggested new descriptors (bispectrum of the neighbor density) [127], which depend only on the raw coordinates of the atoms to reduce the human intervention for the development of NNs potential by only interpolating atomic energies. In the last decade, a lot of effort has been dedicated to the development of atomic environment descriptors and several have been proposed, such as the smooth overlap of atomic positions and the Coulomb matrix, just to name a few [135, 136].

For the development of NN interatomic potential for GST225 in this work, we have employed the automatically generated descriptors proposed in the novel approach "End-to-end Symmetry Preserving Interatomic Potential Energy Model" as implemented in the DeePMD kit [23, 24, 137]. This scheme exploits a feed-forward NN as it is the case for Ref. [18, 132], but the task of optimizing the symmetry functions is bypassed by fitting one or more NNs (known as embedded networks) whose output is the set of descriptors used as input of another NN, which fits the PES. Embedded networks are built as to preserve all the physical symmetries, as we will see later, and to reduce the complexity of developing NN interatomic potentials.

2.5.3 End-to-end neural network potentials

In "End-to-end Symmetry Preserving Interatomic Potential Energy Model" framework implemented in the DeePMD code, a general representation of the

PES based on the raw atomic coordinates has been proposed to reduce the human intervention (and effort) in developing NN interatomic potentials.

Given an atomic configuration with N atoms, $\mathbf{r} = \{\mathbf{r}_1, ..., \mathbf{r}_j, ..., \mathbf{r}_N\}$ is the set of atomic coordinates. The local environment matrix of the i-th atom, which includes the $N_{r_c}(i)$ neighbors up to a given cutoff r_c, is defined as:

$$\mathbf{R}^i = \{\tilde{\mathbf{r}}_{1,i}^T, ..., \tilde{\mathbf{r}}_{j,i}^T, ..., \tilde{\mathbf{r}}_{N_{rc}(i),i}^T\} \quad , \quad \tilde{\mathbf{r}}_{j,i} = \{S(r_{j,i}), \hat{x}_{j,i}, \hat{y}_{j,i}, \hat{z}_{j,i}\} \tag{2.32}$$

where $\mathbf{r}_{j,i} = \mathbf{r}_j - \mathbf{r}_i$, j is the index of the neighboring atom ($1 < j \leq N_{r_c}(i)$), $\hat{x}_{j,i} = \frac{x_{j,i}}{r_{j,i}}$ (similarly $\hat{y}_{j,i}$ and $\hat{z}_{j,i}$) and $S(r_{j,i})$ is a smoothing function given by:

$$S(r_{j,i}) = \begin{cases} \frac{1}{r_{j,i}} & for\ r_{j,i} < r_{cs} \\ \frac{1}{r_{j,i}}\{\frac{1}{2}[cos(\pi \frac{r_{j,i} - r_c s}{r_c - r_c s} + \frac{1}{2})\} & for\ r_{cs} < r_{j,i} < r_c \\ 0 & for\ r_{j,i} > r_c \end{cases} \tag{2.33}$$

where r_{cs} is an internal cutoff. Hence the smoothing acts only in the region included between the two cutoffs and $S(r_{j,i})$ goes to zero at the external boundary of this region.

Note that the local environment matrix $\mathbf{R}^i \in \mathbb{R}^{N_{r_c}(i) \times 4}$. The first component of $\tilde{\mathbf{r}}_{j,i}$ contains the radial information between the two atoms while the other three components contain the angular ones. Moreover, note that the size of $N_{r_c}(i)$ changes from atom to atom depending on its local environment. As $\mathbf{R}^i$ is the input of the embedding network and NNs have a fixed number of input nodes, the size of $\mathbf{R}^i$ is fixed for all atoms to $N_m = \max(N_{r_c}(i))$ in the database. In the case of atoms with a number of neighbors less than the chosen maximum, the extra rows are padded to zero.

The neighbors in the local environment matrix are ordered from the nearest to the most distant one. This choice preserves the permutation symmetry by construction in the case of a single chemical species system. For multi-chemical species systems, the neighbors are ordered considering also their chemical elements. Hence, for the first chemical species all neighbors are sorted according to their distance from the central atom, then the second chemical species and so on, as you can see in Fig. 2.7. In Fig. 2.7 we show also an example in the case of a number of neighbors less than N_m. Moreover, besides the permutation symmetry, the local environment matrix preserves also the translation symmetry as it contains only information about the distances between the i-th atom and its neighbors.

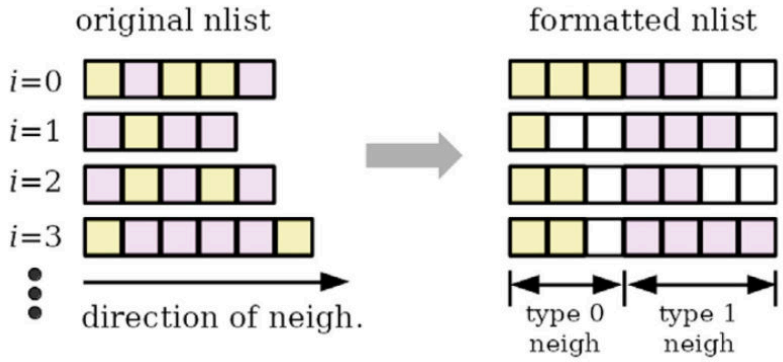

Figure 2.7: Schematic representation of the local environment matrix construction in a system with two chemical species. The neighbor list of each atom in the system (left) is ordered in the formatted neighbor list (right): first, by the chemical species (yellow and red) and then for each chemical species, the atoms are sorted according to their distance. If there are fewer atoms than the maximum number of the neighbors of that chemical species the components of the vectors in excess are set to zero (white squares). Taken from [138].

The local environments, as defined earlier, are the input of the embedded networks, which generates as output the embedding matrix $\mathrm{g}_i(\mathbf{R}^i)$. Then embedding matrices are used to compute the actual descriptors $\{\mathrm{D}_I(\mathrm{g}_i(\mathbf{R}^i))\}$ of the local environment, where I is the index of the embedding network, as we could use more than one embedding network to describe the system. These descriptors in turn are the input of the fitting network $\mathrm{F}(\{\mathrm{D}_I(\mathrm{g}_i(\mathbf{R}^i))\})$, which provides the atomic energy, and hence the total energy is given by:

$$E = \sum_i F(\{D_I(g_i(\mathbf{R}^i))\}) \tag{2.34}$$

In this thesis, we have employed two types of embedding networks: the two-body embedding, which encodes the information in the network through the column containing $\{S(r_{j,i})\}$ of the local environment matrix, and the three-body embedding, which encodes the information via the angle formed by two neighbors, as will be discussed later.

Once the set of descriptors are constructed, they are concatenated and flattened in a 1D vector, which is the input of the fitting network. The fitting network is a simple fully connected network as that discussed in Sec. 2.5.1 with the possibility to exploit the residual connections. The hidden layers have a hyperbolic tangent activation function while the output layer has a linear transform that maps the input from the previous layer into a scalar. The network parameters, together with those of the embedding networks, are optimized with the stochastic gradient descent according to the ADAM algorithm [130], where at each iterative step the network is optimized considering a randomly shuffled batch of configurations from the database. During the op-

timization the weights of the network are updated according to the following loss function:

$$L = \frac{1}{N_b}\sum_{k\in N_b}(\frac{1}{N}p_e|E^k_{NN}-E^k_{ref}|^2+p_f\frac{1}{3N}\sum_{i\alpha}|F^{k,i\alpha}_{NN}-F^{k,i\alpha}_{ref}|^2+p_\tau\frac{1}{9}\sum_{\alpha\beta}|\tau^{k,\alpha\beta}_{NN}-\tau^{k,\alpha\beta}_{ref}|^2) \tag{2.35}$$

where N_b is the batch size, k is the index of a configuration within the batch, i is the index if the i-th atom in the k-th configuration, α and β are Cartesian indexes. E_{NN} is the total energy of a system predicted by the NN while E_{ref} is the reference energy, similarly $F^{k,i\alpha}$, which are the components of the forces vectors and $\tau^{k,\alpha\beta}$, which are the components stress tensor. Finally, p_e, p_f and p_τ are hyperparameters, which control the relative importance of each term in the loss function and they correspond to the energy term, forces term and virial term. The prefactors evolve during the learning process according to the following function:

$$p_\alpha(t) = p^\alpha_{limit}[1-\frac{r_l(t)}{r^0_l}]+p^\alpha_{start}[\frac{r_l(t)}{r^0_l}] \tag{2.36}$$

where α stands for e, f and τ, p^α_{start} and p^α_{limit} are the desired initial and final values of the prefactor, r^0_l is the starting learning rate and $r_l(t)$ is the learning rate at the t-th step of optimization, where the evolution of the learning rate is given by:

$$r_l(t) = r^0_l k^{\frac{t}{t_d}} \tag{2.37}$$

where k is the decaying rate and t_d is the decay constant.

Two-body embedding

The two-body embedding matrix of the i-th atom ($g^2_i(\mathbf{R}^i)$) is a N_m x M_2 whose j-th row is given by:

$$(g^2_i)_j = (G_1(s(r_{j,i})),...,G_{M_2}(s(r_{j,i})) \tag{2.38}$$

where G is the actual embedding network that fits the radial information of the local environment matrix. G is a full connected deep NN with m+1 layers, which maps the input $s(r_{j,i})$ into M_2 outputs. G can be expressed as shown in Eq. 2.26 where the parameters (weights and bias) are optimized during the training together with the fitting network.

With the local environment and two-body embedding matrices, the actual descriptor is defined as:

$$D^2_i = \frac{1}{N^2_m}g^{2,sub}_i\mathbf{R}_i(\mathbf{R}_i)^T g^2 \tag{2.39}$$

where $g_i^{2,sub}$ is a submatrix of g_i^2. A Schematic of the evaluation process of the two body descriptors is shown in Fig. 2.8.

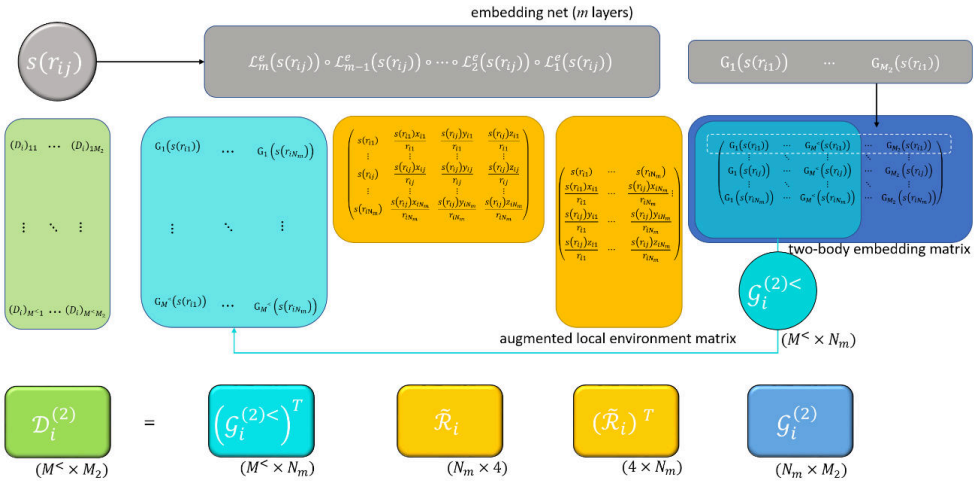

Figure 2.8: Schematic illustration of the two-body descriptor. Taken from [139].

Besides the permutation and the translation symmetries, as discussed previously, D_i^2 preserves also the rotational one. Indeed, the definition of this descriptor, given in Eq 2.39, depends only on the two-body embedding matrix and the product of the local environment matrix $(\mathbf{R}_i(\mathbf{R}_i)^T)$. As anticipated, the former depends only on the distance between atoms and hence it is invariant with respect to the rotations. The latter, $(\mathbf{R}_i(\mathbf{R}_i)^T)$, is known to be an overcomplete base, which is invariant with respect to rotation [140]. Therefore, the resulting two-body descriptor preserves the rotational symmetry.

Three-body embedding

The three-body embedding matrix displays the same spirit as the two-body embedding matrix with different input. Indeed, this matrix encodes the information of the local environment considering the angle formed by two neighboring atoms according to the following definition:

$$(\theta_i)_{jk} = (R_i(R_i)^T)_{jk} = s(r_{j,i})s(r_{k,i})\frac{\mathbf{r}_{j,i}\mathbf{r}_{k,i}}{r_{j,i}r_{k,i}} \tag{2.40}$$

which corresponds to the elements matrix of the inner product of the local environment matrix with itself. The three-body embedding is a rank three tensor and for the i-th atom $(\mathrm{g}_i^3(\theta_i)_{jk})$ it is given by:

$$(g_i^3)_{jk} = (G_1^3((\theta_i)_{jk}), ..., G_{M_3}^3((\theta_i)_{jk})) \tag{2.41}$$

where M_3 is the output size of the G^3 embedding net and similarly to G^2, the parameters of this embedding net are optimized during the learning process. Again, the actual three-body descriptor D^3 is a function of $(\theta_i)_{jk}$ and g_i^3 and it is given by:

$$D_i^3 = \frac{1}{N_m^2} \sum_{j,k=}^{N_m} (\theta_i)_{jk} (g_i^3)_{jk} \tag{2.42}$$

A schematic representation of the construction of the three-body descriptor is shown in Fig. 2.9.

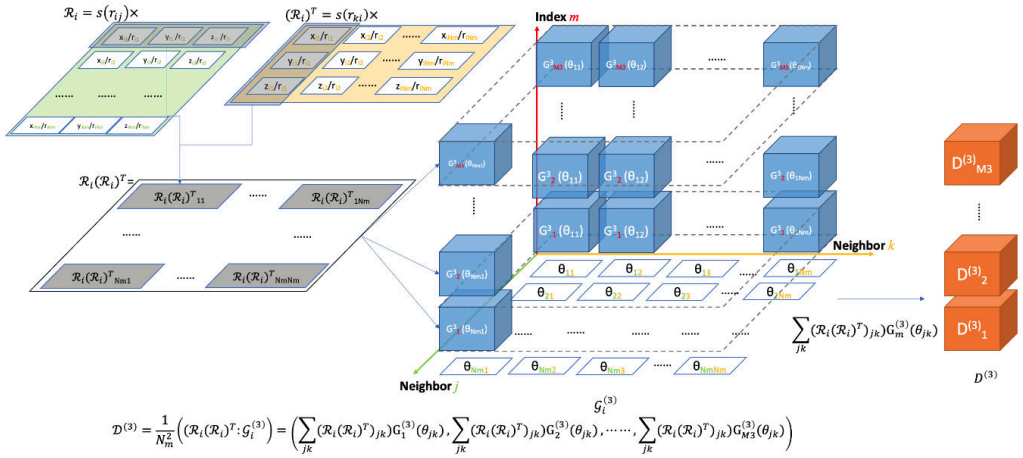

Figure 2.9: Schematic illustration of the three-body descriptor. Taken from [139].

Similarly to D^2, D^3 preserves all the required physical symmetries as it has been shown in Ref. [139] based on the arguments discussed for D^2.

Chapter 3

Atomistic simulations of Ge-rich GeSbTe alloys

Ge-rich GST alloys are promising candidates for embedded memories applications. These alloys display a crystallization temperature higher than that of the prototypical GST225 compound as discussed in Sec. 1.3. The enhancement of the amorphous stability has been ascribed to a non homogeneous crystallization process resulting in the formation of crystalline Ge and less Ge-rich GST alloys. The long scale mass transport of Ge involved in this process slows down the crystallization process that leads to a high T_x. However, the resulting inhomogeneity comes with several drawbacks for the operation of PCMs such as a high cell-to-cell variability and a resistance drift with time in the SET state of the memory. Although great efforts have been devoted to the elucidation of the crystallization process of Ge-rich GST, many details are still unknown. A better understanding of this process is, on the other hand, mandatory to better tune the composition of the alloy to mitigate the detrimental effects of the phase separation.

As a first attempt to better understand the decomposition process, we studied by DFT simulations the evolution of the structure of the amorphous phase by increasing the Ge content. Secondly, we investigated the thermodynamics of the decomposition reaction of non stoichiometric GST alloys into the crystalline products.

To study the evolution of the structural properties of the amorphous phase of GST alloys we generated several DFT models with compositions along the Ge-Sb_2Te_3 and GeSb-GST225 lines by quenching from the melt to 300 K. On the other hand, to study the decomposition pathways of GST alloys we computed the DFT formation free energy of the cubic crystalline phase for all compositions in the central part of the ternary phase diagram. Then, with this information, we computed the convex hull of the Ge-Sb-Te phase diagram which is the 2D surface formed by the most stable compounds in the ternary system. The vertical distance between the formation free energy of a given

composition and the convex hull is a measure of the metastability of the alloy. This information is then employed to compute the reaction free energy of the decomposition reactions for any GST alloy, which provided information on the compositions that most likely appear during the crystallization process.

In the first section of this chapter, we discuss the results on the amorphous phase of Ge-rich GST alloys while in the second section we report the high-throughput DFT study of the decomposition pathways of GST alloys in the crystalline phase. The detailed analysis on the structural properties of the amorphous phase reported in Sec. 3.1 and the thermodynamical data on the decomposition process discussed in Sec. 3.2 will be exploited to propose a possible strategy for the optimization of the alloy composition as will be discussed in Sec. 3.2.5.

Most of the results reported in Sec. 3.1.2 on the structural, electronic and vibrational properties of Ge-rich GST alloys have been published in our previous works [109, 141].

3.1 The amorphous phase of non stoichiometric GeSbTe alloys

To investigate the evolution of the structural properties of non stoichiometric GST alloys with the fraction of Ge we chose compositions along the $GeSb_2Te_3$ tie-line and along the GeSb-GST225 line. More precisely, we modeled $Ge_5Sb_2Te_3$ (GST523), $Ge_4Sb_2Te_3$ (GST423) and $Ge_3Sb_2Te_3$ (GST323) which were studied experimentally in Ref. [13] and display a T_x in the range between 500 and 570 K. Along GeSb-GST225 line, we considered the $Ge_2Sb_2Te_1$ (GST221) to study the evolution of the structure with an equal enrichment of Ge and Sb. Structural data of the amorphous phase of $Ge_1Sb_1Te_1$ (GST111) isoelectronic composition along the GeSb-GST225 are already available in literature [142] to be compared with GST221. In Fig. 3.1 we show the two lines investigated here superimposed to the experimental map of T_x temperature from Ref. [13]. Note that henceforth, a $Ge_XSb_YTe_Z$ composition will be simply named GSTXYZ.

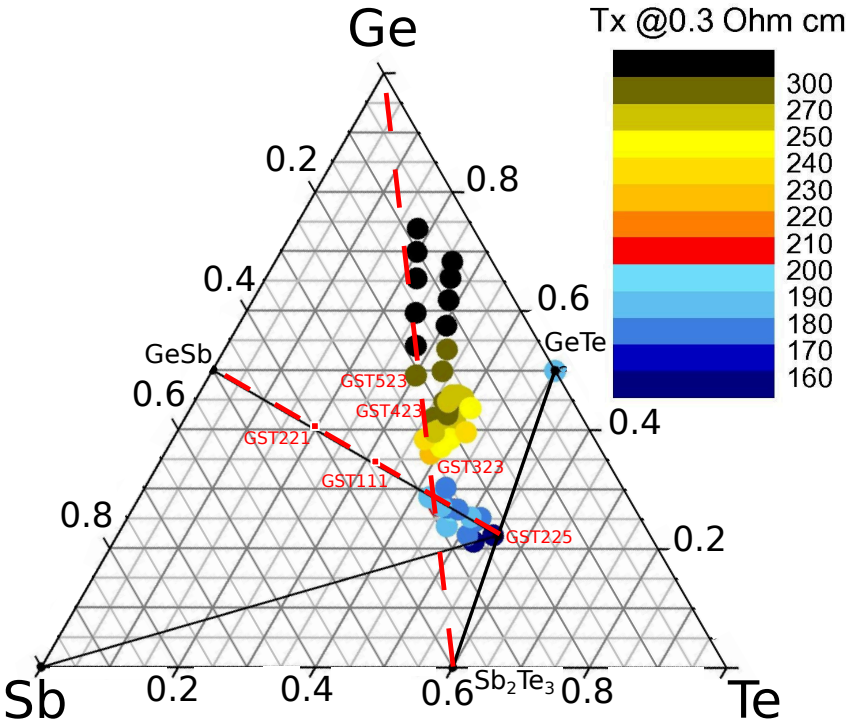

Figure 3.1: The compositions of the amorphous phase investigated here (red symbols on the red dashed lines) in the ternary phase diagram. Compositions investigated experimentally in Ref. [13] are shown by dots with a color assigned by their T_x (color scale aside in °C).

3.1.1 Computational details

The models of amorphous GST alloys have been generated by quenching from the melt in a cubic 216-atom supercell. In the lack of experimental data on the density of the liquid and amorphous phases of non stoichiometric compositions, we chose as initial density a value 8% lower than that of the theoretical equilibrium density of the crystalline phase of the Ge-rich GST alloys, as it is the case for GST225 [143]. To this end, we have first computed the equation of state for the desired compositions in the crystalline phase where we have assumed that Ge-rich GST alloys might exist in the cubic NaCl geometry. More details regarding the initial configuration for our cubic models are discussed in Appendix A. The crystalline models are also used to compute the decomposition free energy as we will discuss in Sec. 3.2.

For the MD simulations, we used the CP2k package [144] which implements the quickstep scheme for the solution of the KS equation (see Sec. 2.1.3). We used the GGA exchange and correlation functional due to Perdew, Burke and Enzerhof (PBE) [115] and norm conserving pseudopotentials due to Goedeker, Teter and Hutter (GTH) [119]. The auxiliary basis set of plane waves was expanded up to a kinetic energy cutoff of 100 Ry while KS orbitals were expanded with Gaussian-type orbitals of a valence triple-zeta polarization basis

set. The semiempirical correction due to Grimme [145] was used to include van der Waals (vdW) interactions, as there is evidence that their inclusion is important for a proper description of the structural properties of liquid and amorphous GeTe and GST225 [146, 147]. The Brillouin zone integration was restricted to the 216-atoms supercell Γ-point for the MD simulations and geometry optimization. Equilibrium geometries, densities and total energies at zero temperature were obtained by full relaxation of the atomic positions and cell edges. DFT molecular dynamics simulations in the BO approximation were performed with a timestep of 2 fs. A similar framework was employed in previous works on several other phase change compounds [74]. The liquid was generated by heating the crystalline models (at a density 8% less dense than the equilibrium density of the crystal) at 2000 K for 2 ps. Then the system has been thermalized at 1000 K for other 2 ps. Finally, it has been quenched in almost 100 ps to 300 K in constant pressure constant temperature (NPT) simulations in order to get the equilibrium density at normal conditions. Only isotropic changes of the cell were allowed in the NPT simulations. The system was quenched by decreasing temperature in a stepwise manner from 1000 K to 300 K according to the protocol shown in Fig. 3.2. The average volume of a NPT simulation 3.5 ps long at 300 K yields the equilibrium volume of the amorphous phase at the 300 K. Then, a NVT simulation 12 ps long was run to compute the average structural properties at 300 K. Finally, the equation of state at zero temperature was computed for each model by optimizing the atomic positions for several volumes and by fitting the resulting energies with a Birch-Murnaghan function [148]:

$$E(V) = E_0 + \frac{9V_0B_0}{16}\left\{\left[(\frac{V_0}{V})^{\frac{2}{3}} - 1\right]^3 B_0' + \left[(\frac{V_0}{V})^{\frac{2}{3}} - 1\right]^2\left[(6 - 4\frac{V_0}{V})^{\frac{2}{3}}\right]\right\} \quad (3.1)$$

where E_0 is the equilibrium internal energy, V_0 is the equilibrium volume, B_0 is the bulk modulus and B_0' is the derivative of the bulk modulus with respect to pressure. The resulting equation of state for Ge-rich GST alloys yield a density of 0.0338, 0.0371, 0.0331, and 0.0323 atoms/Å^3 for GST523, GST423, GST323, and GST221.

The ground state configurations were employed to compute the phonon frequencies, the electronic density of states and Raman spectra. The Raman spectra are computed in the backscattering geometry with nonpolarized light within the BPM [121] developed for GST alloys [122] (see Sec. 2.23) by employing the DFT phonons obtained numerically by finite atomic displacements 0.0053 Å large.

The electronic density of states (DOS) was computed by using the code Quantum-Espresso (QE) [149] from KS energies broadened with a Gaussian function with variance of 35 meV over a 10 × 10 × 10 k-point mesh.

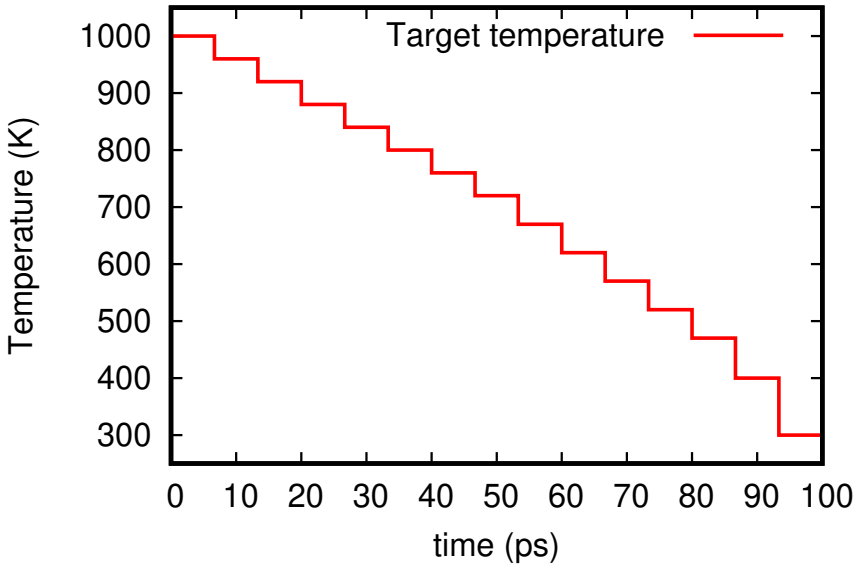

Figure 3.2: Evolution in time of the target temperature of the thermostat in the quenching protocol for the generation of amorphous GST alloys. The temperature jumps were 40, 50, and 70 K in the range 1000-720 K, 720-470 K and 470-400 K. Finally, the last simulation was carried out at 300 K. Each simulation at constant temperature is 6.6 ps long.

3.1.2 Structural properties

The total and partial correlation functions of the amorphous GST alloys DFT models along the Ge-Sb_2Te_3 and GeSb-$Ge_2Sb_2Te_5$ at 300 K are compared in Fig. 3.3.

The distribution of coordination numbers of Ge-rich GST alloys in the amorphous phase, reported in Fig.3.4, were obtained by integrating the partial pair correlation functions up to a bonding cutoff set to 3.2 Å for all pairs but for the Sb-Te cutoff, which is set to 3.4 Å (see Fig. 3.3) for the sake of comparison with previous work on GST225 [70] and GST111 [142], whose data are shown in Fig. 3.4.

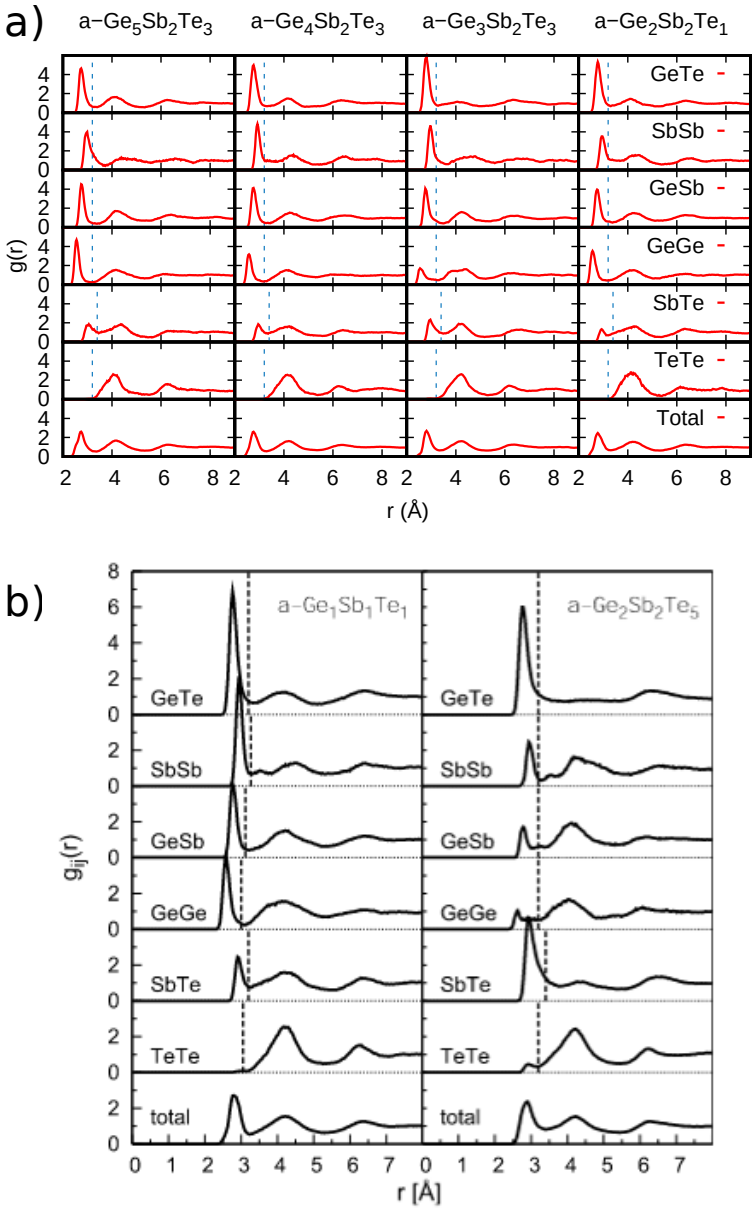

Figure 3.3: Total and partial pair correlation functions of amorphous Ge-rich GST alloys at 300 K. The dashed lines indicate the bonding cutoff used to define the coordination numbers. a) Data for GST523, GST423, GST323 and GST221. The figure is adapted from our previous work [109]. b) Data for GST225 from Ref. [70] and GST111 from Ref. [142].

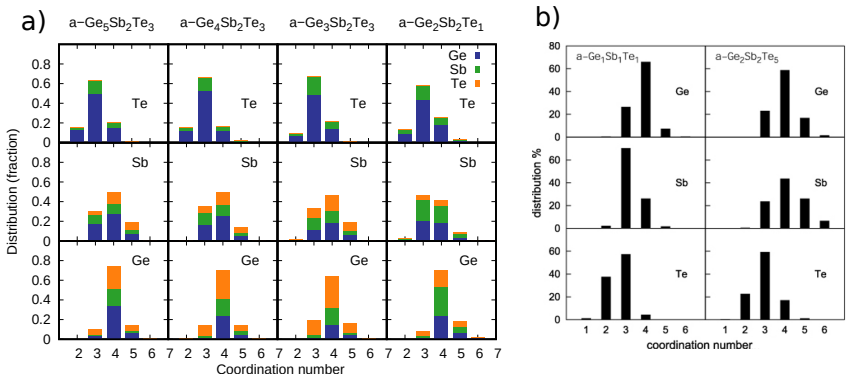

Figure 3.4: a) Distribution of the coordination numbers of amorphous Ge-rich GST alloys by using the bonding cutoff defined by the partial pair correlation functions in Fig. 3.3. Figure taken from our previous work [109]. b) Data for amorphous GST225 and GST111 taken from [70, 142].

The average partial coordination numbers for each atomic species for alloys on Ge-Sb_2Te_3 and on GeSb-GST225 lines are given in Tab. 3.1 and Tab. 3.2. Ge is mainly four-coordinated and Te is three-coordinated as it is the case for GST225.

Table 3.1: Average coordination numbers for different pairs of atoms in amorphous Ge-rich alloys along the Ge-Sb_2Te_3 tie-line. Data taken from our previous work [109].

	-	Total	With Ge	With Sb	With Te
GST523	Ge	4.06	1.82	0.83	1.41
	Sb	3.88	2.04	0.88	0.96
	Te	3.06	2.39	0.66	0.01
	-	Total	With Ge	With Sb	With Te
GST423	Ge	4.01	1.31	0.91	1.79
	Sb	3.80	1.82	1.00	0.98
	Te	3.04	2.39	0.65	0.00
	-	Total	With Ge	With Sb	With Te
GST323	Ge	4.00	0.82	0.96	2.22
	Sb	3.85	1.43	1.07	1.35
	Te	3.15	2.22	0.90	0.03

Table 3.2: Average coordination numbers for different pairs of atoms in amorphous Ge-rich alloys along the GeSb-GST225 line. The data for amorphous GST111 and GST225 are taken from our previous work Ref. [142].

	-	Total	With Ge	With Sb	With Te
GST221	Ge	4.15	1.38	1.60	1.17
	Sb	3.58	1.60	1.52	0.46
	Te	3.18	2.29	0.89	0.00
	-	Total	With Ge	With Sb	With Te
GST111	Ge	3.81	0.88	1.01	1.91
	Sb	3.27	1.01	1.54	0.72
	Te	2.65	1.91	0.72	0.02
	-	Total	With Ge	With Sb	With Te
GST225	Ge	3.96	0.29	0.36	3.31
	Sb	4.15	0.36	0.43	3.36
	Te	2.97	1.33	1.34	0.30

The analysis of the bonding geometry in the amorphous phase obtained from the bond angle distribution function (see Fig. 3.5) suggests the presence of octahedral-like and tetrahedral geometries. Indeed, the broad peak at 90° and the weaker structure around 170° for Ge and Sb are typical features of defective octahedral-like geometries while the peak around 109° for Ge atoms is instead due to tetrahedral geometries.

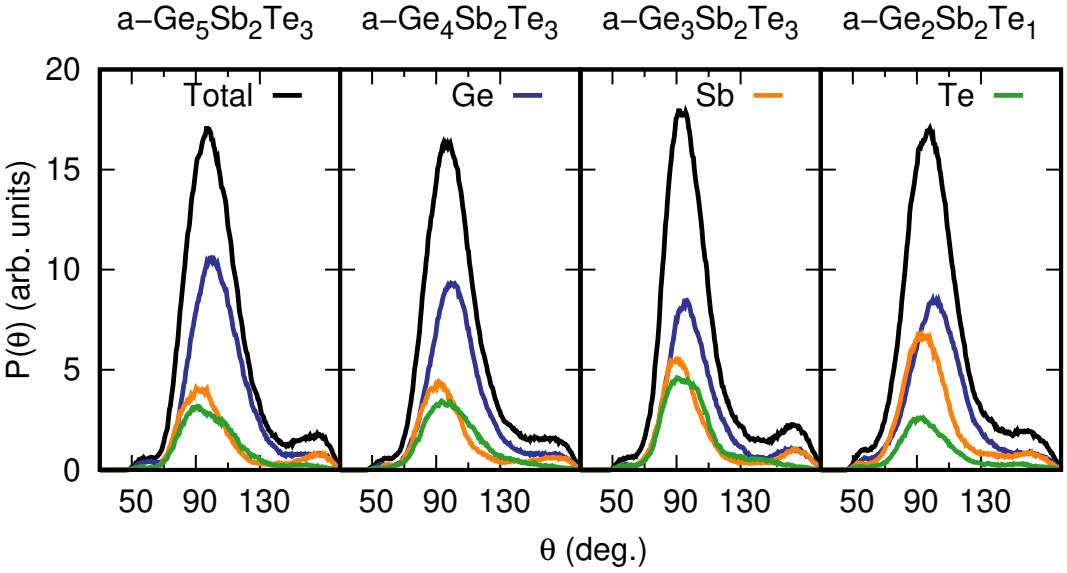

Figure 3.5: Bond angle distribution function of amorphous Ge-rich GST alloys at 300 K. The total distribution and the distributions resolved for the different types of the central atom are shown. Taken from our previous work [109].

The fraction of the different types of bonds for each alloy along Ge-Sb_2Te_3

and on GeSb-GST225 lines are given in Tab. 3.3. As expected, the fraction of Ge-Ge homopolar bonds increases by increasing the fraction of Ge in the alloy.

Table 3.3: Percentage fraction (%) of the different types of bonds in Ge-rich amorphous alloys along the Ge-Sb_2Te_3 and GeSb-GST225 lines. Data taken from our previous work [109] and from Ref. [142] for GST111 and GST225.

	-	Ge	Sb	Te
GST523	Ge	24.4	-	-
	Sb	22.2	4.8	-
	Te	37.9	10.5	0.1
	-	Ge	Sb	Te
GST423	Ge	15.9	-	-
	Sb	22.2	6.1	-
	Te	43.7	11.9	0.1
	-	Ge	Sb	Te
GST323	Ge	8.4	-	-
	Sb	19.6	7.3	-
	Te	45.6	18.5	0.3
	-	Ge	Sb	Te
GST221	Ge	14.7	-	-
	Sb	34.1	16.2	-
	Te	25.0	9.7	0.0
	-	Ge	Sb	Te
GST111	Ge	9.1	-	-
	Sb	20.9	15.8	-
	Te	39.2	14.8	0.2
	-	Ge	Sb	Te
GST225	Ge	0.9	-	-
	Sb	7.9	2.8	-
	Te	43.4	45.1	4.1

The distribution of coordination environments for each species resolved by coordination number in the amorphous phase of GST523, GST423, GST323, and GST221 are shown in Tabs 3.4–3.7. The analysis of these local environments indicates that, despite the large fraction of Ge-Ge homopolar bond present in these alloys, no partial segregation of Ge is present because the fraction of Ge-Ge_4 environment is negligible.

Table 3.4: Distribution of Ge, Sb and Te coordination environments for atoms with different coordination number in amorphous GST523. Environments in a fraction less than 1% are not reported. Taken from our previous work [109].

Central atom	Coordination number			
	2	3	4	5
Ge:		Ge_2Sb 1.13% Ge_2Te 1.18% $GeTe_2$ 4.34% Te_3 1.26%	Ge_4 2.01% Ge_3Sb 3.77% Ge_2Sb_2 7.64% $GeSb_2Te$ 7.28% Sb_2Te_2 1.35% Ge_2SbTe 14.3% $GeSbTe_2$ 11.5% $SbTe_3$ 1.65% Ge_3Te 10.7% Ge_2Te_2 10.4% $GeTe_3$ 1.35%	Ge_4Sb 1.55% Ge_3SbTe 1.67% Ge_2SbTe_2 2.43% $GeSbTe_3$ 1.86% Ge_3Te_2 1.67% Ge_2Te_3 1.44%
Sb:		Ge_3 3.88% Ge_2Sb 12.1% $GeSb_2$ 5.74% GeSbTe 4.81% Ge_2Te 1.99% $GeTe_2$ 1.25%	Ge_4 6.27% Ge_3Sb 9.79% Ge_2Sb_2 5.43% $GeSb_2Te$ 4.19% Ge_2SbTe 6.75% $GeSbTe_2$ 2.17% Ge_3Te 1.90% Ge_2Te_2 7.59% $GeTe_3$ 3.85%	Ge_2Sb_2Te 2.18% Ge_3SbTe 2.09% Ge_2SbTe_2 5.75% Ge_2Te_3 4.09% $GeTe_4$ 1.12%
Te:	Ge_2 11.9% GeSb 3.60%	Ge_3 28.2% Ge_2Sb 29.4% $GeSb_2$ 4.49%	Ge_4 7.55% Ge_3Sb 5.30% Ge_2Sb_2 4.76% $GeSb_3$ 2.11%	

Table 3.5: Distribution of Ge, Sb and Te coordination environments for atoms with different coordination number in amorphous GST423. Environments in a fraction less than 1% are not reported. Taken from our previous work [109].

Central atom	Coordination number			
	2	3	4	5
Ge:		$GeTe_2$ 3.42% $SbTe_2$ 3.09% Te_3 5.30%	Ge_4 1.39% Ge_3Sb 3.19% Ge_3Te 4.43% Ge_2Sb_2 2.49% Ge_2SbTe 10.17% Ge_2Te_2 8.69% $GeSb_2Te$ 10.05% $GeSbTe_2$ 7.84% $GeTe_3$ 7.37% Sb_4 1.01% Sb_3Te 2.06% Sb_2Te_2 3.23% $SbTe_3$ 4.23% Te_4 3.67%	Ge_3SbTe 1.97% Ge_2SbTe_2 2.55% $GeSb_2Te_2$ 1.00% $GeSbTe_3$ 1.10% $GeTe_4$ 1.20%
Sb:		Ge_3 1.35% Ge_2Sb 12.90% Ge_2Te 3.82% $GeSb_2$ 6.21% GeSbTe 2.80% $GeTe_2$ 1.25% Sb_2Te 3.60% $SbTe_2$ 1.82%	Ge_4 2.70% Ge_3Sb 12.66% Ge_3Te 4.45% Ge_2Sb_2 4.01% Ge_2SbTe 3.81% Ge_2Te_2 8.28% $GeSb_2Te$ 4.02% $GeSbTe_2$ 3.55% $GeTe_3$ 1.22% Sb_3Te 1.43% Sb_2Te_2 1.26% $SbTe_3$ 1.58%	Ge_5 1.40% Ge_3Te_2 1.31% Ge_2SbTe_2 1.61% Ge_2Te_3 1.27% $GeSb_2Te_2$ 2.59% $SbTe_4$ 1.44%
Te:	Ge_2 9.262% GeSb 5.998%	Ge_3 34.32% Ge_2Sb 23.98% $GeSb_2$ 7.355%	Ge_4 6.11% Ge_3Sb 4.74% Ge_2Sb_2 4.02% $GeSb_3$ 1.51%	

Table 3.6: Distribution of Ge, Sb and Te coordination environments for atoms with different coordination number in amorphous GST323. Environments in a fraction less than 1% are not reported. Taken from our previous work [109].

Central atom	Coordination number			
	2	3	4	5
Ge:		GeSbTe 1.88	Ge_3Sb 2.46	Ge_3SbTe 1.55
		$GeTe_2$ 2.41	Ge_2SbTe 8.86	Ge_2SbTe_2 2.18
		$SbTe_2$ 4.79	Ge_2Te_2 3.72	Ge_2Te_3 2.28
		Te_3 8.52	$GeSb_2Te$ 4.57	$GeSbTe_3$ 2.00
			$GeSbTe_2$ 9.53	$GeTe_4$ 2.31
			$GeTe_3$ 9.79	$SbTe_4$ 2.50
			Sb_3Te 7.08	
			Sb_2Te_2 6.86	
			$SbTe_3$ 7.60	
			Te_4 3.50	
Sb:		Ge_2Sb 4.22	Ge_4 3.12	Ge_3Te_2 2.00
		Ge_2Te 6.38	Ge_3Sb 3.52	Ge_2Sb_2Te 1.11
		$GeSb_2$ 3.71	Ge_3Te 5.34	Ge_2SbTe_2 1.95
		GeSbTe 6.25	Ge_2Sb_2 5.06	$GeSb_2Te_2$ 2.36
		$GeTe_2$ 2.43	Ge_2SbTe 1.83	$GeSbTe_3$ 1.90
		Sb_3 3.75	Ge_2Te_2 3.17	$GeTe_4$ 1.96
		Sb_2Te 1.83	$GeSb_3$ 1.19	$SbTe_4$ 2.40
		$SbTe_2$ 4.27	$GeSb_2Te$ 2.00	
			$GeSbTe_2$ 10.3	
			$GeTe_3$ 4.00	
			Sb_2Te_2 2.43	
			$SbTe_3$ 2.50	
Te:	Ge_2 5.81	Ge_3 27.9	Ge_4 4.94	
	GeSb 3.23	Ge_2Sb 26.7	Ge_3Sb 7.82	
		$GeSb_2$ 9.11	Ge_2Sb_2 3.24	
		Sb_3 2.52	$GeSb_3$ 3.96	

Table 3.7: Distribution of Ge, Sb and Te coordination environments for atoms with different coordination number in amorphous GST221. Environments in a fraction less than 1% are not reported. Taken from our previous work [109].

Central atom	Coordination number			
	2	3	4	5
Ge:		GeSbTe 1.05%	Ge_3Sb 4.55%	Ge_3Te_2 1.40%
		$GeTe_2$ 1.96%	Ge_2Sb_2 12.81%	Ge_2Sb_3 1.13%
		$SbTe_2$ 1.50%	Ge_2SbTe 5.47%	Ge_2Sb_2Te 2.82%
		Te_3 1.86%	Ge_2Te_2 4.58%	Ge_2SbTe_2 2.57%
			$GeSb_3$ 7.69%	$GeSb_3Te$ 1.57%
			$GeSb_2Te$ 15.2%	$GeSb_2Te_2$ 1.61%
			$GeSbTe_2$ 6.54%	$GeSbTe_3$ 1.41%
			$GeTe_3$ 4.28%	
			Sb_4 2.25%	
			Sb_3Te 1.86%	
			Sb_2Te_2 2.34%	
			$SbTe_3$ 1.67%	
Sb:		Ge_3 5.28%	Ge_4 2.59%	Ge_4Sb 1.40%
		Ge_2Sb 9.94%	Ge_3Sb 4.97%	Ge_3Sb_2 1.21%
		Ge_2Te 3.19%	Ge_3Te 2.68%	
		$GeSb_2$ 13.41%	Ge_2Sb_2 10.37%	
		GeSbTe 6.45%	Ge_2SbTe 2.74%	
		Sb_3 4.01%	$GeSb_3$ 5.59%	
		Sb_2Te 2.75%	$GeSb_2Te$ 6.05%	
			$GeSbTe_2$ 2.06%	
			Sb_3Te 1.67%	
Te:	Ge_2 5.88%	Ge_3 21.34%	Ge_4 5.56%	Ge_3Sb_2 1.27%
	GeSb 6.06%	Ge_2Sb 28.66%	Ge_3Sb 11.67	
	Sb_2 1.24%	$GeSb_2$ 7.31%	Ge_2Sb_2 7.52%	
			$GeSb_3$ 1.33%	

A quantification of the fraction of Ge atoms in a tetrahedral environment can be obtained from the distribution of the q-parameter [150] defined by:

$$q = 1 - \frac{3}{8}\Sigma_{i<k}(\frac{1}{3} + cos(\theta_{ijk}))^2 \tag{3.2}$$

where the sum runs over the couples of atoms bonded to a central atom j and forming a bonding angle θ_{ijk}. The order parameter evaluates to $q = 1$ for the ideal tetrahedral geometry and $q = 5/8$ for a four-coordinated defective octahedral site. The integration of the q distribution of the four-coordinated Ge atoms from 0.8 to 1.0 gives a measure of the fraction of Ge atoms tetrahedrally coordinated as it was shown in Ref. [142]. The distribution of q parameter for Ge, Sb and Te atoms resolved for different atomic coordination in amorphous GST523, GST423, GST323 and GST221 are given in Fig. 3.6. From these results, we get that the fraction of tetrahedral Ge amounts to: 55% in GST523, 49% in GST423, 35% in GST323, and 51% in GST221. In GST225 almost 33% of Ge atoms occupy a tetrahedral environment while in GST111 this fraction raises to 45%. Therefore, we clearly see that along the Ge-Sb_2Te_3 tie-line, the fraction of tetrahedral Ge increases together with the content of Ge. The same holds for alloys along the GeSb-$Ge_2Sb_2Te_5$ line by increasing the fraction of GeSb.

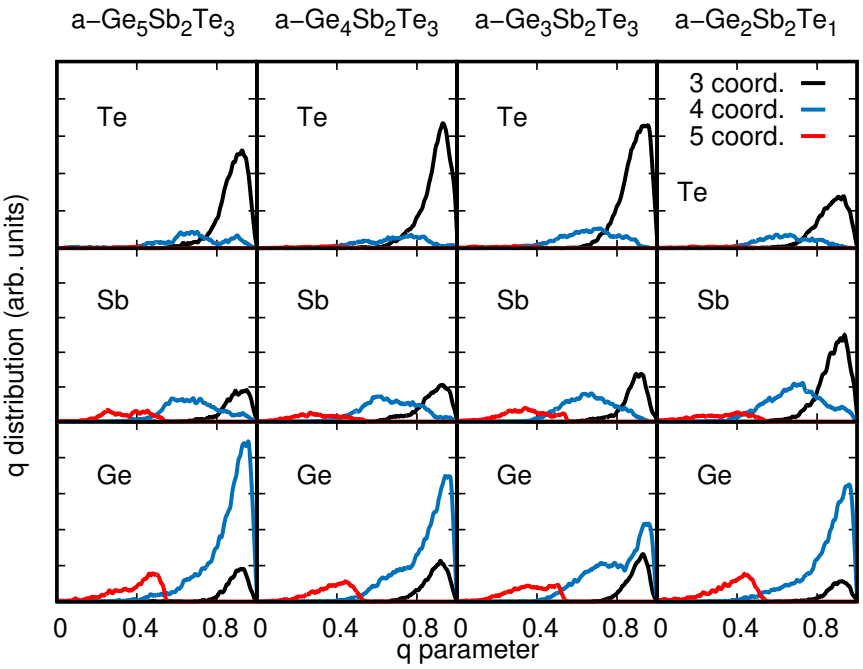

Figure 3.6: Distribution of the local order parameter q resolved for atomic species and coordination number for amorphous Ge-rich GST alloys. The continuous smooth distribution is the result of Gaussian broadening of the order parameter for individual atoms. Taken from our previous work [109].

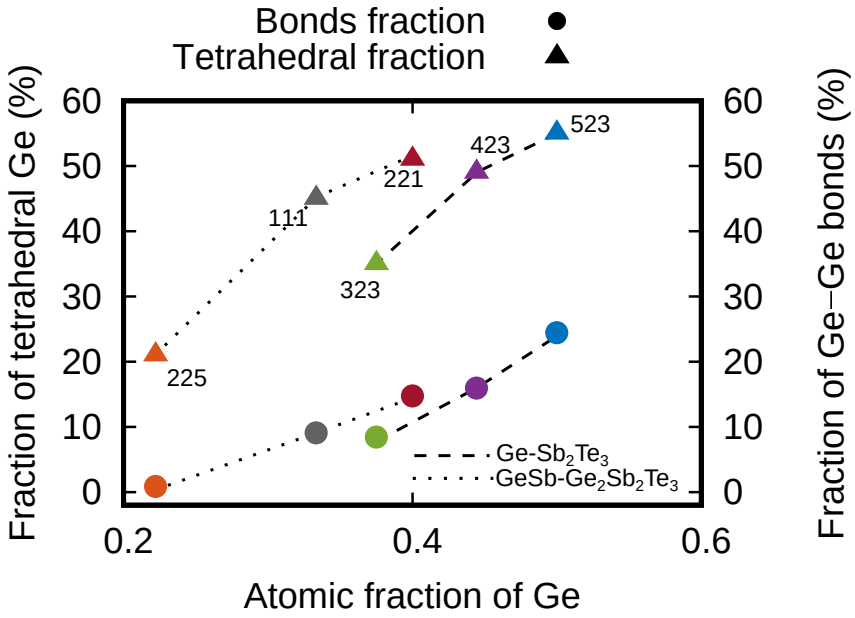

Figure 3.7: Fraction of Ge atoms in tetrahedral geometry (triangles) and fraction of Ge-Ge homopolar bonds (circles) over the total number of bonds in amorphous Ge-rich GST alloys along the Ge-Sb_2Te_3 and GeSb-$Ge_2Sb_2Te_5$ lines as a function of the Ge content in the composition.

As occurs in GST225 and GeTe, we also show here for Ge-rich GST alloys a connection between the fraction of homopolar Ge-Ge bonds and the fraction of tetrahedra as summarized in Fig. 3.7. Very similar results have been obtained for Ge-rich alloys on the Ge-$GeSb_2Te_4$ tie-line in Ref. [108] (see Fig. 1.24).

Moving to the medium-range order, the ring length distribution computed according to the definition given in Ref. [151] is shown in Fig. 3.8. A ring is the shortest closed loop along bonds connecting neighboring atoms starting from a central atom. Five-membered ring is the most abundant one for all Ge-rich alloys investigated here, as opposed to GST225 for which four-membered rings dominate the distribution [142].

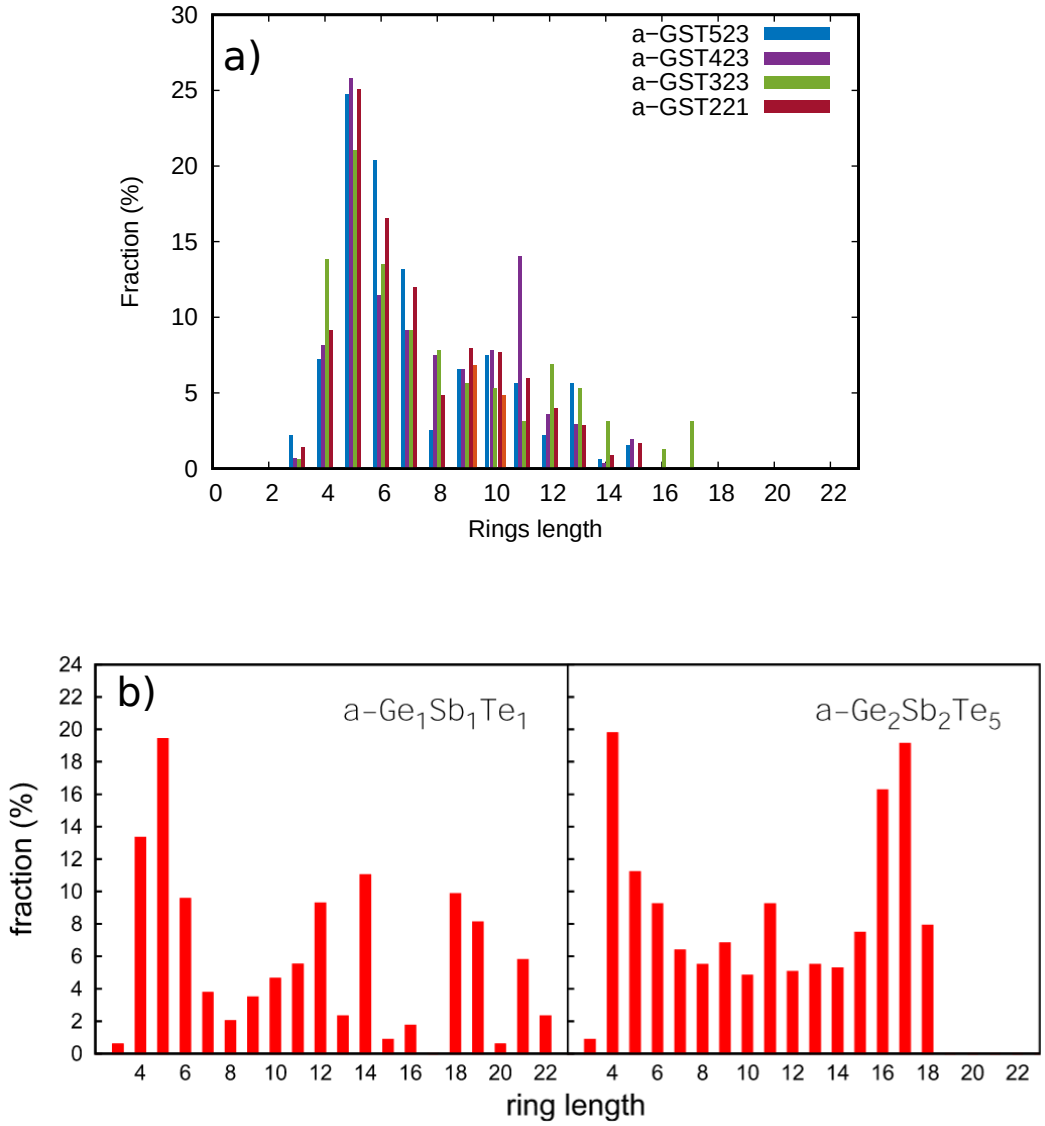

Figure 3.8: Distribution of ring length function of: a) amorphous Ge-rich GST alloys along the Ge-Sb_2Te_3 plus GST221 taken from our previous work [109] and b) Data for amorphous GST225 and GST111 taken from Ref. [142].

3.1.3 Electronic properties

The electronic density of states (DOS) of the amorphous phase of GST523, GST423, GST323 and GST221 are shown in Fig. 3.9.

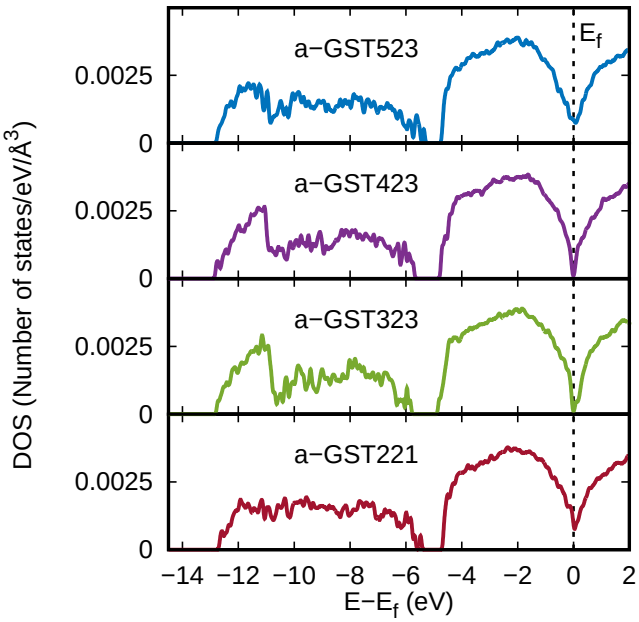

Figure 3.9: Electronic DOS of the amorphous Ge-rich GST alloys along the Ge-Sb_2Te_3 tie-line and of amorphous GST221, computed from KS energies on a 10 × 10 × 10 k-point mesh of the supercell BZ broadened with a Gaussian function 35 meV wide. The highest occupied KS state was taken as a reference (zero of energy). Taken from our previous work [109].

In amorphous GST523 and GST221 there is a finite DOS at the Fermi level while in GST423 and GST323 an energy gap clearly opens up. Nevertheless, states in the pseudogap of GST523 and GST221 are localized as shown by the inverse participation ratio (IPR) superimposed to the electronic DOS in Fig. 3.10. The IPR is a measure of the localization properties and for the i-th KS state is defined by:

$$IPR = \sum_j c_{ij}^4 / (\sum_j c_{ij}^2)^2 \tag{3.3}$$

where j is the index of the gaussian orbitals in the basis set and c_{ij} are the expansion coefficients of the i-th KS. DFT-PBE calculations are known to underestimate the band gap, hence, we can conclude that the amorphous phase of Ge-rich GST alloys might behave as a semiconductor for all compositions studied in this work. For the sake of comparison, we report here in Fig. 3.11 the electronic DOS of the same alloys in the crystalline cubic phase. Further details on the structural properties of the crystalline structure are given in Appendix A. Alloys with less than three p-electron per crystalline site, i.e. GST523, GST423, and GST221 are metallic with the Fermi level lying below the top of the valance band. On the other hand, GST323 with a closed electronic shell

displays a semiconducting behavior with a PBE band gap of 0.16 eV, which is likely to be underestimated. The GST323 alloy keeps the largest band gap among our compositions also in the amorphous phase as shown in Fig. 3.9 and 3.10. The GST323 composition features an average of three p-electrons per site which is the condition for a closed shell system in the metastable cubic phase as demonstrated in Ref. [152].

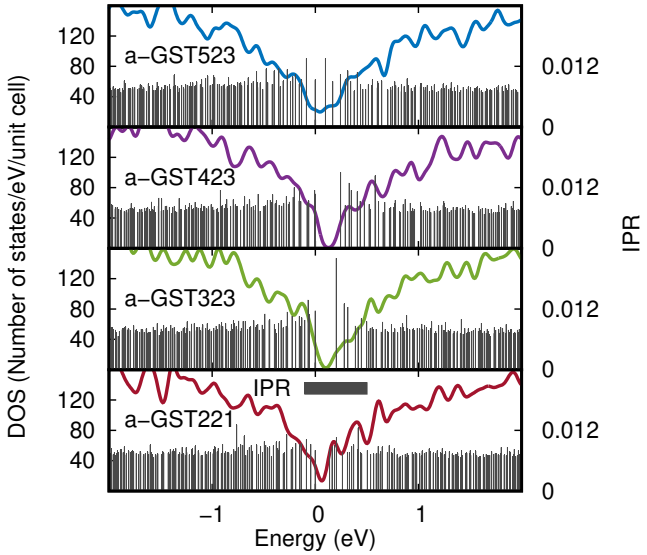

Figure 3.10: Inverse participation ratio (IPR) spikes superimposed to the electronic DOS of Ge-rich amorphous GST alloys near the gap. The zero energy is the highest occupied KS orbital. The states located near the bands edges exhibit more localized behavior than those deeper in the bands. Taken from our previous work [109].

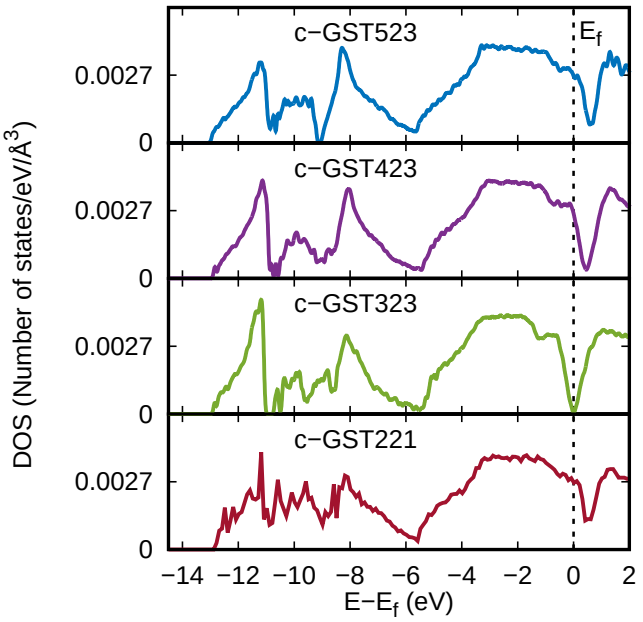

Figure 3.11: Electronic density of states of crystalline cubic Ge-rich alloys. The zero energy is the Fermi level. Taken from our previous work [109].

Experimental data to compare with are not available for the alloys in Fig. 3.9 but ultraviolet photoemission spectra (UPS) have been made available for amorphous GST212, which also lies on the Sb-GeTe isoelectronic line. Therefore, we computed the electronic DOS for amorphous GST212 with 216-atom model generated by the same protocol used for other alloys. The atomic geometry and the volume were optimized at zero temperature and then electronic DOS was computed for the ground state geometry at the supercell Γ-point both with the PBE functional and the HSE06 hybrid functional [153], which is keen to describe better the band gap. KS energies were broadened by a Gaussian function with a variance of 80 meV. The experimental DOS, obtained from UPS measurement compared with the HSE and PBE results in Fig. 3.12. PBE DOS shows a smaller bandwidth with respect to UPS data while the HSE DOS is in a better agreement with UPS data. The hybrid functional seems therefore mandatory for a reliable DOS. However, in the lack of experimental data to compare with, we have not yet extended the HSE calculations to the other compositions. For the sake of comparison, the structural properties of GST212 are reported in Appendix B.

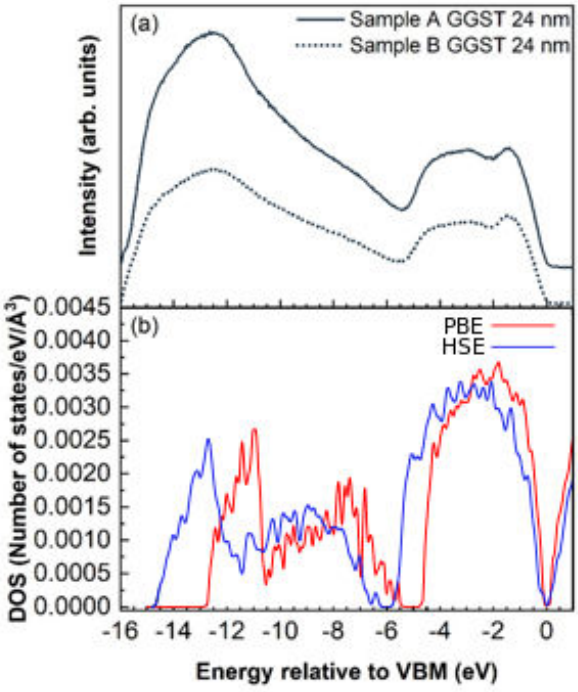

Figure 3.12: Electronic DOS of amorphous GST212: (a) experimental DOS from UPS data on two as-deposited samples [141] (b) theoretical DOS from HSE and PBE calculation. Adapted from our previous work [141].

3.1.4 Vibrational properties

Phonon frequencies of Ge-rich GST alloys were computed at the supercell Γ-point by diagonalizing the dynamical matrix obtained by finite displacements 0.0053 Å large. We also computed the IPR for the phonons which, similarly to the electronic states, measures the phonon localization (see Fig. 3.13). IPR for j-th vibrational mode is given by:

$$\mathrm{IPR} = \frac{\sum_\kappa \left| \frac{\mathbf{e}(j,\kappa)}{\sqrt{M_\kappa}} \right|^4}{\left(\sum_\kappa \frac{|\mathbf{e}(j,\kappa)|^2}{M_\kappa} \right)^2} \tag{3.4}$$

where $\mathbf{e}(j,\kappa)$ are phonon eigenvectors and the sum over κ runs over the N atoms in the unit cell with masses M_κ. According to this definition, the value of IPR varies from $1/N$ for a completely delocalized phonon, to one for a mode completely localized on just one atom.

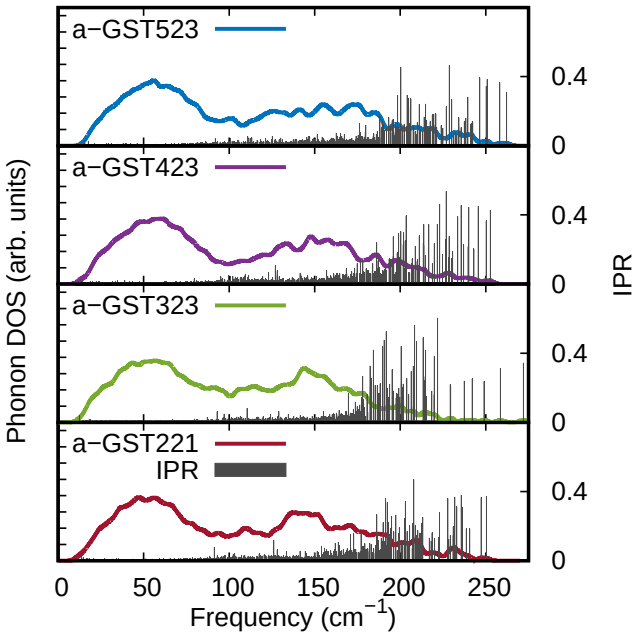

Figure 3.13: Phonon DOS and inverse participation ratio (IPR) of amorphous Ge-rich GST alloys. Taken from our previous work [109].

The phonon DOS projected on different types of atoms and for Ge in tetrahedral geometry are shown in Fig. 3.14. Phonons above 220 cm^{-1} are mainly localized near Ge atoms in a tetrahedral environment; these modes are also the most localized as shown in Fig. 3.13.

With the DFT phonons and the bond polarizability model developed for GST alloys (see Sec. 2.3), we have computed the Raman spectra for Ge-rich GST alloys for future reference. The Raman spectra in backscattering geometry for nonpolarized light of the four alloys are compared in Fig. 3.15.

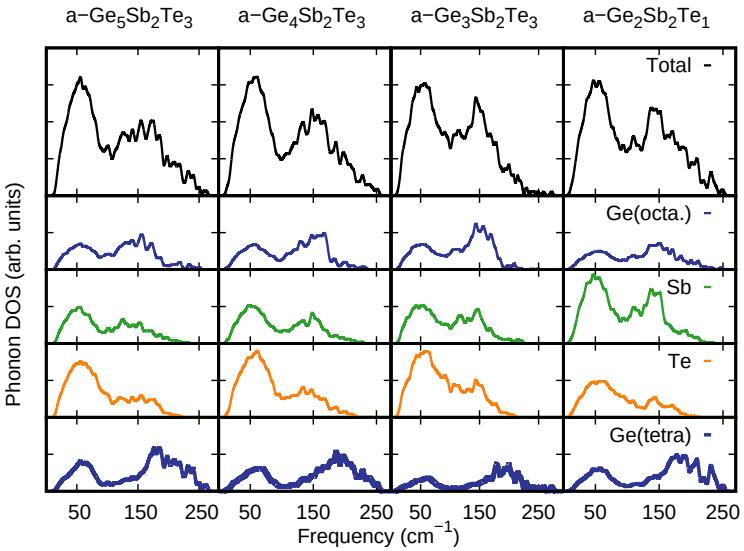

Figure 3.14: The projection of phonon DOS on different types of atoms and for Ge in tetrahedral geometry in the amorphous phase of Ge-rich GST alloys. The DOS is obtained from Γ-point phonon energies broadened by a Gaussian function with a variance of 1.5 cm^{-1}. Taken from our previous work [109].

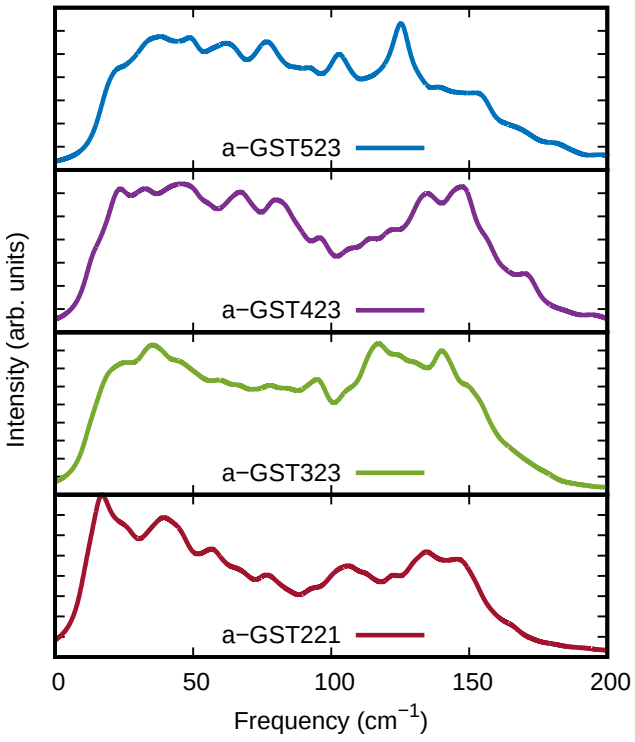

Figure 3.15: Raman spectra of the amorphous phase of Ge-rich GST alloys in nonresonant conditions calculated from DFT phonons and the bond polarizability model in backscattering geometry for non-polarized light. Lorentzian smearing of 3 cm^{-1} was employed to broaden the peaks. Taken from our previous work [109].

Overall the Raman spectra of the Ge-rich GST alloys look sufficiently different for different alloys to allow discriminating the composition by Raman spectroscopy. However, the BPM parameters were obtained in nonresonant conditions while experimental Raman spectra are typically measured in resonant conditions. Hence, the theoretical and experimental intensities might disagree. Besides that, the BPM model was developed for stoichiometric alloys along the GeTe-Sb_2Te_3 tie-line which might limit the transferability of the BPM parameters for strongly Ge-rich alloys.

3.1.5 Summary

In summary, we carried out a DFT study of the structural properties of amorphous Ge-rich GST alloys on the Ge-Sb_2Te_3 and GeSb-GST225 lines of keen interest for storage application in the automotive sector which requires high operating temperatures. These alloys are known to undergo phase segregation upon crystallization which gives rise to a higher T_x. Our analysis shows that the presence of Ge-Ge homopolar bonds and Ge in tetrahedral environments increase by increasing the fraction of Ge in the alloy. These features contribute to enhance the presence of long-membered rings (five and six) at the expense of four-membered ones. As all these features are not present in the crystalline phase, it is expected that Ge-rich GST alloys would display a low nucleation rate, which might translate into higher T_x with respect to GST225 also for a homogeneous crystallization into a metastable off-stoichiometric cubic phase with no segregation of Ge. The same conclusions on the relation between the structural properties of the amorphous phase and the content of Ge in GST alloys have been drawn in a recent DFT study [108] for alloys along the Ge-$GeSb_2Te_4$ tie-line as discussed in Sec. 1.3. This work also shows that when the content of Ge exceeds 50% the amorphous phase turns out to be thermodynamically unstable and might tend to decompose into amorphous Ge and amorphous GST124. The decomposition upon crystallization, however, was not addressed in this study and this is the topic we tackle in the next section.

3.2 Decomposition reactions of non stoichiometric GeSbTe alloys

As anticipated, in a recent work the stability of amorphous GST alloys along the Ge-GST124 tie-line [108] was investigated based on energetic considerations. The results reveal that the amorphous phase of alloys containing more than 50% at of Ge is unstable with respect to the phase separation into amorphous Ge and amorphous GST124. However, the phase separation in PCMs is observed during crystallization in the SET operation. It is unclear whether for Ge content close to or slightly below 50% the amorphous phase could crystallize homogeneously into a cubic crystal with the same compositions, or/and

whether partial segregation of Ge might lead to cubic crystal less rich in Ge but still off the pseudobinary line. To address these questions, we first carried out an exploratory study on some possible decomposition of Ge-rich GST alloys during crystallization [109]. As a first attempt we considered the decomposition pathways of GST523 which is the alloy with 50% of Ge on the Ge-Sb_2Te_3 tie-line studied experimentally in Ref. [13]. We computed the reaction free energy of the process leading to the formation of either trigonal or cubic GST compounds along the GeTe-Sb_2Te_3 tie-line, non-stoichiometric compositions along the Ge-Sb_2Te_3 tie-lines plus other non-stoichiometric alloys, such as GST221, that we also addressed in our study of the amorphous phase. We also considered as possible products of the decomposition reaction of GST523 the two compositions GST213 and GST243 for reasons that we will make clear later on. A schematic representation of the selected decomposition pathways of GST523 is shown in Fig. 3.16 where each reaction was labeled by its main product while the detailed reactions are listed here below:

$$\begin{aligned}
\text{GST523} &\longrightarrow \tfrac{3}{4}\,\text{GST124} + \tfrac{1}{2}\,\text{Sb} + \tfrac{17}{4}\,\text{Ge} && (1)\\
\text{GST523} &\longrightarrow \tfrac{3}{5}\,\text{GST225} + \tfrac{4}{5}\,\text{Sb} + \tfrac{19}{5}\,\text{Ge} && (2)\\
\text{GST523} &\longrightarrow \tfrac{3}{6}\,\text{GST326} + \text{Sb} + \tfrac{7}{2}\,\text{Ge} && (3)\\
\text{GST523} &\longrightarrow 3\,\text{GeTe} + 2\,\text{Sb} + 3\,\text{Ge} && (4)\\
\text{GST523} &\longrightarrow \text{Sb}_2\text{Te}_3 + 5\,\text{Ge} && (5)\\
\text{GST523} &\longrightarrow \text{GST123} + 4\,\text{Ge} && (6)\\
\text{GST523} &\longrightarrow \text{GST223} + 3\,\text{Ge} && (7)\\
\text{GST523} &\longrightarrow \text{GST323} + 2\,\text{Ge} && (8)\\
\text{GST523} &\longrightarrow \text{GST423} + \text{Ge} && (9)\\
\text{GST523} &\longrightarrow \text{GST221} + 2\,\text{GeTe} + \text{Ge} && (10)\\
\text{GST523} &\longrightarrow \text{GST213} + 3\,\text{Ge} + \text{Sb} && (11)\\
\text{GST523} &\longrightarrow \tfrac{1}{2}\,\text{GST243} + \tfrac{3}{2}\,\text{GeTe} + \tfrac{5}{2}\,\text{Ge} && (12)
\end{aligned}$$

More details on the reactions and on the models employed in these calculations are reported in Appendix A. For the calculation of the reaction free energy, we have assumed that non-stoichiometric ternary alloys might exist in the same cubic metastable phase of GST compounds on the pseudobinary line. Although the reactant, GST523, should be in the amorphous phase, we still considered GST523 in the cubic phase as well to estimate the reaction free energy and to identify the most probable decomposition pathway among those we selected. Since the free energy of amorphous GST523 is higher than that of crystalline phase at the same composition, our choice of the cubic phase introduces a constant offset in the calculated reaction free energies. In the decomposition reactions with products on the GeTe-Sb_2Te_3 tie-line, which are the only thermodynamically stable products, the main products were modeled in the trigonal phase while the unary systems were modeled in their standard state. Decomposition pathways with trigonal products along GeTe-Sb_2Te_3 tie-line found out to be the most thermodynamically favored as these are the only stable compounds in the GeSbTe ternary diagram. However, due to kinetics hindrances in the operation of the memory, only the cubic phase could be obtained, as it is the case of GST225. Once we consider the formation of the

cubic phase only, it turns out that other compositions become competitive with those on the pseudobinary line for the crystallization of GST523. This is shown in Fig. 3.17 that collects the reaction free energy of the pathways sketched in Fig. 3.16 and defined previously. Details on the calculations of the reaction free energy will be given later. At this stage, we simply notice that several competitive decomposition channels emerge once the metastable cubic phase is considered as a possible product. These preliminary calculations suggest us to investigate in a systematic way all possible decomposition channels of GST523 from a high-throughput approach that was then extended to study the decomposition of all off-stoichiometric alloys in the central part of the ternary phase diagram.

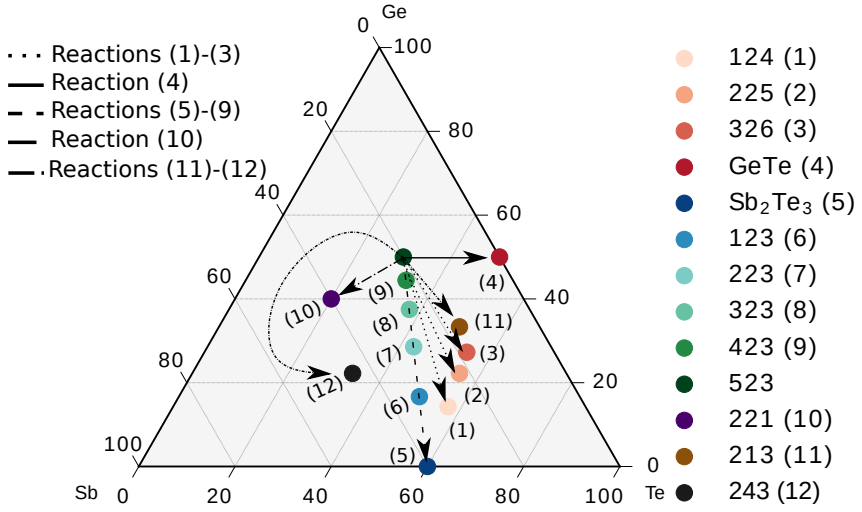

Figure 3.16: Sketch of the selected decomposition pathways of GST523 in the ternary Ge-Sb-Te phase diagram. The arrows indicate the transformations of GST523 into the main product for the different pathways. Adapted from our previous work [109].

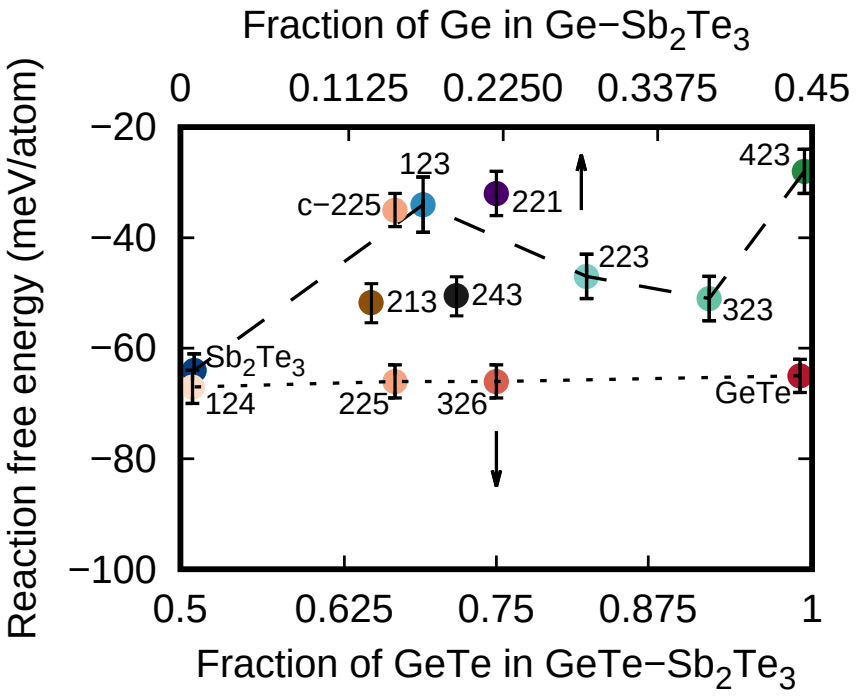

Figure 3.17: Reaction free energy for decomposition pathways of GST523 labeled by their main product. The reaction free energies are reported as a function of the Ge content in the main product on the Ge-Sb_2Te_3 tie-line (upper abscissa scale) and as a function of the GeTe content in the main product on the GeTe-Sb_2Te_3 tie-line (lower abscissa scale). The points for GST221, GST213 and GST243 are also shown although they do not belong to the two tie-lines. c-GST225 stands for the metastable cubic phase of GST225. Sb_2Te_3, GST124, GST225, GST326 and GeTe are in the trigonal phase. Exothermic reactions result in negative free energy. Taken from our previous work [109].

In particular, we computed first the formation free energy of cubic GST alloys in the central region of the ternary phase diagram that then allowed us to build the convex hull, which in turn provides the reaction free energy of any decomposition pathway for a given GST alloy. These data allowed us to compute the reaction free energy for all the possible decomposition pathways of Ge-rich GST alloys into the crystalline less Ge-rich alloys, Ge (and eventually Sb and Te) and the binary compounds. These calculations provide a map for the decomposition paths of any GST composition which in turn allows us to quantify the propensity to decompose of each alloy beside the most probable decomposition products. This approach is exemplified first by the decomposition map of GST523 and then by studying the decomposition pathways of alloys on the Ge-GST124 tie-line.

3.2.1 Computational details

The computational settings employed in this section are very similar to those employed to study the amorphous phase of Ge-rich GST alloys discussed in

Sec. 3.1.1. DFT calculations were performed employing the PBE exchange and correlation functional [115] and the norm-conserving pseudopotentials by Goedeker, Teter and Hutter [118, 119]. The quickstep method as implemented in the CP2k package was exploited [144]. The KS orbitals were expanded in Gaussian-type orbitals of a valence triple-zeta-valence plus polarization basis set and the electronic density was expanded in a basis set of plane waves up to a kinetic energy cutoff of 100 Ry. Dispersion vdW interactions were included by using the semiempirical correction due to Grimme [145].

We modeled all GSTXYZ alloys in the metastable rocksalt geometry for compositions in the central part of the Ge-Sb-Te ternary phase diagram in which a single element (Ge, Sb or Te) in the alloy does not exceed 60 atomic %, as for higher content of Ge we might expect defected tetrahedral geometry while for higher fraction of Sb or Te we might expect to have either, the trigonal layered structures of Sb or more complex structures for very high Te fraction. Considering that we are interested in the possible switching between the amorphous phase and a cubic crystalline phase, as typically occurs in memories, this restriction to the central part of the ternary phase diagram is well justified.

The metastable cubic phase for all GSTXYZ compositions was modeled in 216-atom supercells, the same rocksalt geometry of GST225. As already discussed previously, in cubic GST225, Ge and Sb atoms occupy randomly the cationic sublattice with 20% of stoichiometric vacancies, while the anionic sublattice is fully occupied by Te. Stoichiometric vacancies in GST225 are needed to guarantee a closed shell system. In fact, with 20% vacancies on the cationic sublattice, there are exactly three p electrons per site on average.

In our models, in a GSTXYZ composition with a fraction of Ge larger than 0.5 the cationic sublattice is completely occupied by Ge atoms while the anionic one is occupied by the remaining fraction of Ge, Sb and Te. On the other hand, for compositions rich in Sb, we assumed an amphoteric behavior of Sb and hence Sb atoms were distributed on both the anionic and cationic sublattices. The vacancies were included for alloys with more than three p electrons per site on average to ensure a closed electronic shell. To properly describe the disorder on the different sublattices, we generated three independent SQS models for each composition by using special quasi-random structures (SQS) [154].

To compute the formation free energy of GSTXYZ alloys and construct the convex hull in the Ge-Sb-Te phase diagram we computed also the DFT total energies of the ordered compounds Ge, Te ($P3_121$ space group), Sb ($\bar{R}3m$ space group), GeTe (R3m space group) and Sb_2Te_3 ($\bar{R}m$ space group) modeled with 216-, 192-, 216-, 162- and 270- atom supercells. The atomic positions and cell edges of all models were fully optimized with a convergence threshold of 5

mRy/a_0 for forces and pressure tolerance of 0.01 GPa. The cell optimization of the metastable phases was carried out in two steps. First, we optimized the cell by fixing all angles to 90° and subsequently, we allowed also the cell angles to change. Cell optimizations were performed by restricting the BZ integration to the supercell Γ-point while the total energy of each model was computed with a 3 × 3 × 3 k-point mesh in the supercell BZ. In order to estimate the reaction free energies of the decomposition of GST alloys, we also included the configurational entropy in the crystalline phases due to disorder on both the sublattice given by $S = \frac{-k_B}{2}\Sigma_{i,j}x_{i,j}ln(x_{i,j})$, where j is the index of the sublattice (i.e. cationic and anionic) and i is the index of the atomic species which occupy the j-th sublattice (i.e. Ge, Sb, Te and vacancies), k_B is the Boltzmann constant and $x_{i,j}$ is the molar fraction. The formation free energy of GST alloys, used to compute reactions free energies, includes the total energy at zero temperature and the configurational free energy at 300 K. Calculations on selected possible decomposition pathways have shown that the phononic contribution to the reaction free energy is negligible (a few meV/atom) as shown in Tab. A.2 in Appendix A and it has thus been omitted in this study.

3.2.2 The convex hull in the Ge-Sb-Te ternary phase diagram

As a first step, we computed the formation free energy of GST alloys with respect to the standard phase of the unary systems (Ge, Sb and Te) according to the following chemical reaction:

$$XGe + YSb + ZTe \longrightarrow Ge_XSb_YTe_Z \tag{3.5}$$

The formation free energy for cubic GST alloys in the central part of the phase diagram is shown in Fig. 3.18. Each point on the map corresponds to a GSTXYZ composition for a total number of 698 alloys uniformly spaced, as far as we can with the constraints on the number of atoms in our supercell, within the region explored here. The formation free energy in that map corresponds to the total DFT energy at zero temperature averaged over three independent models for each composition plus the configurational free energy at 300 K due to disorder in the sublattices. A positive value of the formation free energy indicates an alloy unstable with respect to phase separation into the unary systems Ge, Sb and Te. This is the case for Sb-rich alloys on the left part of the phase diagram. From the map in Fig. 3.18 it is clear that the formation free energy is lower (more negative) for alloys along the GeTe-Sb_2Te_3 tie-line and on the Sb-GeTe isoelectronic line. Note that in the formation free energy map all alloys, except GeTe, are in the cubic phase including also Sb_2Te_3. In fact, a metastable cubic phase of this compound was observed experimentally with vacancies on 1/3 of the cationic sites [58].

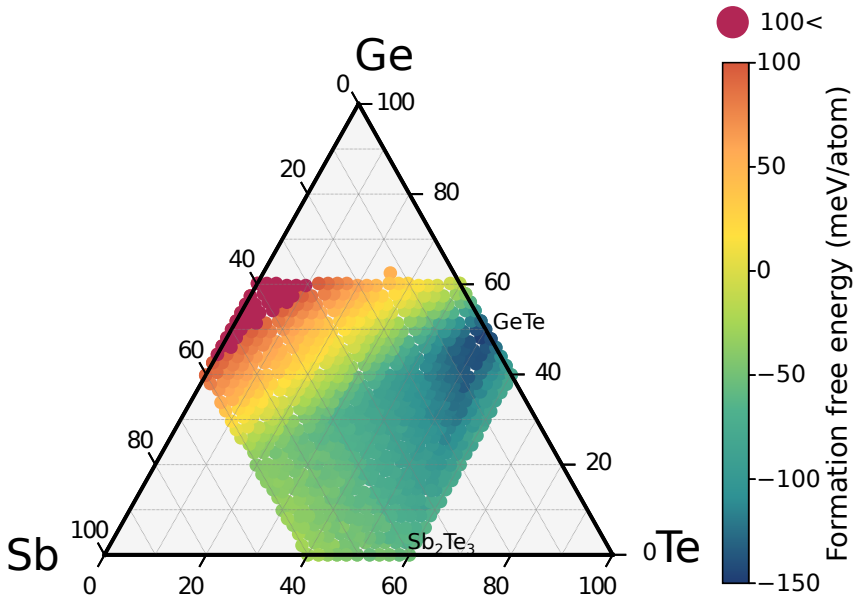

Figure 3.18: Map of the formation free energy of GST alloys in the metastable cubic phase except for GeTe compound which is in the stable trigonal phase. The formation free energy includes the DFT total energy at zero temperature and the configuration free energy contribution due to the disorder at room temperature. Taken from our previous work [155].

The formation free energy of all the thermodynamically stable compounds in a phase diagram form the so-called convex hull, which is a (n-1)-dimensional surface for a phase diagram with n atomic species and it is formed by compounds with a formation free energy lower than that of any other structure or any linear combination of structures with the same composition. The vertices of the convex hull construction, therefore, correspond to the thermodynamically stable compounds while the tie-lines connecting the two compounds are the edges of the convex hull. By construction, the convex hull represents the Gibbs free energy of the alloys in a phase diagram at zero temperature [156, 157, 158].

In the Ge-Sb-Te phase diagram, unary systems, trigonal compounds along the GeTe-Sb_2Te_3 pseudobinary line and the Sb-Sb_2Te_3 tie-line form the so-called convex hull [59, 159, 160, 161] which in this case is a two-dimensional surface. All other structures (in the cubic phase, for instance) have an energy that falls above this set of tie-lines and their distance from the surfaces gives a measure of the degree of the metastability of these structures. We have built the convex hull in the GeSbTe phase diagram to access this information.

In this work, we constructed the convex hull of the Ge-Sb-Te phase diagram considering only unary systems, GeTe and Sb_2Te_3, which is an approximation of the real one. In fact, the energies of the $(GeTe)_m(Sb_2Te_3)_n$ compounds, such as GST147, GST124, GST225, GST326, GST528 and so forth, are very close

to the (GeTe)-(Sb_2Te_3) edge of the convex hull as can be seen in Tab. A.2 in Appendix A. The same holds for the Sb_xTe compounds along the Sb-Sb_2Te_3 tie-line [161]. Thus, for simplicity, we considered a simplified convex hull including only Ge, Sb, Te and the binary GeTe and Sb_2Te_3 trigonal compounds. For the construction of the convex hull, we employed the qhull code [162]. The resulting convex hull with the free energy points of the different cubic alloys is shown in Fig. 3.19. The vertical distance between the formation free energy of an alloy and the underlying surface of the convex hull gives a measure of its metastability and it corresponds to the amount of energy the alloy would gain upon the decomposition into the compounds on the vertices of the surface just below it. In Fig. 3.19 we show the distance from the convex hull for cubic alloys in the central region of the GST phase diagram. Short distance corresponds to a high degree of metastability and hence, probably, long-living states.

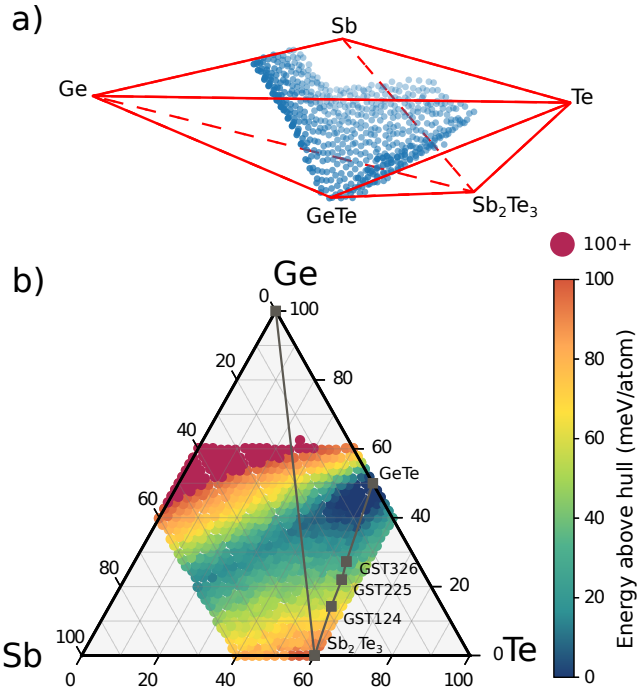

Figure 3.19: a) Convex hull in the Ge-Sb-Te phase diagram. The formation free energy of GST alloys with negative sign are shown in blue points and it is set to zero for standard states. (b) The distance of the formation free energy (meV/atom) of the cubic GST alloys from the convex hull. Short distance corresponds to a high degree of metastability of the composition. Taken from our previous work [155].

.

From the map of the distance from the convex hull, it is clear that alloys on the Sb-GeTe isoelectronic line are remarkably stable since their energy is very close to the convex hull. Indeed, the GST212 alloy on the Sb-GeTe line was indicated as the starting point to obtain a "golden composition" for embedded

memories [10] by increasing the content of Ge. The high metastability (low distance from the convex hull) corresponds to a low propensity to decompose as we will discuss later on. The cubic alloys along the GeTe-Sb_2Te_3 exhibit a large distance from the convex hull, even larger than the distances observed along the isoelectronic line despite the large formation free energy as shown in Fig 3.18. This is actually in agreement with our preliminary results shown in Fig. 3.17 and it can be understood considering the high difference in energy between the trigonal and the cubic phase of these compounds, which is of the order of 50–60 meV/atom [163].

The map of the formation free energy can be used to study all the decomposition pathways of any alloy in the phase diagram. To this end, starting from a GSTXYZ cubic alloy we study the reaction free energy of the decomposition pathways given by:

$$GSTXYZ \rightarrow a\,GSTX'Y'Z' + b\,Sb + c\,Ge + d\,Te + e\,Sb_2Te_3 + f\,GeTe. \quad (3.6)$$

where the GSTX′Y′Z′ alloy and the Sb_2Te_3 compound are in the cubic metastable phase while Ge, Sb, Te and GeTe are in their standard phase. For each reaction of the form given above, the decomposition path is assigned by first maximizing the fraction (a) of the ternary product and then the fraction (e or f) of the binary product. These two constraints uniquely assign the fraction of the unary products. For a given starting composition we can compute the reaction free energy of all the decomposition pathways and plot them in the decomposition map, as it will be exemplified in the next two sections for GST523 and for alloys on the Ge-GST124 tie-line.

3.2.3 Decomposition of GST523

The decomposition map of GST523 is shown in Fig. 3.20. A point in this map corresponds to the value of the reaction free energy to form a GST alloy with the composition of that point starting from GST523. For example, the reaction free energy for the formation of GST423 from GST523 corresponds to the reaction GST523 $\longrightarrow$ GST423 + Ge. Since the alloys are modeled by a 216-atom supercell, the actual reaction is not exactly given by the one reported above but by $Ge_{108}Sb_{44}Te_{64} \longrightarrow Ge_{84}Sb_{42}Te_{63} + GeTe + 23\,Ge + 2\,Sb$, due to the constraints imposed by the finite size of the supercell. This map highlights which decomposition paths are more probable to be observed during the crystallization of the amorphous phase, as the energy of the amorphous phase is always higher than the energy of the cubic phase at the same composition (see Tab. A.2 in the Appendix A).

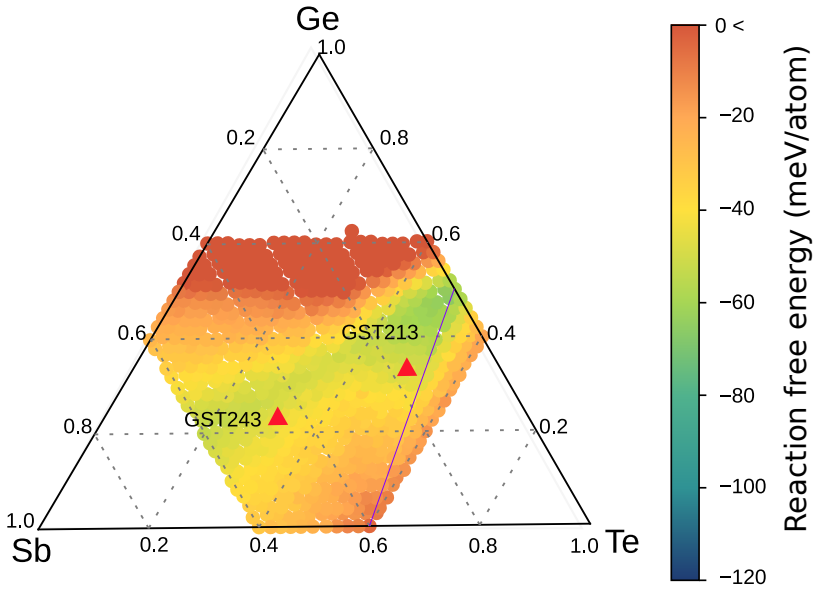

Figure 3.20: Maps of the decomposition pathways of cubic GST523. The color code corresponds to the reaction free energy to form the cubic GST alloy starting for the reactant GST523. The red triangles show the compositions of GST alloys found upon crystallization of melt-quenched and as-deposited amorphous films. Taken from our previous work [164].

Exothermic reactions display negative reaction free energy, the more negative the value of reaction free energy is, the more favored is the corresponding decomposition pathway. The most favored products are found close to the Sb-GeTe isoelectronic line. Selected compositions shown with red triangles in Fig. 3.20 correspond to the alloys seen experimentally upon the crystallization of amorphous GST523 [164] in a joint work that we carried out in collaboration with the experimental partners of the Beforehand project, already mentioned in the introduction. The crystallization of GST523 was studied. In this work, the phase separation of GST523 upon crystallization was investigated experimentally by either water cooling the liquid phase of a bulk sample or by annealing thin amorphous film deposited with pulsed laser deposition technique. EDX elemental chemical mapping (see Fig. 3.21) indicated the formation of multiple crystalline phases, namely, GST213 and GST243, whose reaction free energy was reported previously in Fig. 3.17. Remarkably, these compositions (i.e. GST213 and GST234) lie in the regions with favored reaction free energies exhibiting the most favored decomposition reactions (green region in Fig. 3.20). We remark, however, that the experimental compositions are obtained by averaging over the thickness of the sample which might contain multiple grains of different compositions.

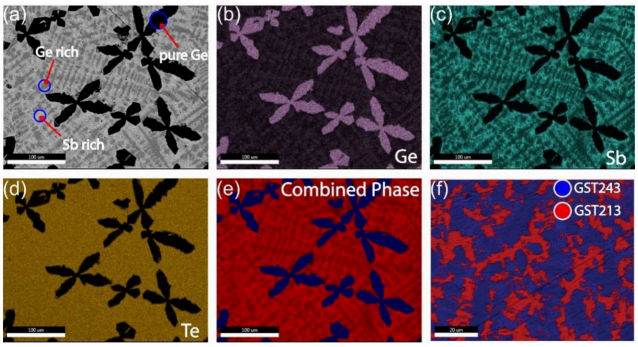

Figure 3.21: SEM–EDX mapping of water-quenched liquid GST523 which results in several crystalline phases. (a) SEM image which shows the formation of Ge dendrites. (b) Ge, (c) Sb, and (d) Te elemental maps. (e) A combined elemental mapping. The color contrast shows the formation of three phases. (f) The elemental map, far from the Ge dendrites, shows the formation of two GST phases, namely GST213 and GST243. Taken from our previous work [164].

3.2.4 Decomposition of Ge-GST124 alloys

The decomposition map shown in the previous section for GST523 can be obtained for any initial composition which allows studying how much Ge segregate by varying the composition. As an example of this methodology, we have computed the decomposition map of the three alloys, GST312, GST412 and GST512, on the Ge-GST124 pseudobinary line (see Fig.3.22) whose amorphous phase were studied by DFT simulations in Ref. [108]. Note that in this latter work, the phase separation of Ge-rich GST alloys into Ge and GST124 was addressed in the amorphous phase. This study suggested that Ge-rich alloys along the Ge-GST124 tie-line with a Ge content less than 50 % at. are stable in the amorphous phase with respect to phase separation. It remains to be seen whether a metastable crystalline cubic phase might form at the same composition. Note that in the decomposition maps of GST312, GST412 and GST512 we plot the reaction free energy only for exothermic decomposition which form an amount of GSTX′Y′Z′ corresponding at least to 1/3 of the reactant (i.e. GSTX′Y′Z′ is the main product).

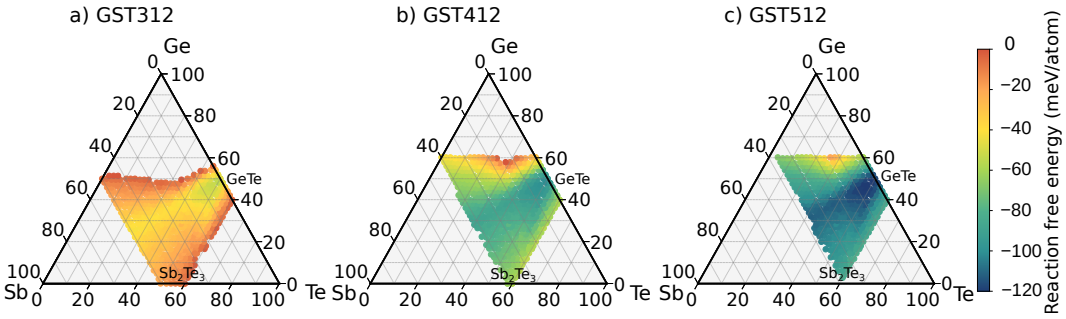

Figure 3.22: Maps of the decomposition pathways of (a) GST312, (b) GST412, and (c) GST512. Taken from our previous work [155].

The maps in Fig. 3.22 clearly show that the energy gain due to phase separation becomes larger and more negative for a wider part of the phase diagram (the products) by increasing the content of Ge in the reactant (compare GST312 with GST512 in Figure 3.22). This result quantifies the expectation that Ge-rich GST alloys are more prone to decompose along several competitive decomposition channels. Note also that the most probable reactions (i.e. most exothermic) correspond to the formation of alloys on the GeTe-Sb_2Te_3 pseudobinary line and on the Ge-Sb_2Te_3 isoelectronic line. Moreover, the energy gain increases remarkably in the region close to GeTe.

Although there is a large number of competitive decomposition channels with very similar reaction free energies, the GSTX′Y′Z′ products of these reactions can hardly be discriminated by X-ray diffraction data. In fact, the equilibrium lattice parameter slightly depends on the composition and it is very similar for the majority of GST alloys in the cubic phase. This is shown in Fig. 3.23 which reports a map of the deviation of the equilibrium theoretical lattice parameter for cubic alloys from that of GST225. Accordingly, the coexistence of different cubic alloys resulting from the crystallization of the amorphous phase of Ge-rich GST alloys is expected during the operation of the memory. The presence of several competitive channels might contributes to the high cell-to-cell variability observed in embedded memories based on Ge-rich GST alloys.

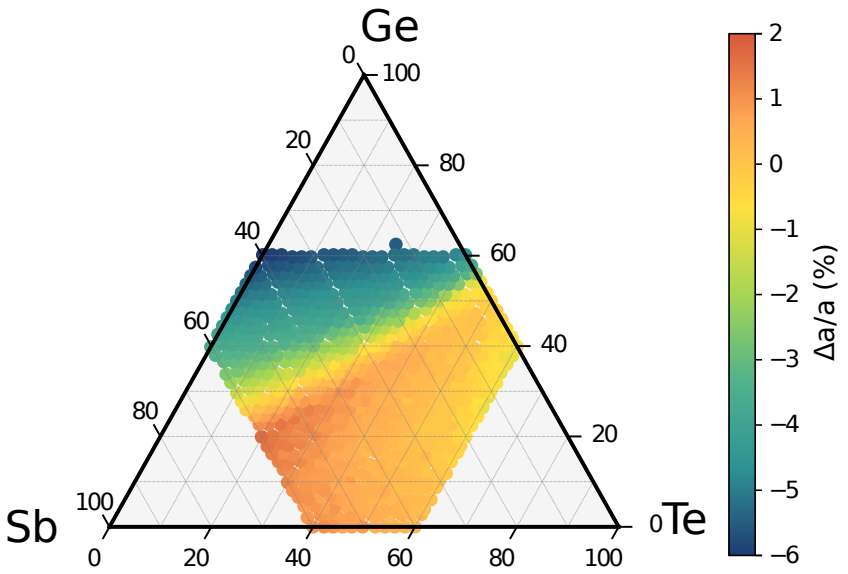

Figure 3.23: The equilibrium lattice parameter of the cubic phase of GST alloys in the ternary phase diagram is reported as the relative difference (a -a_{225})/a_{225} in percentage (%) with respect to the lattice parameter of GST225 (a_{225} = 6.0293 Å) [59]. Taken from our previous work [155].

The maps in Fig. 3.22 show that the number of decomposition channels remarkably increases with the content of Ge which suggests, as one would expect, an increase in the decomposition propensity by increasing Ge. The decomposition map of GST512 displays indeed a largest blue region (more exothermic reactions) among the three alloys on the Ge-GST123 tie-line. In the next section, we try to quantify the decomposition propensity for GST alloys.

3.2.5 Decomposition propensity

We attempted to quantify the decomposition propensity of each GST alloy from its decomposition map. We measured the decomposition propensity by counting the number of exothermic decomposition channels, each weighted by its reaction free energy. In this calculation, we consider the whole decomposition map relaxing the constraint on the fraction of ternary product (one-third to consider it the main product) as we are interested in all the decomposition channels regardless of the nature of the products. For instance, a decomposition reaction which produces GSTX′Y′Z′ in a small fraction can still be strongly exothermic due to the formation of a large fraction of GeTe. This is done for all GST alloys in the central region of the phase diagram and the resulting map of the decomposition propensity is shown in Figure 3.24. Again, the GeTe-Sb_2Te_3 tie-line and Sb-GeTe isoelectronic line exhibit superior stability with other GST alloys as they lay in regions with a low propensity to decompose (blue regions). The map of the decomposition propensity and the results dis-

cussed previously in the Sec. 3.2.5 on the properties of the amorphous phase suggests a possible strategy to minimize the segregation phenomena by still keeping a higher crystallization temperature.

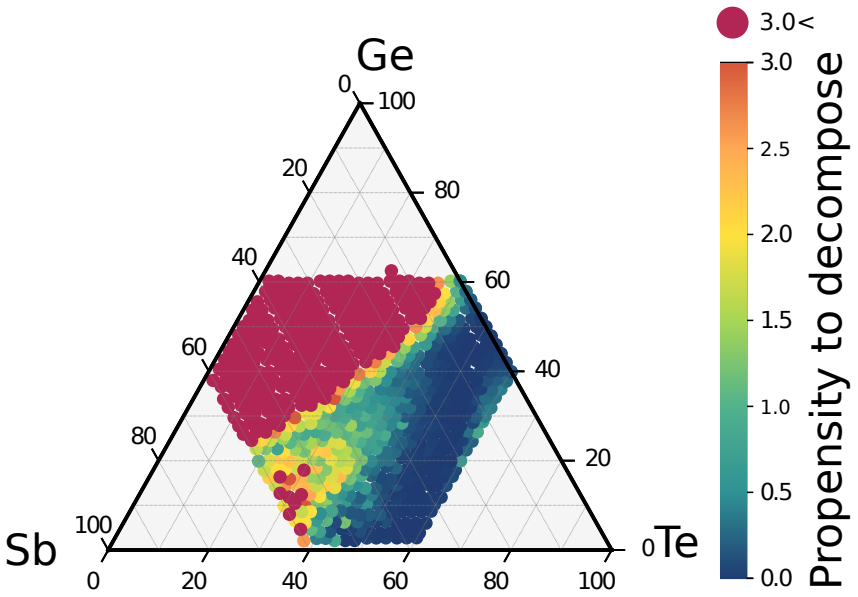

Figure 3.24: Map of the decomposition propensity of the cubic crystalline phase of GST alloys in the ternary phase diagram. Alloys with low propensity lie in the blue regions. The decomposition propensity is computed as the number of exothermic decomposition channels weighted by the modulus of their reaction free energy (in eV/atom). Taken from our previous work [155].

As we already discussed, it is believed that phase separation is the origin of the enhanced crystallization temperature due to the long-scale mass transport involved in the segregation of Ge [165]. On the other hand, a GST alloy with sufficiently high crystallization temperature capable of switching between the crystalline and amorphous phase homogeneously with no phase separation would allow mitigating the drawbacks of the segregation of Ge in Ge-rich alloys. Phase separation is responsible for a large cell-to-cell variability and the presence of several nanocrystallites with different compositions that may undergo coarsening with time could also contribute to the drift of the SET state. Therefore, it is interesting to speculate whether it would be possible to keep a high T_x in a homogeneous crystallization in which a suitably tuned Ge-rich GST alloy could crystallize in a metastable cubic crystal with no segregation of Ge.

The analysis of the structural properties of DFT models of the amorphous phase of GST alloys showed that moving away from the GeTe-Sb_2Te_3 tie-line by increasing either the Ge or Sb content along the Ge-GST124 [108], Sb-GeTe [142] and Ge-Sb_2Te_3 lines, leads to an amorphous network which is more and more dissimilar from the cubic crystal. In fact, the rocksalt phase displays no

homopolar bonds and all atoms are in an octahedral bonding geometry. In the amorphous phase, a fraction of Ge atoms is instead in a tetrahedral geometry favored by the presence of Ge–Ge bonds. Both the fraction of Ge-Ge homopolar bonds and of Ge in tetrahedral geometry increase with the content of Ge. This occurs also by increasing the fraction of Sb due to the lack of Te to form Ge–Te bonds [108, 142].

Another descriptor of the local environment is given by the distribution of ring length. As discussed previously, the ring distribution of amorphous GSTT225 and GeTe exhibits a peak corresponding to the four-membered ring of the form ABAB, where A = Ge/Sb and B = Te, as was shown by DFT MD simulations. This particular ring is the building block of the cubic rocksalt crystal. The four-membered rings are also present in the supercooled liquid phase above glass transition temperature where crystallization takes place [17]. It is believed that the fast crystallization of phase change materials relies on the presence of these rings, which can give rise to a crystalline nucleus by reorientation and merges [17, 21, 166]. Still, by increasing the content of Ge, the fraction of five- and six-membered rings increases at the expense of four-membered ones. Homopolar bonds, tetrahedral geometry and longer rings instead of four-membered ones are all structural features hindering the crystallization since they are not present in the rocksalt structure. Therefore, one might think of controlling the crystal nucleation rate by tuning the composition to enhance the dissimilarity between the crystal and amorphous phases. This would allow improving data retention. In this respect, the propensity map in Fig. 3.24 indicates the regions with a larger Ge or Sb content that can enhance the structural dissimilarity but with a low propensity to decompose during crystallization (mainly near the isoelectronic line). It remains to be seen if this strategy is suitable to raise the crystallization temperature sufficiently for applications in embedded memories and whether a homogeneous crystallization is possible sufficiently far from the GeTe-Sb_2Te_3 tie-line.

The strategy suggested by inspection of the decomposition propensity inspired our experimental colleagues within the Beforehand project in their search for a high T_x alloys with low segregation of Ge. Three different Ge-rich regions in the ternary phase diagram were selected to grow amorphous films by means of molecular beam epitaxy (see Fig. 3.25). Both the effect of the distance between the composition and the GeTe-Sb_2Te_3 pseudobinary line and the effect of changing the composition by keeping fixed the content of Ge [167] were addressed. The resulting compositions are Ge-rich Sb_2Te_3 with a high amount of Ge and Ge-rich GST225 with low and high amount of Ge which have been named H-Ge-ST, L-Ge-GST and H-Ge-GST, respectively, as shown in Fig. 3.25.

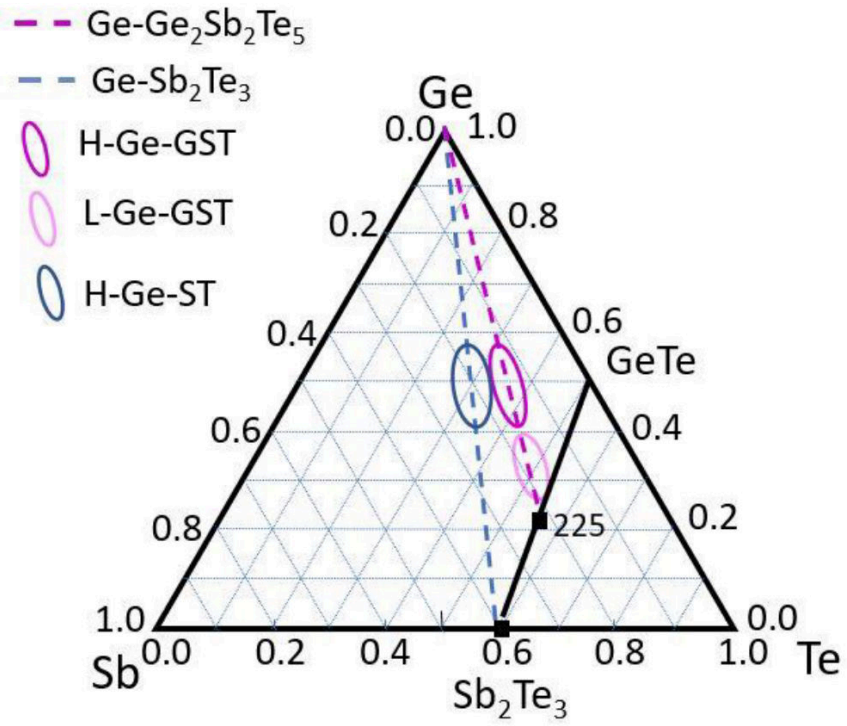

Figure 3.25: Sketch of the composition investigated experimentally in our joint theoretical and experimental work. [167].

XRD data in Fig. 3.26 shows that the H-Ge-ST and H-Ge-GST crystallize with segregation of Ge [167]. On the contrary, the composition L-Ge-GST crystallize with no phase separation. The intensity ratio of the peaks related to GST and Ge is lower in H-Ge-GST than in H-Ge-ST, which suggests a different tendency to decompose in the two alloys in good agreement with our decomposition maps shown in Fig. 3.27.

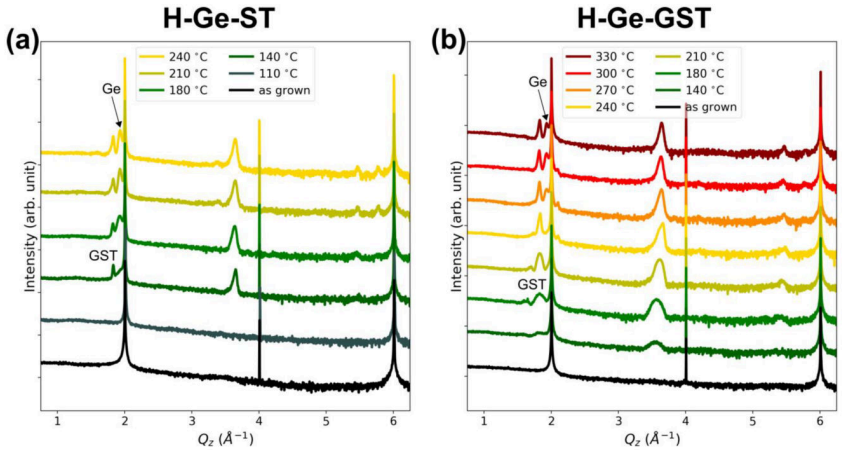

Figure 3.26: XRD data at different temperatures for (a) H-Ge-ST and (b) H-Ge-GST. Taken from our previous work [167].

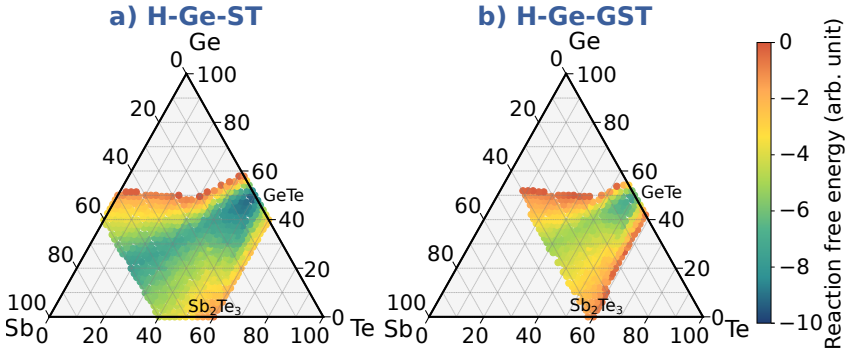

Figure 3.27: The decomposition map of H-Ge-ST (left) and H-Ge-GST (right). Taken from our previous work [167].

Despite the different degree of Ge segregation, T_x is almost the same for H-Ge-GST and H-Ge-ST as shown in Fig. 3.28b, where T_x was assigned by the inflection point in the resistivity-temperature plot in Fig. 3.28.

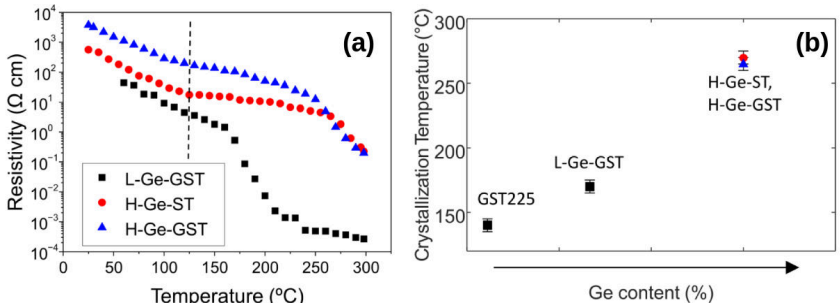

Figure 3.28: a) Electrical resistivity as a function of temperature for three Ge-rich GST alloys. b) Crystallization temperature estimated from the position of the inflection point of the electrical resistivity as a function of temperature for the three different alloys. Taken from our previous work [167].

We have also generated an amorphous model for the H-Ge-GST and H-Ge-ST following the same protocol employed for the other compositions. We found that both display a high fraction of Ge-Ge homopolar bonds, of Ge in tetrahedral geometry and of long-membered rings (see Fig. 3.29) which might contribute to raise T_x besides the segregation of Ge.

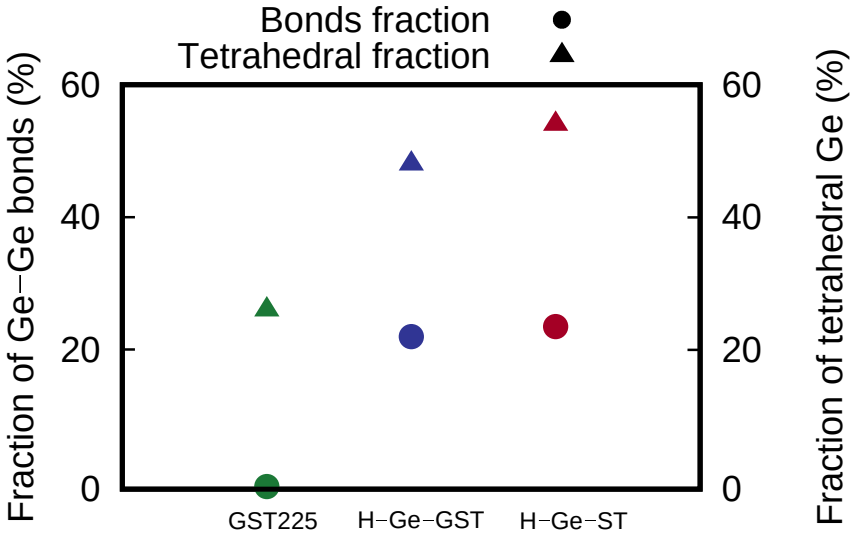

Figure 3.29: The fraction of Ge-Ge homopolar bonds and tetrahedral Ge in H-Ge-ST and H-Ge-GST alloys and, for the sake of comparison, GST225 obtained from DFT-MD simulations.

As a final result, we computed the average fraction of expelled Ge along the decomposition pathways for each GSTXYZ alloy in the central part of the phase diagram. The average fraction is computed by summing the atomic fraction of Ge expelled in each exothermic decomposition path weighted by its reaction free energy as $\Delta Ge_{av}(GSTXYZ) = \frac{\sum_i c_i|\Delta_i|}{X\sum_i|\Delta_i|}$, where the sum runs over the decomposition channels and c_i is the fraction of Ge formed in reaction i (see Equation (3.6)). The resulting map is shown in Fig. 3.30.

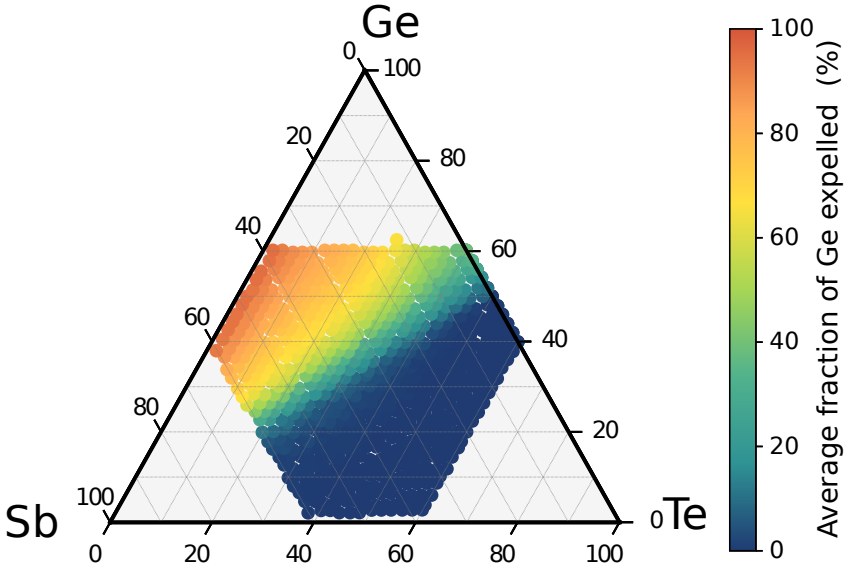

Figure 3.30: Map of the average fraction of Ge expelled (in atomic %) over all the possible exothermic decomposition reactions for GST alloys in the central region of the ternary phase diagram. Taken from our previous work [155].

For the sake of comparison, we also computed the fraction of Ge expelled by considering only the decomposition pathway forming thermodynamically stable compounds at the vertices of the convex hull. In this case, only one decomposition pathway for each GST alloy is possible. This new map of Ge segregation is shown in Fig. 3.31.

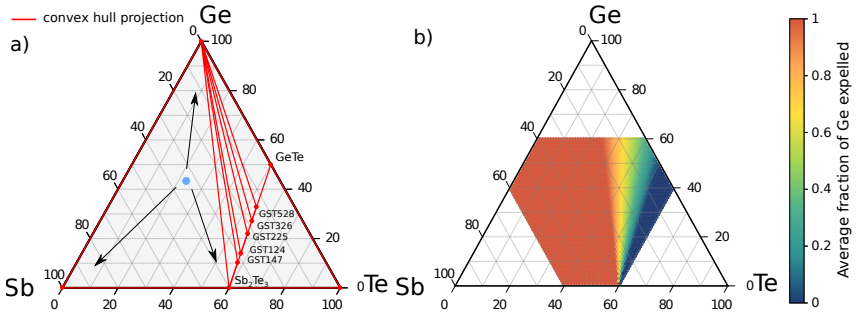

Figure 3.31: a) The projection of the convex hull on the phase diagram showing a decomposition path of generic a GSTXYZ alloy into the stable compounds. b) Map of the fraction of crystalline Ge in atomic formed upon the crystallization into the thermodynamically stable compounds for GST alloys in Ge-Sb-Te phase diagram.

The pictures shown in Fig. 3.30 and Fig. 3.31, not unexpectedly, are very different. By allowing for the formation of metastable cubic phase of off-stoichiometric compositions (see Fig. 3.30), a very low segregation of Ge is expected below the Sb-GeTe isoelectronic line while the segregation increases gradually by increasing the fraction of Ge_xSb_y. The map in Fig. 3.30 and the map of decomposition propensity are actually similar. However, while the decomposition propensity shows a minimum along the Sb-GeTe line, the fraction of segregated Ge in Fig. 3.30 shows a monotonic behavior. By considering only the thermodynamically stable products, a large portion of the phase diagram display full segregation of Ge (i.e. on the left of the Ge-Sb_2Te_3 tie-line) while no Ge segregation is observed only below the GeTe-Sb_2Te_3 tie-line (Fig. 3.31b).

The two maps of the fraction of expelled Ge suggest that measuring the fraction of segregated Ge could be used to identify the phases formed upon decomposition, i.e, the thermodynamically stable compounds on the tie-lines or metastable off-stoichiometric alloys.

3.2.6 Decomposition reactions in the amorphous phase

In the previous section, we discussed the phase separation of Ge-rich GST alloys during crystallization. We already mentioned that phase separation in the amorphous phase was discussed for the Ge-GST124 tie-line in Ref. [108]. Here we consider the phase separation in the amorphous phase for GST523 using the DFT energy of our amorphous models, which allows studying the decomposition of GST523 along the pathways 8, 9 and 10 on page 78 where

the reactant and all the products are in the amorphous phase. The resulting reaction free energies are -15.5, -8.4 and -7.3 meV/atom. For these calculations, the energy of amorphous Ge was obtained from the energy of crystalline Ge and the crystallization energy (120 meV/atom) obtained from calorimetric measurements [168]. Therefore, GST523 is unstable with respect to decomposition into the amorphous GST phases plus amorphous Ge. The same is true if we consider crystalline Ge. The picture remains the same also by considering the vibrational contribution to the reaction free energy at 300 K. Indeed this contribution, despite being negative is still small and amounts to 3.6, 1.9, and 0.4 meV/atom.

It is worth noting that the reverse reaction for the formation of an amorphous phase should occur in the liquid phase. The phase diagram of the binary line Ge-Sb_2Te_3 suggests the formation of the homogeneous liquid with GST523 composition above the liquidus temperature at about 1000 K [169]. If these conditions are reached in the RESET process, the homogeneous liquid might form and segregated Ge could dissolve into the GST liquid giving rise to a more Ge-rich liquid. Then, when the temperature drops abruptly, this homogeneous liquid would quench into metastable amorphous with the composition of GST523. To this end, RESET operation should guarantee the time required to recover a homogeneous system in the liquid phase.

3.2.7 Summary

The study of the decomposition reactions during crystallization suggests that amorphous Ge-rich alloys might decompose along several competitive pathways by forming crystalline alloys in the cubic metastable phase. The coexistence of several grains with different compositions, and possibly different electrical resistance, might contribute to the high cell-to-cell variability observed in embedded PCMs based on Ge-rich GST alloys. Moreover, the resistance drift observed in the SET state in these devices could also be partially due to coarsening of different grains in the nanocomposites formed during the heterogeneous crystallization.

The quantification of decomposition propensity of a given alloy from DFT thermochemical data suggested a possible strategy to reduce the phase segregation, yet keeping a high crystallization temperature.

Hitherto, the decomposition of GST alloys was studied based on thermodynamical considerations only, but kinetics is expected to play a crucial role in determining the actual products. Indeed, the crystallization process may occur in several steps (i.e Ge migration and crystallization both of Ge and GST) and the activation barrier for each step might hinder possible decomposition pathways that could be more prominent in the decomposition map

built from reaction free energy. For instance, decomposition pathways with full segregation of Sb plus other byproducts to form GeTe, although probably thermodynamically favored, might be not viable due to kinetics effects. To this end we carried out a 1 ns long MD simulation at 650 K with the amorphous 216-atom model of GST523; however, neither crystallization nor nucleation was observed on this timescale. Indeed, kinetics effects due to the phase separation require a long scale beyond the reach of DFT methods and therefore they cannot be addressed within the framework used so far. However, machine learning interatomic potentials with a near DFT accuracy might allow large-scale MD simulations that could shed light on the details of the crystallization kinetics in Ge-rich GST alloys.

In this perspective, we have developed a NN potential for GST225, as a first step toward a NN potential for Ge-rich GST alloys as discussed in the next chapter.

Chapter 4

A Neural Network Potential for $Ge_2Sb_2Te_5$

So far, we investigated the phase segregation of Ge-rich GST alloys based exclusively on energetics and thermodynamical considerations. However, a full understanding of the segregation process is far from being reached at this stage because the kinetics of the phase segregation is expected to play a crucial role in making the possible decomposition channels viable. In fact, as discussed in the introduction (see Sec. 1.3), several experiments with different annealing protocols of amorphous films with very similar compositions give rise to a different sequence of crystallization steps with Ge or GST crystallizing first.

The main problem in investigating the kinetics effects at the atomistic level is that the phase separation occurs on a time scale beyond the reach of DFT simulations. However, DFT could be used to develop NN interatomic potentials which display an accuracy similar to DFT at a tiny fraction of the cost. On these premises, we decided to generate a NN interatomic potential for GeSbTe ternary alloys to pave the way for the direct MD simulations of the crystallization process of Ge-rich GST alloys, as it was done for Sb [20] and the GeTe binary compound [19]. As a first step toward the large-scale simulation of Ge-rich GST, we developed a NN potential for the GST225 ternary compound that we exploited to study the kinetics of homogeneous and heterogeneous crystallization. We discuss the development of the NN potential in Sec. 4.1 and its validation in Sec. 4.2 In Sec. 4.3 we discuss its application to the study of the crystallization kinetics of GST225.

We remark that a machine learning interatomic potential for GST225 was recently developed with the Gaussian Process Approximations (GAP) method as reported by Mocanu et al. [170]. The GAP potential features, however, some inaccuracies in reproducing the DFT results on the fraction of homopolar bonds and tetrahedra in the amorphous phase due to the lack of these configurations in the training set [170]. There is therefore room for improvement. We here adopt a different machine learning scheme based on deep NN

as implemented in the code DeepMD and described in Sec. 2.5.3.

4.1 The generation of the neural network potential

The NN potential was obtained by fitting DFT energies, forces and virial tensor of a database containing almost 180000 atomic configurations in the liquid, amorphous, cubic and hexagonal phases of GST225 using DeePMD-kit open-source package [23]. In the database, liquid and amorphous phases were modeled with a 108-atom cubic supercell. The cubic metastable phase was modeled with 57- and 98-atom supercells. The first one corresponds to a 2x2x2 NaCl supercell while the second one corresponds to a 2x2x3 NaCl cell rotated in the XY plane by 45°. Finally, the hexagonal phase was modeled with a 108-atom supercell corresponding to a 2x3x1 supercell rotated in the XY plane in such a way as to form an orthorhombic cell. DFT calculations were performed with the PBE exchange and correlation functional and by employing the norm conserving GTH pseudopotentials [115, 118, 119]. KS orbitals were expanded in Gaussian-type orbitals of a valence triple-zeta-valence plus polarization basis set, while a basis set of plane waves up to a kinetic energy cutoff of 100 Ry is used to represent the charge density as implemented in the CP2k package [144].

To generate the database configurations, long DFT-MD simulations were performed in the BO approximation with a timestep of 2 fs. The BZ integration in MD simulations was restricted to the Γ-point of the supercell. Then, for a subset of the atomic configurations extracted from the MD the energy and the forces were computed by properly integrating the BZ. A 3x3x3 k-point mesh was used for all models but for the cubic phase with 57 atoms, for which we used a 4x4x4 k-point mesh in BZ. These data at convergence in BZ integration were used as a training set for the NN.

For the development of the NN potential, we started with a small database of about 5k configurations generated by DFT-MD. Then, we expanded the database in an iterative process to achieve a refined version of the NN potential. During this iterative process, we added atomic configurations generated from DFT-MD trajectories to enhance the description of specific properties, and also configurations from NN-MD trajectories generated by intermediate versions of the NN potential where energy was poorly described. In the final database, which contains almost 180000 configurations, we covered a wide range of thermodynamical conditions, i.e., different temperatures up to 2000 K and several densities in the range between 0.026 and 0.036 atoms/Å^3. More details about the configurations in the database are given in Tab. 4.1. In Tab. 4.1 supercooled liquid simulations refer to simulations of several tens of ps at fixed temperature in the range 500-900 K, quenching simulations refer to simulations in which the system was cooled very rapidly from 990 to 300

K while metadynamics simulations refer to biased simulations to enhance the sampling in a specific configurational region.

Table 4.1: Details of the dataset used for the training of the NN potential.

Phase/simulations	Number of configurations
Liquid phase	4489
Supercooled liquid simulations	64440
Quenching simulations	70463
Amorphous phase	3620
Cubic phase	8764
Hexagonal phase	7935
Metadynamics simulations	18524

In the construction of the NN potential, we employed two descriptors: the two-body embedding descriptor and the three-body embedding one (see Sec. 2.5.2). For the two-body descriptor, we use $r_c = 7$ Å which includes the third coordination shell and $r_{cs} = 3.8$ Å (see Eq 2.33). Moreover, we set the maximum number of neighbors to 30, 30 and 40 for Ge, Sb and Te. The embedding network has 3 hidden layers with 20, 40 and 80 neurons respectively while the M_2 parameter is set to 35 (see Sec. 2.5.2). Instead, for the three-body embedding descriptor, we choose a shorter cutoff r_c= 3.8 Å, which includes only the first coordination shell and a smoothing cutoff r_{cs}= 3.0 Å. The maximum number of neighbors is 10 for all the chemical species and the embedding network has 3 hidden layers with 3, 6 and 12 neurons. Finally, the fitting network for the energy consists of 4 hidden layers with 120, 60, 30 and 15 neurons with atomic energy reference for the chemical species of -102.297, -146.521 and -218.984 eV for Ge, Sb and Te. These reference energies were obtained from isolated atoms calculations with CP2k. In the embedding and fitting network, we have used the hyperbolic tangent as an activation function. We have also exploited the residual connections as discussed in sec 2.5.1. The hyperparameters which control the learning process are reported in table 4.2.

Table 4.2: Details of the hyperparameters used for the learning rate and the Loss Function (LF) employed for the training of the NN potential.

Learning rate	initial value = 0.001	final value = 3.51e-8
Decay of the learning rate	prefactor = 0.95	steps = 7275
Energy prefactor in the LF	initial value = 1	final value = 1000
Forces prefactor in the LF	initial value = 8000	final value = 800
Virial prefactor in the LF	initial value = 0.2	final value = 100
Batch size (configurations)	training = 16	test = 128
Training epochs	200	

The energy root-mean-square error (RMSE) between the value predicted with the NN potential and that of DFT is 8.4 and 8.6 meV/atom for the

training and test sets. The RMSE on forces is 159 meV/Å for both sets. The distribution of NN errors on energies and forces is in Fig. 4.1. The typical average errors obtained with DeePMD for disordered systems like ours (i.e liquid and/or amorphous phases) is in the range 2-7 meV/atom and 60-130 meV/Å [139, 171, 172].

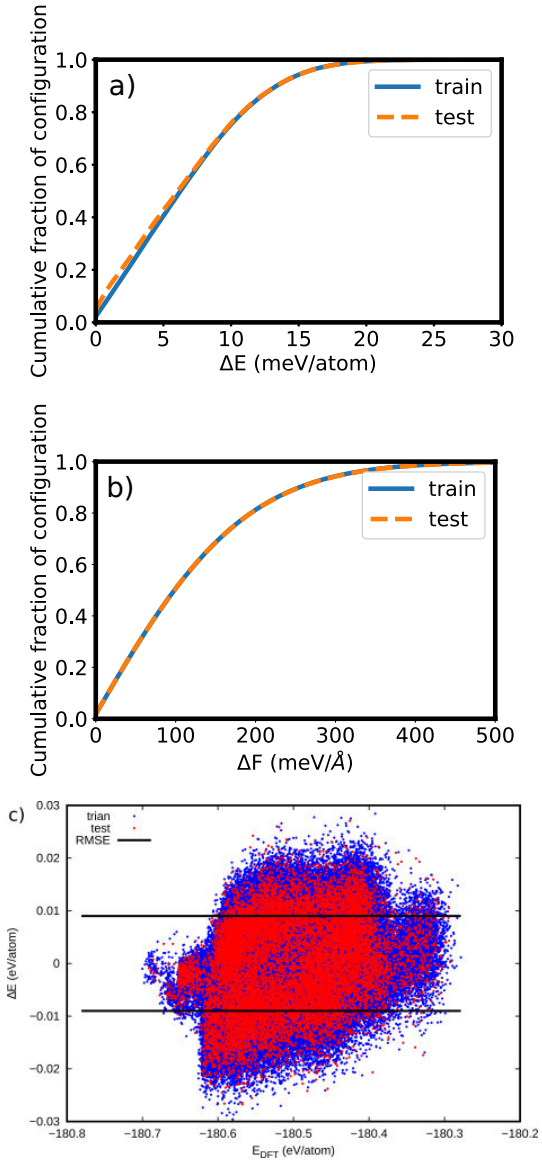

Figure 4.1: Cumulative fraction of the absolute errors of the NN potential in training and test data sets for a) the energies per atom ($\Delta E=|E_{DFT}-E_{NN}|$) and b) forces ($\Delta F=|F_{DFT}-F_{NN}|$). c) We report the distribution of the absolute error as a function of DFT energy.

All the NN-MD simulations were performed with the LAMMPS code [173] exploiting GPU acceleration with a timestep of 2 fs and a Nose-Hoover thermostat.

4.2 Validation of the NN potential

The NN potential has been validated on the properties of the liquid, amorphous, cubic and hexagonal phases as described in the separate sections below.

4.2.1 The liquid phase

The structural properties of the liquid phase of GST225 have been evaluated from NN-MD simulation with a 999-atom supercell at 990 K and compared with those obtained from DFT-MD simulation with a 216-atom supercell at the same temperature. In both models, we used the experimental density of the amorphous phase, 0.031 atoms/Å^3 [143], which is close to that of the liquid of 0.0307 at 883 K [147]. To generate the liquid models we first performed a 7 ps long MD simulation at 2000 K to properly randomize the atoms in the box. Then, we performed a second equilibration at 990 K for 10 ps. Finally, we evaluated the structural properties over trajectories 10 ps long. The total and partial pair correlation functions are compared in Fig. 4.2 while in Tab. 4.2.1 we report the position of the first maximum and minimum of each partial correlation function. We remark, however, that the first minimum is often not very well defined.

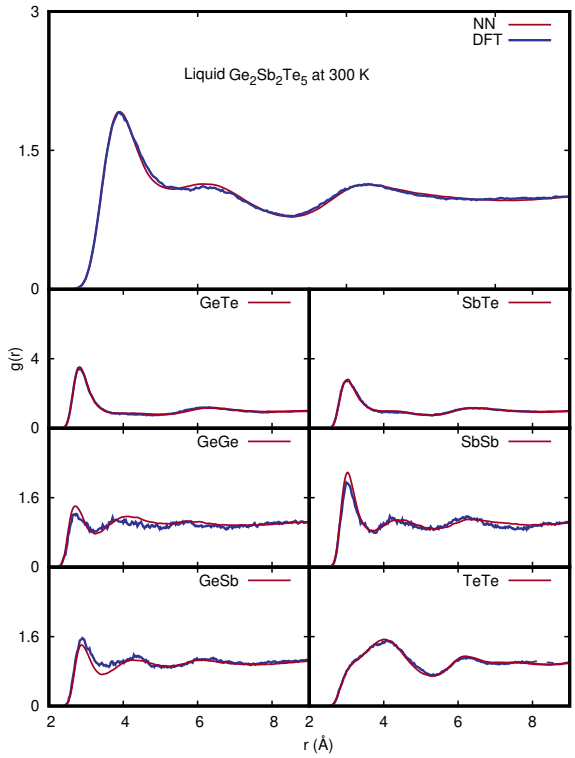

Figure 4.2: Total and partial radial distribution function of GST225 in the liquid phase at 990 K. DFT (blue curves) and NN (red curves) data refer to a 216-atom or 999-atom models.

Table 4.3: First maximum and minimum of the pair correlation functions in the liquid phase of GST225 at 990 K from DFT-MD simulations. The NN data are given in parentheses.

Bond type	First maximum(Å)	First minimum (Å)
GeGe	2.70 (2.71)	3.24 (3.28)
GeSb	2.88 (2.9)	3.6 (3.44)
GeTe	2.80 (2.82)	-
SbSb	3.00 (3.00)	3.78 (3.70)
SbTe	3.04 (3.05)	-
TeTe	-	-

In Figs. 4.3 and 4.4 we report the angular distribution function resolved and the distribution of coordination number for each chemical species computed by integrating the partial pair correlation functions up to a bonding cutoff, which corresponds to 3.2 Å for all pairs except for Sb-Te, for which we use 3.4 Å as was done in Ref. [70].

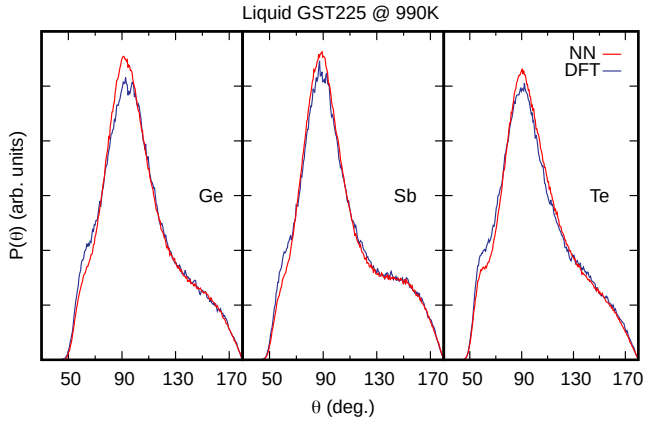

Figure 4.3: Angular distribution function resolved per central atomic species in liquid GST225 at 990 K. The data were normalized to the number of triplets in each model to properly compare the 216-atom and 999-atom results of DFT and NN simulations.

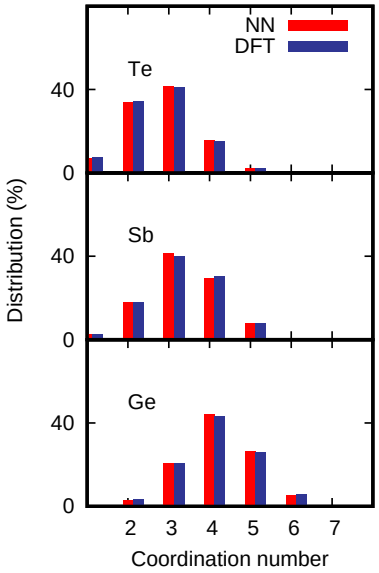

Figure 4.4: Distribution of coordination numbers resolved per chemical species in the liquid phase of GST225 at 990 K from NN and DFT simulations.

The structural properties obtained from NN-MD simulations are in excellent agreement with those obtained from DFT-MD, which suggests that the NN potential reliably describes the liquid phase.

We have also computed the self-diffusion coefficients from NN-MD simulations for several temperatures in the range 1200-800 K above T_m and below T_m in the supercooled liquid. The density was fixed to the value of the experimental amorphous phase (0.031 atoms/Å^3) as it was done in the previous DFT-PBE work [174] that we use as a reference for the validation. We first equilibrated the liquid for 40 ps at several temperatures in the canonical ensemble starting from the liquid at 990 K. Then, at each temperature, we performed a further equilibration for 20 ps in the microcanonical ensemble. Finally, the mean square displacement (MSD) and then self-diffusion coefficients at long time, MSD=6Dt, were computed over 40 ps trajectories. Then we have fitted self-diffusion coefficients with the Arrhenius function $D=D_0 e^{\frac{-E_a}{k_b T}}$ (see Fig. 4.5). The resulting activation energy E_a^{NN} is 0.267 eV and D_0=1.03x10^{-7} m^2/s. We repeated these simulations by including the semiempirical correction due to Grimme [175] (D2) which provides a very similar activation energy E_a^{NN+D2} = 0.286 eV and D_0=1.01x10^{-7} m^2/s. These values are similar to other values reported in the literature as shown in Tab. 4.2.1. Note that in the fitting procedure, we did not include the data below 700 K which does not fall in the Arrhenius plot due to the known fragility of the system.

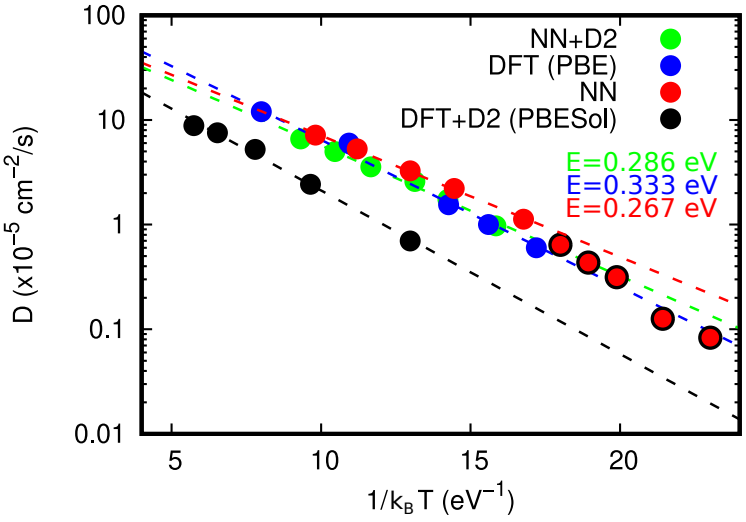

Figure 4.5: The Arrhenius plot of the diffusion coefficient as a function of temperature. The extracted activation energies for diffusion are E_a^{DFT}=0.333 eV from PBE calculations [174] and 0.25 eV from PBESol calculations [176], E_a^{NN}=0.267 eV for NN simulations, and E_a^{NN+D2}=0.286 eV for NN+D2 simulations. The data of D below 700 K are shown with a black border and they have been excluded from the Arrhenius fit.

Table 4.4: Activation energy for the atomic self-diffusion in liquid GST225 in literature.

E_a (eV)	D_0 (m^2/s)	density (atom/Å^3)	method	Reference
0.333	-	0.031	PBE	[174]
0.300	-	-	PBESol	[176]
0.285	0.01	0.031	NN+D2	This work
0.267	1.03	0.031	NN	This work
0.260	0.45	0.031	PBESol	[177]

At lower temperature we observe deviations from the Arrhenius law as it is expected for a fragile liquid. Then, we tried to fit the self-diffusion coefficient of the supercooled liquid in a wider range of temperatures with the formula due to Cohen-Grest (CG)[178] which is more suitable for fragile liquids:

$$\log(D(T)) = A - \frac{B}{T - T_0 + [(T - T_0)^2 + 4CT]^{1/2}} \tag{4.1}$$

where A, B, C and T_0 are fitting parameters in K. Actually, this formula was used in Fig. 1.16 to fit the kinetic prefactor u_{kin}= $\frac{6D}{\lambda}$ in the crystal growth velocity inferred from DSC data [89]. We have fitted the diffusion coefficient of the supercooled liquid phase as shown in Fig. 4.6 and the resulting parameters are A=-2.44, B=630.30 K, C=21.09 K and T_0=317.67 K to be compared with the values obtained from calorimetric measurements B=121 K, C=1.71 K and T_0= 427 K [89]. We notice that our fitting parameters for D

differ significantly from those obtained experimentally from the fitting of the crystal growth velocity.

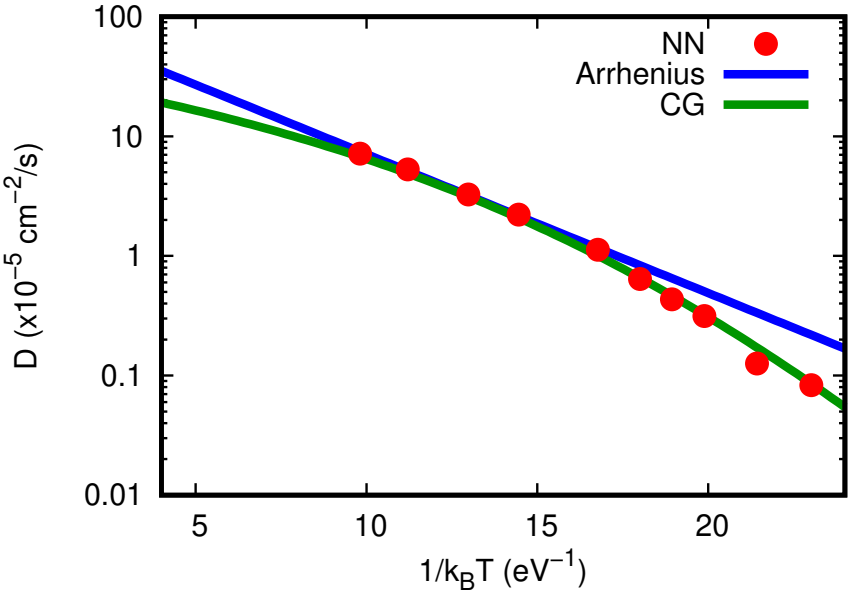

Figure 4.6: Cohen-Grest fit of the self-diffusion coefficient as a function of temperature (green curve) compared with the Arrhenius fit (blue curve) (see Fig. 4.5).

So far, the ability of the NN potential to describe the structural properties of the liquid phase is in good agreement with our PBE calculations and data present in the literature. As a further step in the benchmark of the NN potential, we estimated the melting temperature of the crystalline cubic phase of GST255 by means of the phase coexistence approach [179]. To this aim, we have prepared a 12960-atom model of the cubic-liquid interface initially set at 900 K with cell edges of 6.15x6.15x11.08 nm, which corresponds to the equilibrium density of the cubic phase at 300 K. The interface lies on the XY plane and the thickness of the slab in the cubic phase is almost 2 nm while the liquid slab is almost 9 nm. Then we carried out several independent simulations at different temperatures in the range 880-950 K. A snapshot of the initial configuration is reported in Fig. 4.7 on the left. At temperatures above T_m we expect that the crystalline region in our model melts, as it is the case for 950 and 940 K (see the left side of Fig. 4.7) while for temperatures below T_m, we expect that the crystalline region grows, as it is the case for the trajectories below 920 K. This set of simulations suggests that the melting point of the NN potential is in the range 920-930 K which is very close the experimental value of 900 K. All these simulations were carried out at the equilibrium density of the cubic phase at zero Kelvin and in the canonical ensemble. A better estimation of T_m should, however, be obtained from NPT simulations to describe the density change across melting and the thermal expansion of the crystal. NPT simulations with the PBE functional are, however, problematic as they

underestimate significantly the equilibrium density due to the coalescence of nanovoids. Therefore, in order to better estimate T_m we have repeated the same calculations in the temperature range 925-940 K in NPT ensemble with NN+D2, as the D2 contribution prevents the coalescence of nanovoids that form by decreasing the density as it was also reported for GeTe [180]. Starting from the same initial configuration, we first carried NPT-MD simulation allowing the cell edges to change at fixed angles. The equilibrium density is reached on a time scale of 30 ps, much shorter than that required for crystallization. Then, we performed long NPT simulations which yielded T_m of 940 K, which is close to the previous NVT results with the PBE function and no vdW interactions (see Fig. 4.8). At this temperature, the latent heat of melting (ΔH_m) is around -180 meV/atom which is slightly higher than the values reported in literature obtained from calorimetric measurements (-120 and -173 meV/atom [181, 182]). To calculate the latent heat, we carried a 40 ps long NPT simulation starting from a properly equilibrated 999- (900-) atom cubic supercell at 940 K for the liquid (crystalline) phase to estimate the equilibrium density. The initial configuration for the liquid phase is a snapshot of the liquid model at 990 K discussed above while that of the cubic metastable phase is a SQS model in 5x5x5 supercell in the rocksalt geometry. Then, a 40 ns long NVT-MD simulation at the densities obtained from the previous simulations was performed to estimate the enthalpy of each phase. Note that all these calculations were carried out by including the D2 correction. Finally, in order to assess the error on the latent heat introduced in case one does not take into account the volume density change upon melting (i.e. NVT simulations), we computed the enthalpy of the liquid phase at the equilibrium density of the cubic crystalline phase at 940 K. The resulting heat of melting is ΔH_m = -220 meV/atom which is higher than the result obtained from NPT simulations, as one might expect considering that the liquid phase is compressed. The value of ΔH_m computed in the same manner without vdW interactions is instead 230 meV/atom which we expect to be affected by a similar 40 meV/atom error due to the use of NVT conditions. Finally, we estimated an uncertainty of about 10 K in T_m due to the constraint at constant volume with the Clausius-Clapeyron equation.

As a final result, in Fig. 4.9 we show the enthalpy as a function of temperature computed in the supercooled phase. This data was obtained from independent NN+D2 simulations with 999-atoms supercell at several temperatures, where the models were initially equilibrated at 1000 K and then cooled down to the target temperature in 20-100 ps. The enthalpy displays clearly two slopes as a function of temperature which allows us to estimate the glass transition temperature in the range 450-500 K, very similar to the experimental value of 473 K [183]. This is apparent from Fig. 4.10 which shows the specific heat (C_v) as a function of temperature computed from the derivative of enthalpy, which in return was fitted by a quadratic function separately in the two regions below and above T_g. The jump of the C_v occurs at the glass tran-

sition temperature. The decrease of C_v with temperature in the supercooled liquid above T_g is a typical feature of fragile liquids [184].

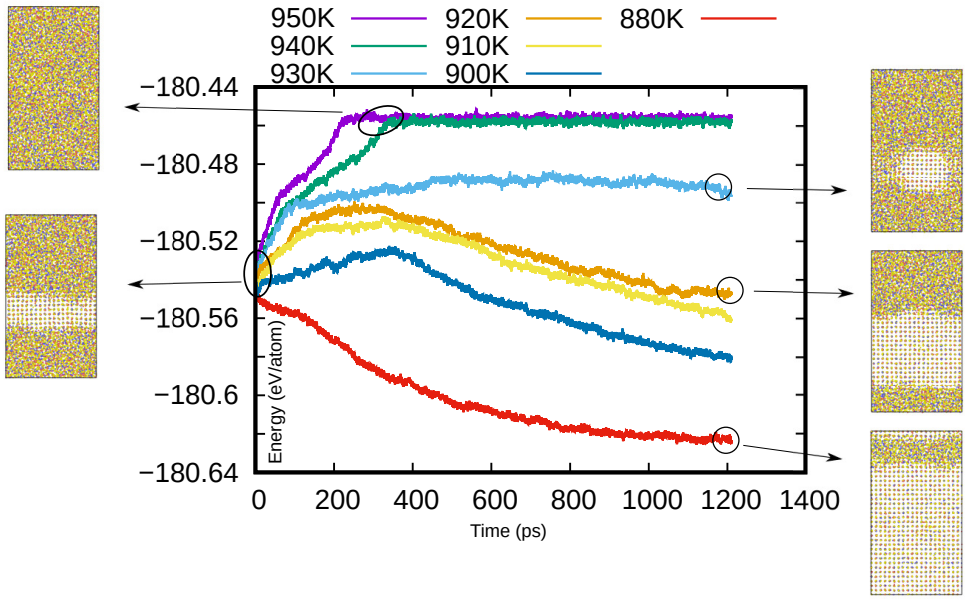

Figure 4.7: The internal energy as a function of time at different temperatures of the cubic-liquid interface model. Several snapshots along these trajectories are reported to show the initial configuration and the movement of the interface between the two phases. The melting temperature is estimated to be in the range 920-930 K. The data refer to NN simulations with no vdW interactions.

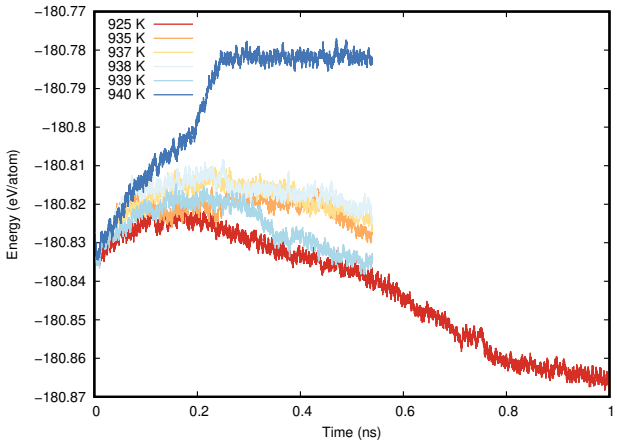

Figure 4.8: The internal energy as a function of time at different temperatures of the cubic-liquid interface model from NN+D2 simulations. The melting temperature is estimated to be around 940 K.

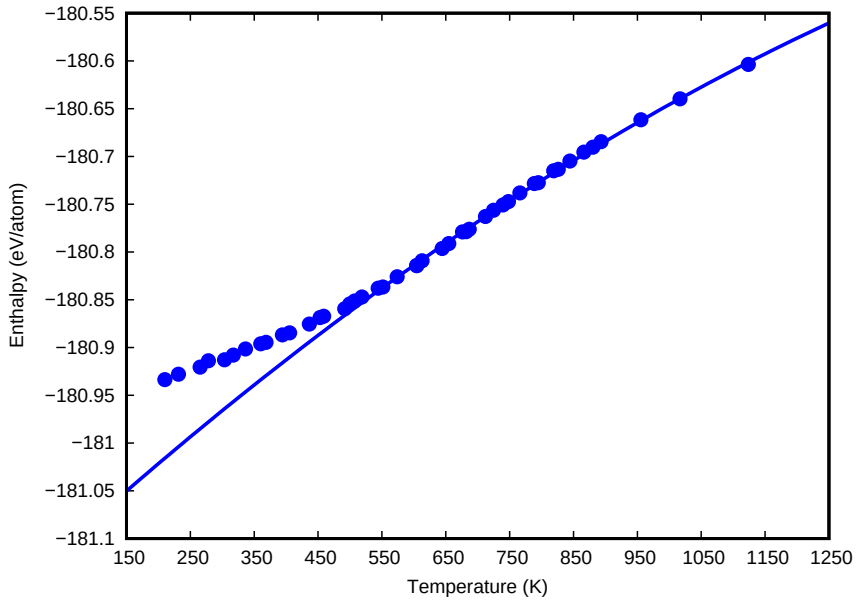

Figure 4.9: Enthalpy of the supercooled liquid as a function of temperature computed with NN+D2. The continuous blue line is a quadratic fit above T_g.

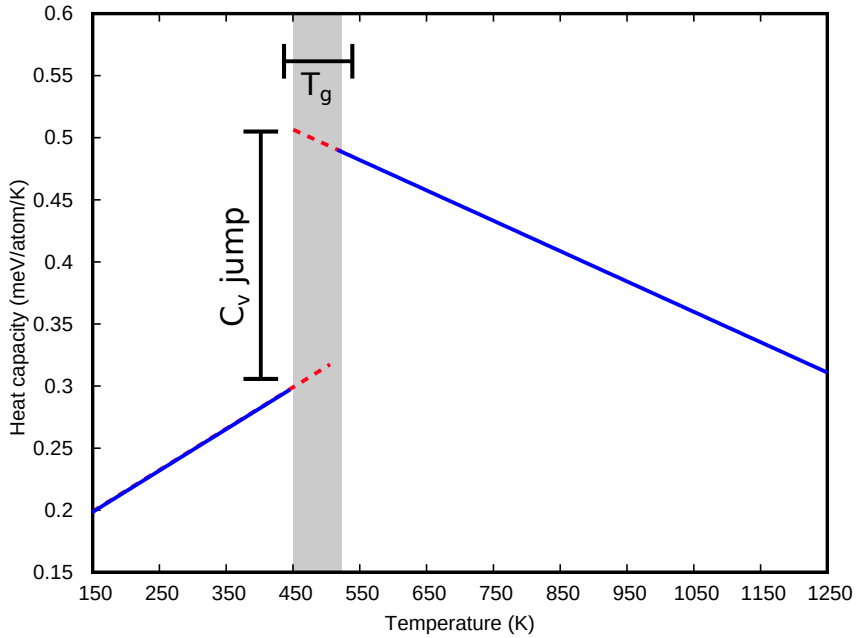

Figure 4.10: Heat capacity at constant volume of the supercooled liquid as a function of temperature obtained from the enthalpy fit above and below T_g (see Fig. 4.9).

4.2.2 The amorphous phase

The NN potential was further validated on the structural properties of the amorphous phase. A 999-atom model of amorphous GST225 at the experimental density of the amorphous phase (0.031 atom/Å^3) was generated by

quenching from the melt in 100 ps. Four DFT simulations at the same density were generated with the same quenching protocol as above.

Total and partial pair correlation functions of DFT and NN models are compared in Fig. 4.11. The position of the first maximum and minimum of each partial correlation function are shown in Tab. 4.2.2. It is worth highlighting that the Ge-Ge homopolar bond in the four DFT models generated for this benchmark is slightly longer (2.66±0.05 Å) than that reported in Ref. [70] (2.62 Å) while it is shorter than that reported in Ref. [69] (2.84 Å). Overall, the pair correlation functions obtained from NN-MD are within the spread of DFT results over all four models except for GeGe and GeSb for which the first peak is overestimated.

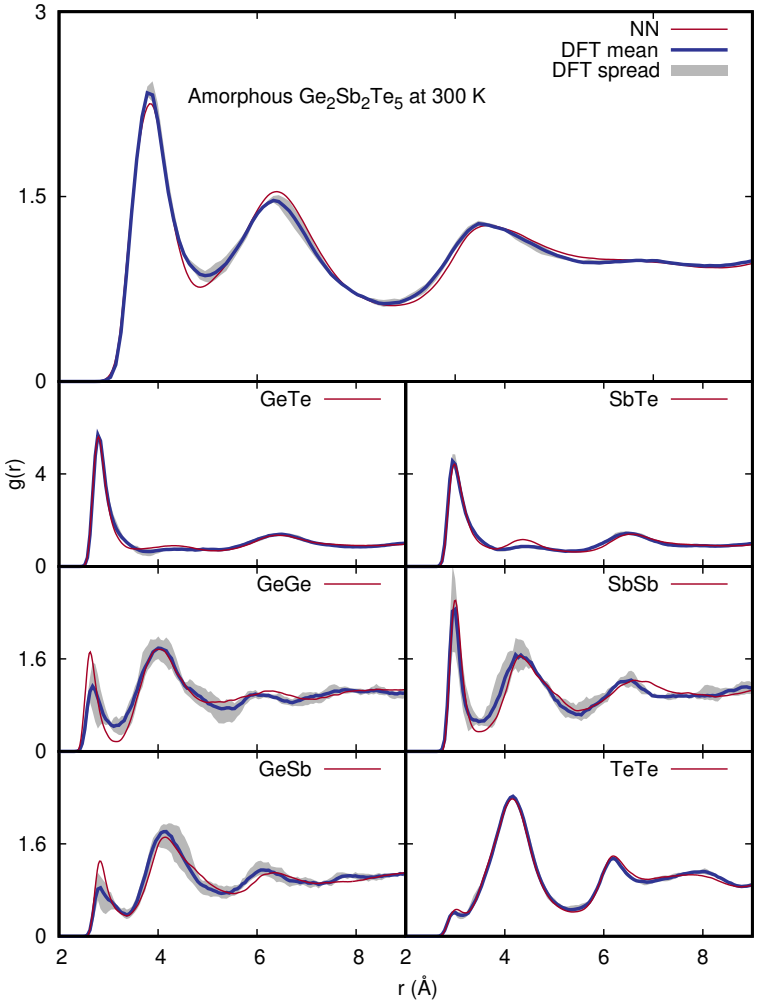

Figure 4.11: Total and partial radial distribution function of amorphous GST225 at 300 K. DFT data (blue curves) are obtained as the average over four independent 216-atom models while NN data (red curves) are obtained from a 999-atom model.

Bond type	First maximum(Å)	First minimum (Å)
GeGe	2.66 (2.62)	3.15(3.14)
GeSb	2.83 (2.82)	3.6 (3.6)
GeTe	2.78 (2.78)	-
SbSb	2.99 (2.99)	-
SbTe	2.97 (2.96)	-
TeTe	2.99 (3.04)	-

Table 4.5: Position (Å) of the first maximum and minimum of the pair correlation functions in the amorphous phase of GST225 at 990 K from DFT and NN MD simulations. NN data are given in parenthesis.

The angular distribution functions for each chemical species of the NN and DFT models are compared in Fig. 4.12 while the distribution of the coordination number is compared in Fig. 4.13, as obtained by integrating the pair correlation functions up to a bonding cutoff corresponding to 3.2 Å for all pairs except for Sb-Te, for which a longer cutoff value of 3.4 Å was used. The average coordination numbers for each pair of atoms are reported in Tab. 4.6.

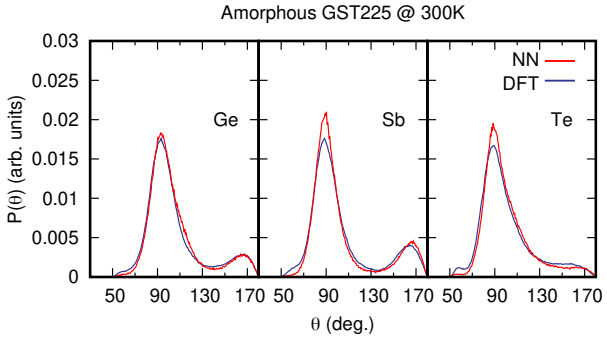

Figure 4.12: Angular distribution function resolved per central atomic species in amorphous GST225 at 300 K. The data are normalized to the number of triplets in each model to properly compare the 216-atom DFT model to the 999-atom NN one.

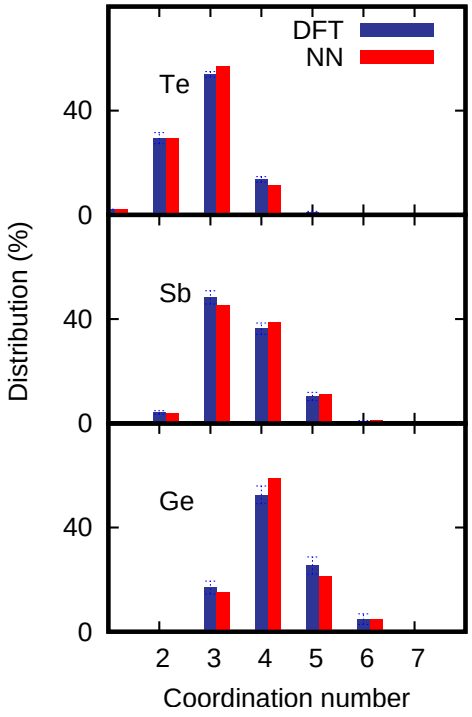

Figure 4.13: Distribution of coordination numbers resolved per chemical species in the amorphous phase of GST225 at 300 K from NN and DFT simulations.

Table 4.6: Average coordination numbers for different pairs of atoms computed from the partial pair correlation function in amorphous GST225 generated from DFT and NN simulations. NN data are given in parentheses.

-	Total	With Ge	With Sb	With Te
Ge	4.17 (4.15)	0.34 (0.35)	0.26 (0.33)	3.57 (3.46)
Sb	3.54 (3.60)	0.26 (0.33)	0.51 (0.54)	2.77 (2.72)
Te	2.82 (2.79)	1.42 (1.37)	1.10 (1.09)	0.28 (0.31)

The distribution of the local order parameter q for tetrahedricity (see Sec. 3.1) is reported in Fig. 4.14 for four-coordinated Ge atoms. The bimodal shape corresponds to tetrahedral and defective octahedral geometries. We quantified the fraction of Ge atoms in a tetrahedral environment by integrating the q parameter between 0.8 and 1 as discussed in Sec. 3.1. In the NN model, 33% of Ge atoms are in the tetrahedral geometry while in our DFT models only about 23% of Ge atoms are associated with this geometry. DFT calculations in literature report a fraction of tetrahedral Ge in the range 27-35% [16, 174].

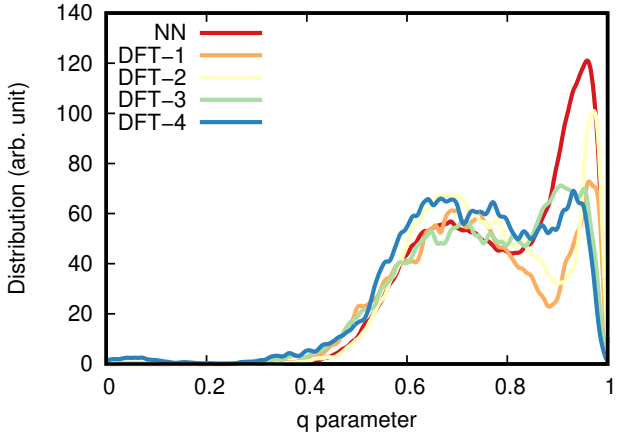

Figure 4.14: Distribution of the local order parameter q for four-coordinated Ge in amorphous GST225 for the NN model and for each of our four DFT models.

In Appendix C, we report a similar comparison between the structural properties of amorphous GST225 where DFT data shown here, and DFT data of amorphous GST225 obtained with the same protocol used so far by including the d-electrons of Ge.

Finally, we computed the phonons density of states in amorphous GST225. To this end, we computed the phonon frequencies at the Γ-point of the supercell by diagonalizing the dynamical matrix constructed numerically by atomic finite displacements as discussed in sec 3.1.1. In Fig. 4.15 we report the result for a 216-atom model computed both with DFT and NN and a 999-atom model computed with NN.

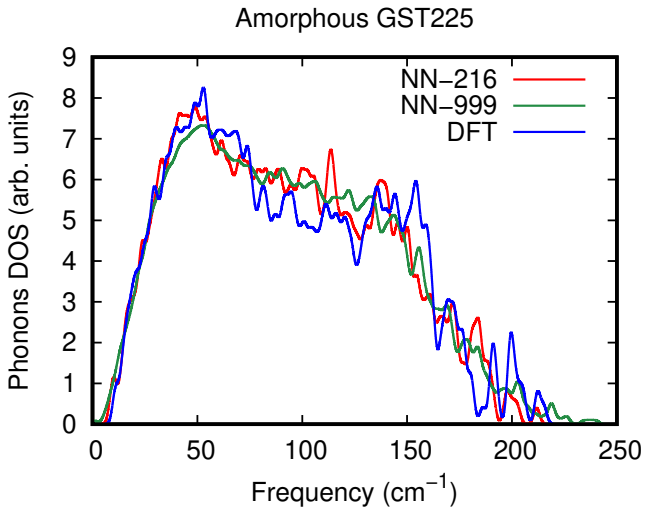

Figure 4.15: Phonon density of states of the amorphous phase. The phonons were computed at the Γ-point of a 216- and 999-atom supercell with the NN and a 216-atom supercell with DFT. The dynamical matrix was computed by finite atomic displacements 0.0053 Å large for DFT and 0.03 Å for NN.

4.2.3 The cubic crystalline phase

The metastable cubic phase of GST225 consists of a NaCl structure with the anionic sublattice occupied by Te and the cationic one occupied by Ge, Sb and 20% of vacancies. In this benchmark, the cubic phase was modeled by employing a 300-sites supercell (the same as in Ref [70]) with 30 vacancies and 270 atoms at the stoichiometric GST225 composition. A comparison of the Birch–Murnaghan equation of state from DFT and NN is shown in Fig.4.16 and the corresponding fitting parameters are reported in Tab. 4.7. Moreover, in Fig. 4.17 we report DFT and NN phonon DOS computed with the same protocol used for the amorphous phase.

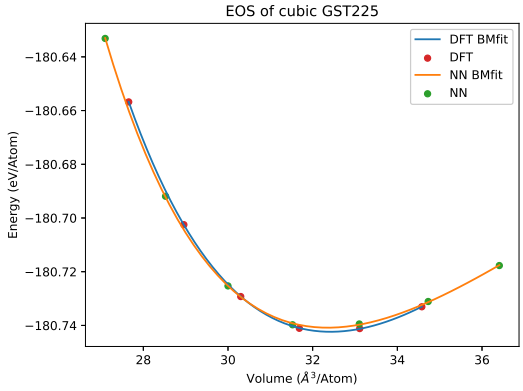

Figure 4.16: Equation of state of the cubic phase of GST225 from DFT and NN calculations.

Table 4.7: Fitting parameters of the Birch–Murnaghan equation of state of cubic GST225.

Method	E_0 (eV/atom)	V_0 (Å^3 /atom)	B (GPa)	B′
DFT	-180.7424	32.42	25.10	7.53
NN	-180.7408	32.35	22.51	9.41

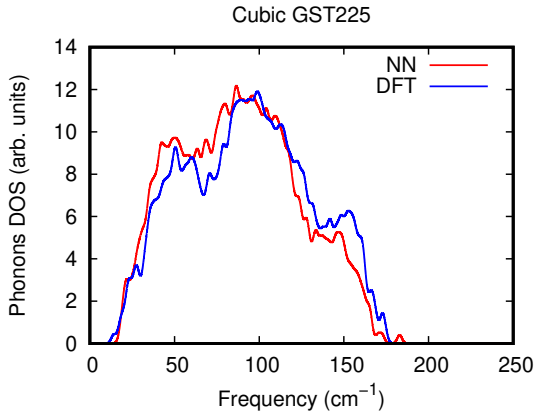

Figure 4.17: DFT and NN phonon density of states of the cubic phase of GST225. The phonons were computed at the $\Gamma-$point of a 270 atoms supercell. The dynamical matrix was computed by finite atomic displacements 0.0053 Å large for DFT and 0.03 Å large for NN.

4.2.4 The hexagonal phase

The hexagonal phase is the stable phase of GST225 at normal conditions and it corresponds to a distorted NaCl structure with an elongation along the [111] direction. The primitive unit cell contains 9 atoms stacked along the c direction with a stacking order ABCABC (see Fig. 4.18). Each formula unit forms a lamella separated from the others by a so-called vdW gap, although the interlamella interaction is not just a vdW contact but a metavalent bond as discussed in Ref. [78] and Sec. 1.2. There are three different distribution of atoms proposed from experimental data as discussed in Sec. 1.2. In this section, we refer always to the Kooi stacking. The Birch–Murnaghan equation of state (EOS) from DFT and NN are compared in Fig.4.19 and the corresponding fitting parameters are reported in Tab. 4.2.4.

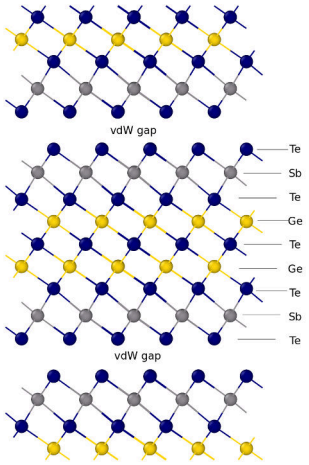

Figure 4.18: Kooi stacking of the hexagonal phase of GST225.

We have also calculated the phonon DOS and dispersion curves. Note that within the PBE approximation, GST225 in the hexagonal phase features phonon instability [185] which is also present in NN calculations as it should be. These instabilities at the PBE level are resolved by including the semiempirical correction due to Grimme (D2) [185]. Hence we calculated the phonon dispersion relations by including the D2 correction which are compared with previous DFT+D2 results [185] in Fig. 4.20. The code Phonopy [186] was used to compute phonons dispersion relation from the Γ-point dynamical matrix of a 12x12x4 supercell.

The derivatives of the dispersion curves close to the Γ-point provide the sound velocities that we averaged over all directions in the BZ to yield a transverse velocity of v_t= 1270 m/s and a longitudinal velocity of v_l = 2888 m/s. The DFT-D2 values are v_t= 1950 m/s and v_l = 3120 m/s [185]. From these values, we can also estimate the bulk thermal conductivity using the Cahill formula [187] for the minimum thermal conductivity given by:

$$k_{min} = \frac{1}{2}\left(\frac{\pi\rho^2}{6}\right)^{\frac{1}{3}}(v_l + 2v_t)\,k_B \tag{4.2}$$

where ρ is the atomic density and k_B is the Boltzmann constant. Within this approximation, our minimum thermal conductivity is estimated to be 0.3 W/m/K (0.43 from DFT+D2 data in Ref. [185]).

Table 4.8: Fitting parameters of the Birch–Murnaghan equation of state of hexagonal GST225.

Method	E_0 (eV/atom)	V_0 (Å^3 /atom)	B (GPa)	B′
DFT	-180.7883	31.131	19.8	21.75
NN	-180.7890	32.135	18.7	23.38

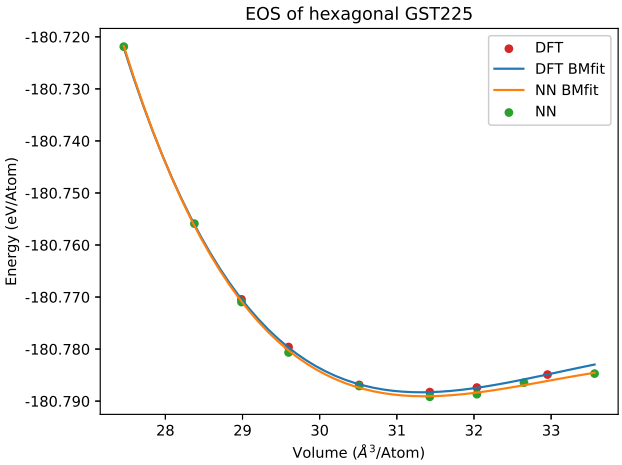

Figure 4.19: Equation of state of the hexagonal phase of GST225.

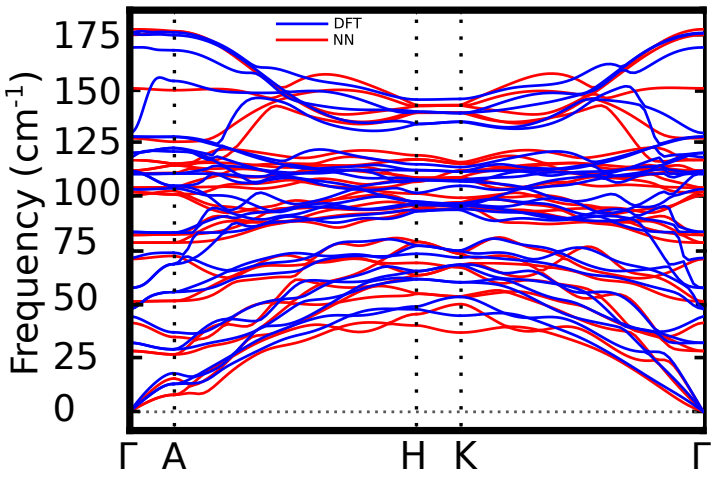

Figure 4.20: NN and DFT phonon dispersion relations of GST225. DFT data are taken from Ref. [185].

In summary, although the RMSE for the energies and forces are not very small (8 meV/atom and 160 meV/Å), albeit similar to other NN potentials in literature for disordered materials, the validation of the potential over the properties of liquid, amorphous and crystalline phases are good. A less satisfactory agreement is found for the phonon dispersion relation in the crystalline phase which are, however, relatively difficult to be reproduced by a NN potential not explicitly devised for these properties. Overall, we judge that our potential is sufficiently accurate to address the study of many properties of this system including the crystallization kinetics, which is the subject of the next section.

4.3 Simulation of the crystallization process

As a first application of the NN potential for GST225, we studied the kinetics of the crystallization process in the supercooled liquid phase by evaluating the crystal growth velocity (v_g) as a function of temperature in the range 500-940 K. This information can be extracted from the simulations already performed to estimate T_m with a model displaying a liquid-crystal interface. To this end, these simulations have been extended to the wider range of temperatures studied here. For each starting temperature, the model has been quenched in 40-80 ps from 900 K. The number of crystalline atoms is measured by using the local order parameter for crystallinity Q_4 order parameter [188] (see Appendix D) that is suitable to distinguish atoms in crystalline or liquid/amorphous environments. Then the evolution of the crystalline interface was monitored to evaluate v_g as given by:

$$v_g = \frac{dL(t)}{dt} \Rightarrow L\,(t) = \left(\frac{N(t)}{2A\rho_{NN}^{cubic}}\right) \tag{4.3}$$

where $L(t)$ is the thickness of the crystalline slab, $N(t)$ is the number of atoms in the crystalline slab, ρ_{NN}^{cubic} is the theoretical equilibrium density of the cubic phase and A is the cross-section of the box orthogonal to the growth direction. The evolution of $L(t)$ as a function of time at several temperatures is reported in Fig. 4.21.

The crystal growth velocity as a function of temperature can be described by the phenomenological Wilson–Frenkel equation (WF) $v_g = u_{kin}(1 - e^{-\frac{\Delta\mu}{k_B T}})$ (as discussed in Sec. 1.2.1) where u_{kin} is a kinetic prefactor and $\Delta\mu$ is the free energy difference between the crystalline and supercooled liquid phases. For the kinetic prefactor we use the approximation $u_{kin} = \frac{4D}{\lambda}$, the same one used to study the crystallization of GeTe with the NN potential in Ref. [19, 22] where λ is the typical jump distance of atoms in the elementary diffusion process. We fitted the values of D in Fig 4.5 to be plugged in WF formula with the CG expression (see Eq. 4.1) which better describes the diffusion coefficient for fragile liquid down to temperatures close to T_g.

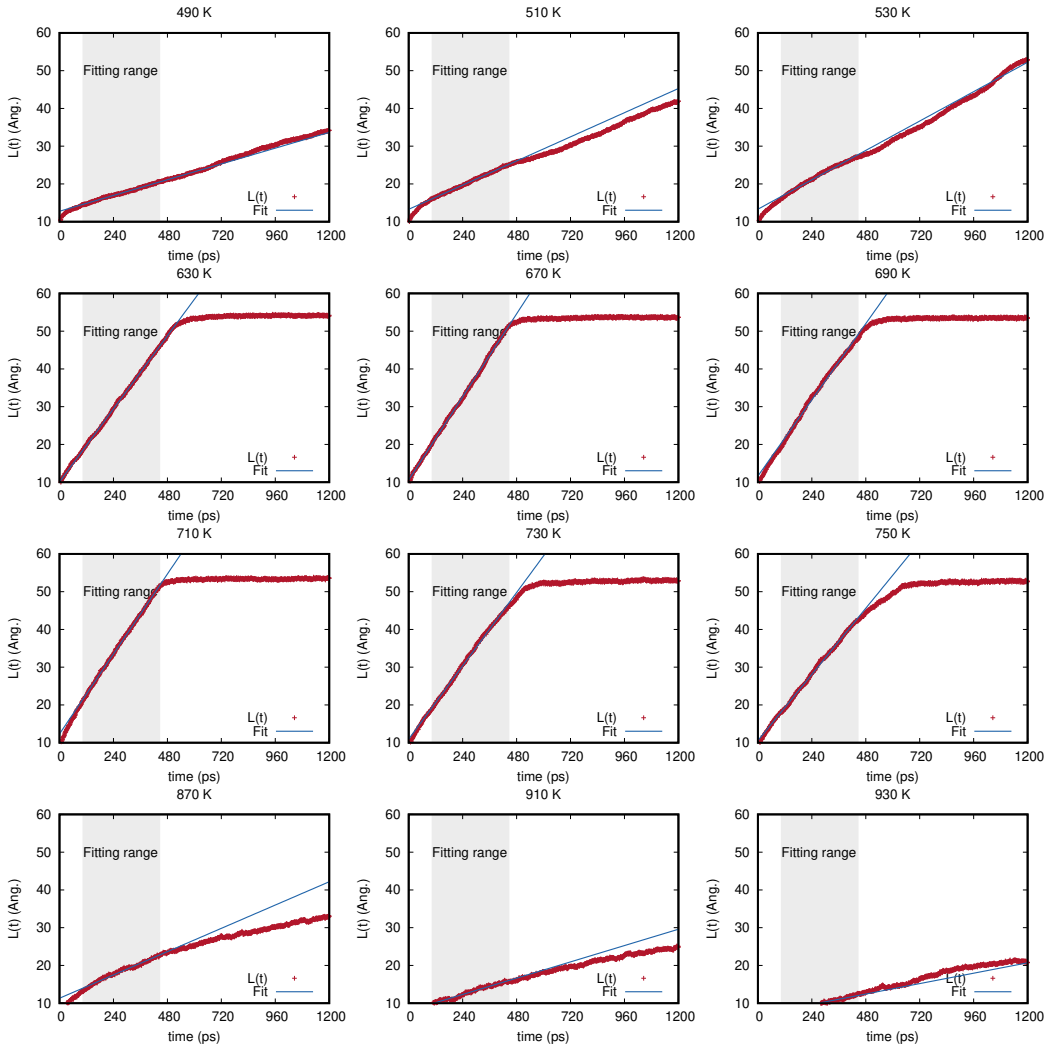

Figure 4.21: The evolution of the thickness of the crystalline slab $L(t)$ in simulations at different temperatures and their linear fit in the range highlighted in grey yielding the crystal growth velocity.

We attempted to fit the crystal growth velocity extracted from MD simulations with the WF equation with the D coefficient from the GC fit and $\Delta\mu$ given by Thomson and Spaepen formula $\Delta\mu(T) = \frac{\Delta H_m(T_m-T)}{T_m}\frac{2T}{T_m+T)}$ [189] where $\Delta H_m = 180$ meV/atom, $T_m = 940$ K, and D form CG formula. These values are those obtained from our MD simulation reported in Sec. 4.2.1. The resulting fit shown in Fig. 4.22 yields $\lambda = 6.2$ Å which seems too high for a typical jump length in the diffusion process.

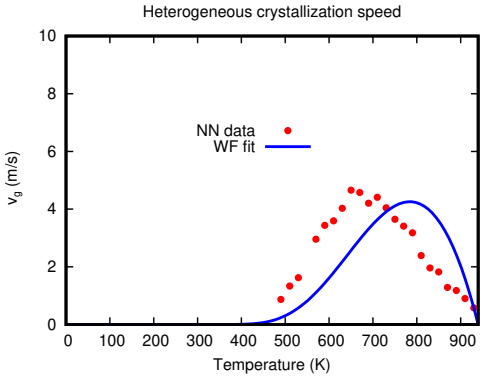

Figure 4.22: Crystal growth velocities from simulations of the heterogeneous crystallization and the Wilson–Frenkel fitting.

If, instead, we set λ to the same value obtained for GeTe in Ref. [19] (λ= 3 Å) which is a physically reasonable value, we obtain the WF curve shown in Fig. 4.23 which better reproduces the crystal growth velocity at low temperatures but largely overestimates v_g at high temperatures.

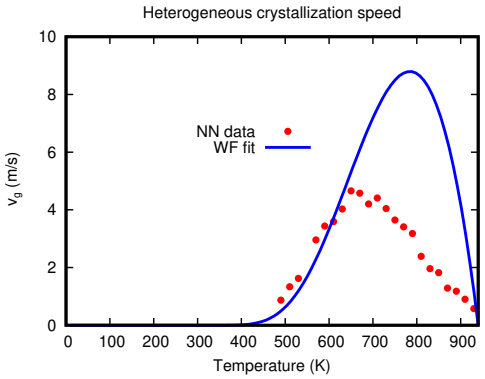

Figure 4.23: Crystal growth velocities from simulations of the heterogeneous crystallization and the WF fit with λ= 3 Å.

From Figs. 4.22 and 4.23 it is clear that the WF formula does not describe well the crystal growth velocity as a function of the temperature. However, the self-diffusion coefficient describes the long-scale atomic diffusion process while the term that enters in the kinetic prefactor u_{kin} for the crystallization is actually an effective atomic diffusion that might embody a more local atomic motion. One could then think of fitting the kinetic prefactor directly from the crystal growth velocities obtained from MD simulations. This new fit is reported in Fig. 4.24. The resulting parameters of the CG fit are B= 103 K, C=0.3 K and T_0=456 K, very similar to those obtained from experimental calorimetric measurements of B=121 K, C= 1.71 K and T_0=427 K [89].

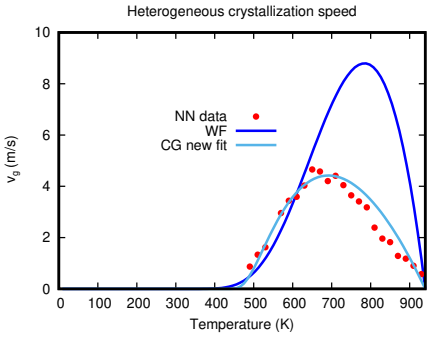

Figure 4.24: Crystal growth velocities (v_g) from simulations of the heterogeneous crystallization. The dark blue curve corresponds to WF fit with the diffusion parameters from MD simulations while the light blue curve corresponds to WF with u_{kin} fitted directly from v_g data.

This result shows that the effective kinetic term in the WF formula for the crystallization process in GST225 increases with temperature at a much lower pace than the diffusion coefficient does, which suggests that the kinetics prefactor is possibly controlled by a more local motion than the long-range diffusion which rules the coefficient D. This local motion would experience a lower activation energy resulting in a milder increase on the effective D by increasing temperature. On the other hand, one should also consider a possible error in the thermodynamic term used in WF formula. To check this possibility, we investigated the impact of the change of T_m and ΔH_m on the crystal growth velocity by fixing the kinetic prefactor. The result reported in Appendix E shows that changing T_m and ΔH_m in a reasonable range does not allow fixing the large misfit shown in Fig. 4.23.

We have also studied the crystallization in the bulk (homogeneous crystallization) of the supercooled liquid. To this aim, we generated a 7992-atoms cubic model of the liquid phase at 990 K as discussed previously. Then we quenched the model down to different temperatures in 80 ps MD simulations within the NVT ensemle and at the experimental density of the amorphous phase (0.031 atom/Å^3). Then, we performed long simulations up to 12 ns to crystallize the supercooled liquid and compute the crystal growth velocity. In Fig. 4.25 we show the profile of the potential energy as a function of time for different simulations showing the onset of the crystallization. From this picture, we can see clearly that a postcritical nucleus/nuclei form on a time scale of 0.2 to 3 ns in the temperature range 500-600 K. At 650 K a postcritical nucleus forms after about 7 ns while at 700 K the nucleation was not observed up to 20 ns. For temperatures where nucleation was not observed after a few tens of nanoseconds, the crystal growth velocities were calculated starting from a snapshot with a postcritical nucleus formed at a lower temperature. Moreover, we observe that the number of postcritical nuclei increases as temperature decreases (see Fig. 4.26). For the higher temperatures, we observe a single crystallite which gives rise to a uniform single crystal filling

the simulation box.

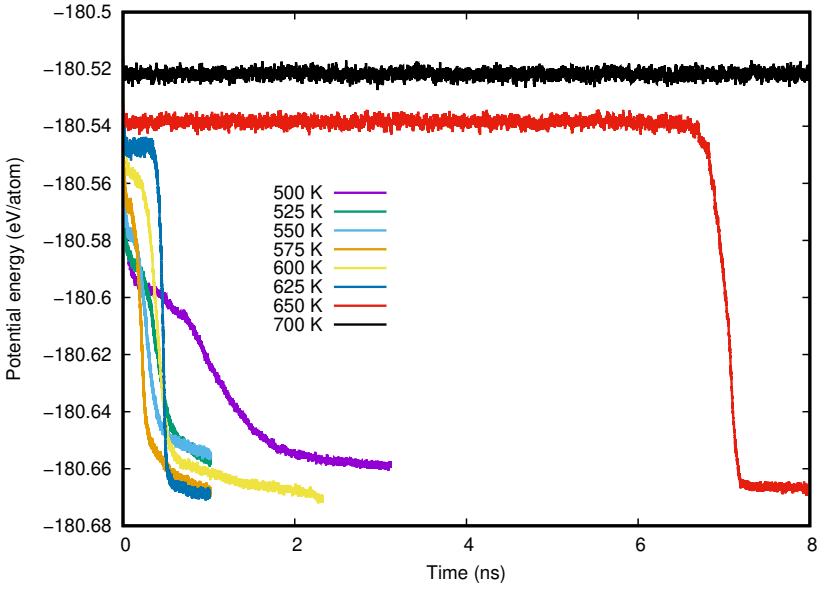

Figure 4.25: Potential energy profile as a function of time in simulations of the crystallization of supercooled liquid GST225 at different temperatures.

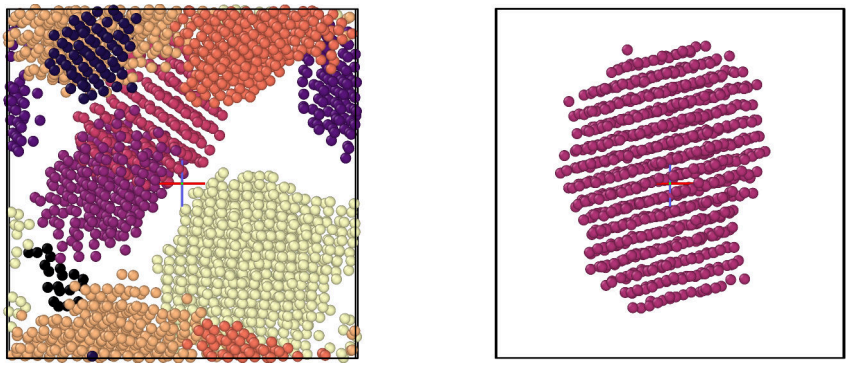

Figure 4.26: Snapshots of the formation of crystal nuclei in simulations at 500 K (left) and 650 K (right). Different crystalline nuclei are shown with different colors. Liquid-like atoms are not shown.

The crystalline atoms were labeled with the Q_4 parameter as discussed above. Then to distinguish different nuclei, crystalline atoms are assigned to a single crystalline nucleus when it falls within a 3.6 Å from the outermost atoms

of the nucleus. Then the evolution of the crystalline nuclei was monitored to evaluate v_g which in this case is given by:

$$v_g = \frac{dr_i(t)}{dt} \Rightarrow r_i(t) = \left(\frac{3N_i(t)}{4\pi\rho_{NN}^{cubic}} \right)^{\frac{1}{3}} \tag{4.4}$$

where N_i, is the number of atoms in a single nucleus and r_i is the radius of the i-nucleus, where we assumed a spherical shape. This assumption is valid only in the early stage of crystallization where a cluster does not interact with other clusters or its periodic image. The resulting v_g as a function of temperature and the WF fit with the kinetic prefactor fitted directly from the v_g data with the CG formula are shown in Fig. 4.27-averaged over different nuclei in a single simulation and over two independent simulations for some temperatures.

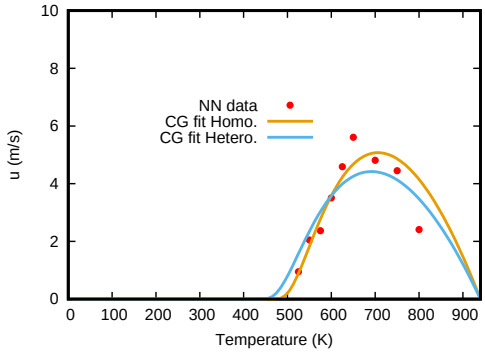

Figure 4.27: Crystal growth velocities from simulations in the bulk (red points) compared with the WF fit of the heterogeneous crystallization (see Fig. 4.24). The WF fit for the homogeneous crystallization is obtained by fitting directly the kinetic prefactor with the CG formula as in the heterogeneous case.

From Fig. 4.27 we notice that the heterogeneous crystal growth velocity is slightly smaller than the homogeneous one in the temperature range 600-700 K, which might be ascribed to the growth direction which is reduced to the <001> direction in the phase coexistence simulations while the crystal growth velocity obtained from the growth of a regularly spherical nucleus is an average over all different growth directions. However, we observe a variability of up to 2 m/s in v_g in different nuclei and therefore additional data are necessary to improve the statistics. Moreover, it is worth highlighting that the crystal growth velocity from NN-MD at 600 K is 4.2 (3.45) m/s in the homogeneous (heterogeneous) crystallization. This value has to be compared with other values obtained from DFT-MD at the same temperature, which vary from 5.5 m/s for small models, 0.3-1 m/s for intermediate models and 0.5 m/s for the largest model simulated with DFT [17, 72, 73, 90, 91, 92, 93, 94] while the experimental value is about 3 m/s [89].

So far we studied the kinetics of the crystallization without the inclusion of vdW interaction. The effect of vdW interaction on the crystallization kinetics is left to future work, as in the current implementation of DeePMD it is not possible to exploit the GPUs when NN is combined with D2, which makes these calculations more demanding.

4.4 Summary

In summary, as a first step towards the goal of large scale simulation of Ge-rich GST alloys, we developed a NN potential for GST225 capable of describing the structural and dynamical properties of this compound in the crystalline, liquid and amorphous phases over a large range of thermodynamics conditions. We have employed this potential to study the crystallization of GST225 both homogeneous and heterogeneous at the liquid crystal interface. By trying to fit the crystal growth velocity as a function of temperature with the WF phenomenological formula we found that the kinetic prefactor in GST225 is ill-described by the diffusion coefficient computed independently from MD simulations. A better description is given by a CG formula fitted directly on the kinetic prefactor of the crystal growth velocity extracted from MD simulations. The resulting parameters are in good agreement with those obtained experimentally from the crystal growth velocity inferred from DSC data. The NN crystal growth velocity as a function of temperature is in part very similar to the experimental data reported in Ref. [89] with a slightly higher maximum v_g for the NN at around 680 K, which is very close to the temperature at which the maximum of the v_g was observed experimentally.

Chapter 5

Conclusions

In summary, we carried out a DFT study on Ge-rich GST alloys which are of keen interest for embedded memory applications operating at high temperatures. These alloys decompose into crystalline Ge and less Ge-rich GST alloys upon crystallization. However, the details of this process are still largely unknown. To shed light on several issues regarding these materials at the microscopic level, we investigated the structural properties of amorphous Ge-rich GST alloys by means of DFT methods and we performed a high-throughput DFT study on the decomposition pathways of Ge-rich GST alloys. The analysis of amorphous models generated by quenching from the melt in DFT-MD allowed us to identify a few trends on the dependence of some structural features on the Ge content. Namely, we found that Ge-Ge homopolar bonds, Ge in tetrahedral geometry and long-membered rings instead of four-membered rings increase by increasing the Ge content. Since all these local features are not present in the crystal, the dissimilarity between the amorphous and crystalline cubic phase of GST alloys increases by raising the Ge content, which is also in agreement with another recent work [108]. We might expect that by increasing the dissimilarity between the amorphous and crystalline phase the crystal nucleation rate would decrease. Then we studied the phase separation upon crystallization based on thermodynamical analysis. First, we carried out an exploratory study on selected decomposition pathways of GST523, which has been studied because of its high T_X and because of a parallel study on this system carried out by an experimental group we were collaborating with.

We found that decomposition reactions into stoichiometric trigonal phases along the GeTe-Sb_2Te_3 pseudobinary line are the most thermodynamically favored, as one would expect. However, once we consider the cubic metastable crystalline phase as a possible product, several other decomposition channels into non-stoichiometric alloys become competitive [109]. Based on these results we carried out a comprehensive study by means of high-throughput DFT calculations [155]. First, we computed the formation free energy of all GST alloys in the central region of the phase diagram modeled into the cubic metastable phase. Then, we constructed the convex hull and we calculated the distance

of the formation free energy of each alloy from the convex hull, which gives a measure of the metastability of the non-stoichiometric compositions. These data allowed us to compute the reaction free energy of all the possible decomposition pathways of the GST alloys, which provided a decomposition map for each individual GST composition and its most probable decomposition products and/or competitive decomposition channels. The results for the GST523 alloy are in agreement with experimental results obtained by water quenching the liquid phase from an experimental work group we collaborated with. We collected the thermochemical data in a map of the decomposition propensity, which then allowed us to suggest a possible strategy to minimize the segregation of Ge by still keeping a high T_x, thanks to our knowledge on the structural properties of the amorphous phase as a function of the Ge content. This information has been exploited in a joint theoretical and experimental search for better performing Ge-rich GST alloys for embedded memories [167]. This work yielded a golden composition with a high T_x but a lower segregation of Ge, which is beneficial for the operation of the memory to reduce for instance the cell-to-cell variability.

Our thermochemical data showed that several thermodynamically favored competitive decomposition pathways with very similar reaction free energy are possible for Ge-rich GST alloys. However, not all decomposition paths might be viable due to kinetic effects.

In the last years, MD simulations based on DFT have been demonstrated to be a viable tool to investigate the crystallization kinetics of phase change materials. In the case of Ge-rich GST, mass transport due to phase separation into crystalline Ge requires simulation times that are beyond the reach of DFT methods. A possible strategy to overcome the limitation of DFT methods and to enlarge their scope is the development of interatomic potentials based on machine learning techniques for large-scale MD simulations. A machine learning scheme based on NN method was already exploited previously for the simpler GeTe and Sb phase change materials. In the perspective to develop a NN potential for Ge-rich GST, we have first tackled the problem of generating a potential for the stoichiometric GST225 compound. We succeed in this task by training a NN on a DFT database of energy and forces of about 180000 configurations of small cells (108 atoms). This procedure implemented in DeePMD code yields a potential suitable to describe the structural and dynamical properties of the crystalline, liquid and amorphous phases of GST225 with an unprecedented closeness to DFT results. As a first application of the NN potential we studied the kinetics of crystallization of GST225 in the supercooled liquid phase. Simulation with up to 12000 atoms and up to 20 ns long allowed us to compute the crystal growth velocity as a function of temperature, which turns out to be in very good agreement with the experimental data inferred from DSC. This potential is now ready to be exploited to address several open issues in the physics of this compound, such as a possible

fragile-strong transition in the supercooled liquid, the aging of the amorphous phase responsible for the drift in the electrical resistance, or the crystallization in confined geometries, just to name a few. Moreover, as already mentioned, the achievement of a reliable NN potential for GST225 represents the first step in the development of a NN potential to directly simulate the crystallization with phase separation of Ge-rich GST alloys by molecular dynamics. We can envisage that the simulations will be suitable to provide crucial insights on the crystallization kinetics that will aid the design of better performing Ge-rich GST alloys for memory applications.

Appendix A

Additional material on the decomposition of GST523

GST523, GST423, GST323 and GST221 were modeled in a cubic crystal similar to the metastable cubic phase of the GST225. The crystalline phase of these alloys was modeled in 216-atom supercells, which corresponds to a 3x3x3 cubic rocksalt supercell. Since in these Ge-rich alloys there are less than three p-electrons per site, stoichiometric vacancies are not expected to be present as observed in cubic GST225 [152]. In the Ge-rich alloys addressed here, Sb is supposed to behave as an amphoteric element due to the low content of Te, which introduces a disorder in the anionic sublattice besides the disorder present in the cationic sublattice. In order to take into account this additional complexity, a large supercell has to be considered, which is also needed to generate representative amorphous models. For each alloy, special quasi-random structures (SQS) [154] were generated using "The Alloy-Theoretic Automated Toolkit" [190] to properly include disorder in the two sublattices. Due to the constraint of 216 atoms, it was not always possible to generate models with the exact desired composition.

GST523 was modeled with the cationic sublattice fully occupied by Ge while the anionic one was occupied with a composition of $Sb_{0.4}/Te_{0.6}$. The resulting SQS has 64 atoms of Te and 44 atoms of Sb on the anionic sublattice and hence the actual composition is $Ge_5Sb_{2+x}Te_{3-x}$ where x is 0.0037.

In GST423, the cationic sublattice was modeled with a composition of $Ge_{0.888}/Sb_{0.111}$ and the anionic one with a composition of $Sb_{0.333}/Te_{0.666}$. A SQS was generated in which the cationic sublattice is occupied by 96 atoms of Ge and 12 atoms of Sb while the anionic sublattice is occupied by 36 atoms of Sb and 72 atoms of Te, which corresponds to the exact composition of GST423.

GST323 alloy is an isoelectronic alloy with exactly three p electrons per site on average, the cationic sublattice is occupied by Ge and Sb with a ratio of three to one, while the anionic sublattice is occupied by Te and Sb with the

same ratio. The resulting model has the cationic sublattice occupied by 81 atoms of Ge and 27 atoms of Sb. The anionic sublattice is, instead, occupied by 81 atoms of Te and 27 atoms of Sb, which correspond to the exact composition GST323.

Finally, the crystalline phase of GST221 was modeled with a composition of $Ge_{0.8}/Sb_{0.2}$ on the cationic sublattice while the anionic one with a composition of $Sb_{0.6}/Te_{0.4}$. In the SQS of this alloy, the cationic sublattice was occupied by 86 atoms of Ge and 22 atoms of Sb. The anionic sublattice was occupied by 64 atoms of Sb and 44 atoms of Te and hence the actual composition is $Ge_2Sb_2Te_{1+x}$ where x is 0.0023.

Besides these compositions which were studied in the amorphous phase, we also generated models of the cubic crystalline phase of GST223 and GST123 for the exploratory study of the decomposition reaction of GST523 as discussed in Sec. 3.2.

As GST223 and GST123 alloys have more than three p electrons per atom in the formula unit, we included vacancies in the cationic sublattice to enforce the presence of three p electrons per site in the rocksalt crystal on average. In GST223 the cationic sublattice is occupied by 60 atoms of Ge, 39 atoms of Sb and 9 vacancies and the anionic one is occupied by 87 atoms of Te and 21 atoms of Sb. The resulting composition corresponds to $Ge_2Sb_2Te_{2.9}$. The models of GST123 were generated with the cationic sublattice occupied by 33 atoms of Ge, 54 atoms of Sb and 21 vacancies and the anionic sublattice occupied by 96 atoms of Te and 12 atoms of Sb, which result in a composition of $GeSb_2Te_{2.909}$.

We have also generated two crystalline models for GST213 and GST243 which were observed experimentally as a product of the decomposition of GST523 as discussed in Sec. 3.2.3. In the model of GST213, the cationic sublattice is occupied by 12 vacancies, 68 atoms of Ge and 28 atoms of Sb. The anionic one is occupied by 6 atoms of Sb and 102 atoms of Te. Hence, our model has 204 atoms and 12 vacancies with an actual composition of $Vac_{1/3+x}Ge_2SbTe_3$ where x = 0.0196. In the model of GST243 we have 10 vacancies, 42 atoms of Ge and 56 atoms of Sb occupying the cationic sublattice while the anionic one is occupied by 36 atoms of Sb and 72 atoms of Te. Hence, the actual composition of this model is $Vac_{0.4347}Ge_{2-x}Sb_4Te_{3+y}$ where x = 0.174 and y = 0.1304.

The equilibrium density of the crystalline phase was obtained by fitting the total energy for various volumes with the Brich-Murnagham function. The internal geometry was fully relaxed by keeping a cubic supercell. The resulting equilibrium density and bulk modulus are given in Table A.1. Then, the equilibrium configuration was rescaled in order to get a model 8% lower in density as an initial configuration for simulation at 2000 K (the preparation of the

liquid phase).

Table A.1: Theoretical lattice parameter and bulk modulus of the Ge-rich GST alloys studied in the amorphous phase. The average values and the mean deviation refer to calculations over three independent SQS models. Data taken from our previous work [109]

alloy	a (Å)	density (atoms/Å^3)	bulk modulus (GPa)
GST523	5.893±0.004	0.0391±0.001	53±1
GST423	5.999±0.001	0.0371±0.001	33.3±0.8
GST323	6.141±0.001	0.03454±0.0002	49±1
GST223	6.138±0.001	0.0331±0.001	41±1
GST123	6.134±0.004	0.0313±0.0001	34.8±0.9
GST221	5.9670±0.006	0.0376±0.001	49.5±0.5
GST225	6.140	0.0311	-
GST213	6.094	0.0334	31.7
GST243	6.154	0.0327	36.0

We also have analyzed the rocksalt phase of these alloys at equilibrium and found that the structure of each alloy is distorted giving rise to longer and shorter bonds, similar to what occurs in GST225 (see Fig A.1).

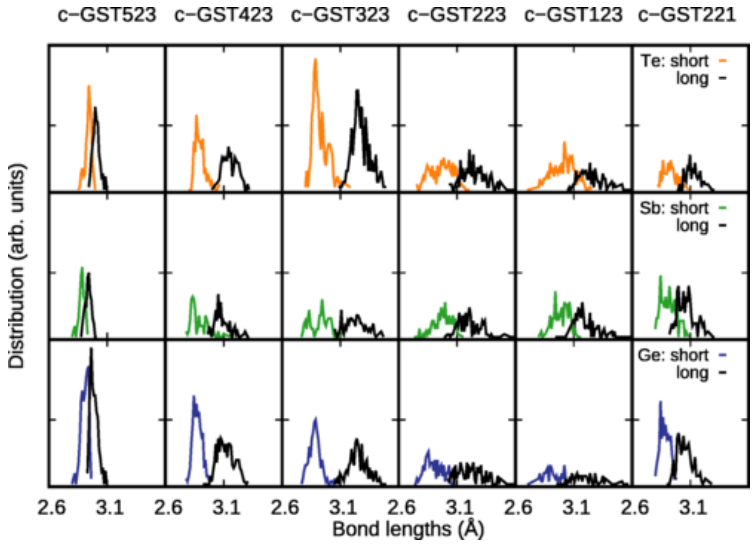

Figure A.1: Bond length distribution in crystalline Ge-rich GST alloys resolved for the three shorter and the three longer bonds and for the different chemical species. Taken from our previous work [109].

For the sake of comparison with the amorphous phase, we also computed the vibrational properties (see Fig. A.2 and Fig. A.3) and Raman spectra (see Fig. A.4) of GST523, GST423, GST323 and GST221 (see Sec. 3 for details on the methods).

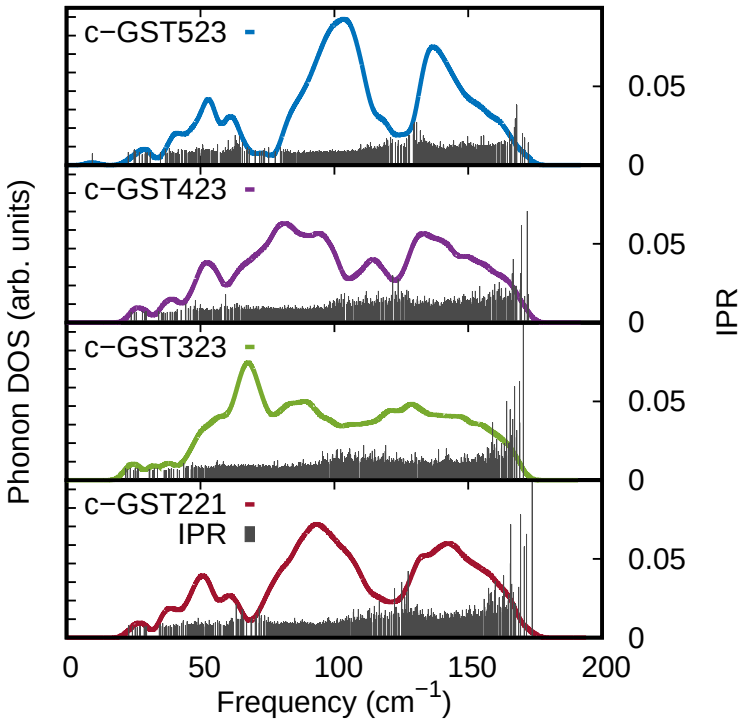

Figure A.2: Phonon DOS and inverse participation ratio (IPR) of crystalline Ge-rich GST alloys. Taken from our previous work [109].

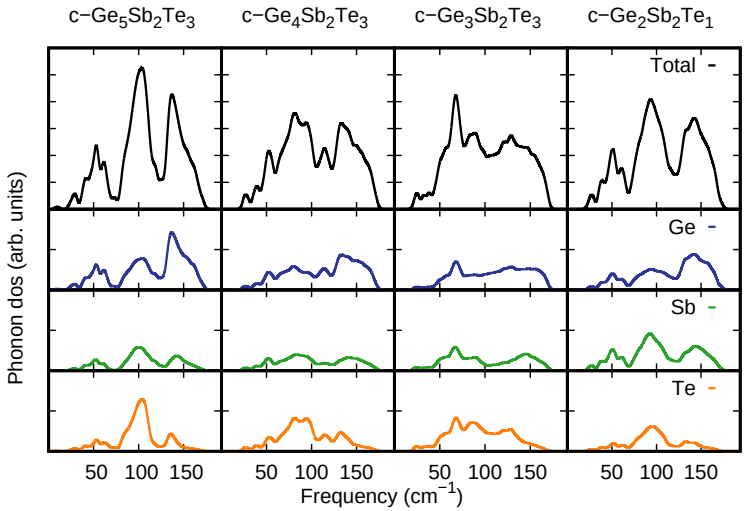

Figure A.3: The projection of phonon DOS on different types of atoms and for Ge in tetrahedral geometry in the crystalline phase of Ge-rich GST alloys. The DOS is obtained from Γ-point phonon energies broadened by a Gaussian function with a variance of 1.5 cm^{-1}. Taken from our previous work [109].

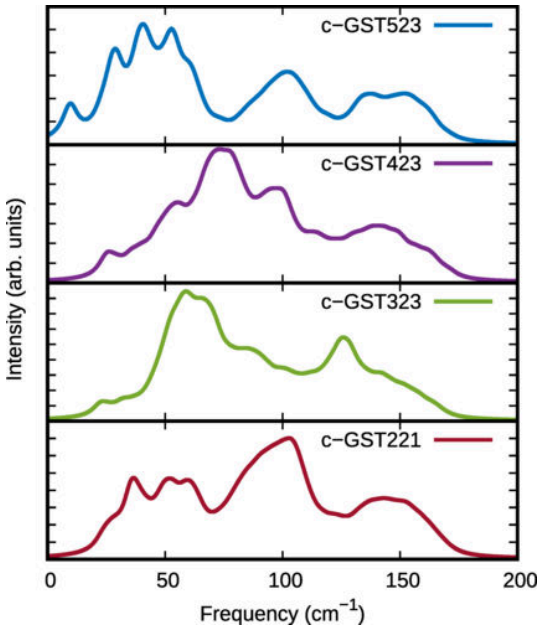

Figure A.4: Raman spectra of the crystalline phase of Ge-rich GST alloys in nonresonant conditions calculated from DFT phonons and the bond polarizability model in backscattering geometry for non-polarized light. Lorentzian smearing of 4 cm^{-1} was employed to broaden the peaks. Taken from our previous work [109].

The energy of these models, together with those of the amorphous models are reported in Tab. A.2. These energies were used to compute the reaction free energy of the decomposition of GST523 in an exploratory study as discussed in the introduction of chapter 3.2 for the crystalline phase and in Sec. 3.2.6 for the amorphous one. The energy of the crystalline phase was used to compute the reaction free energy for the decomposition of GSt523 along the different paths (1)-(12) discussed in 3.2 and given below:

$$
\begin{aligned}
\text{GST523} &\longrightarrow \tfrac{3}{4}\,\text{GST124} + \tfrac{1}{2}\,\text{Sb} + \tfrac{17}{4}\,\text{Ge} && (1)\\
\text{GST523} &\longrightarrow \tfrac{3}{5}\,\text{GST225} + \tfrac{4}{5}\,\text{Sb} + \tfrac{19}{5}\,\text{Ge} && (2)\\
\text{GST523} &\longrightarrow \tfrac{3}{6}\,\text{GST326} + \text{Sb} + \tfrac{7}{2}\,\text{Ge} && (3)\\
\text{GST523} &\longrightarrow 3\,\text{GeTe} + 2\,\text{Sb} + 3\,\text{Ge} && (4)\\
\text{GST523} &\longrightarrow \text{Sb}_2\text{Te}_3 + 5\,\text{Ge} && (5)\\
\text{GST523} &\longrightarrow \text{GST123} + 4\,\text{Ge} && (6)\\
\text{GST523} &\longrightarrow \text{GST223} + 3\,\text{Ge} && (7)\\
\text{GST523} &\longrightarrow \text{GST323} + 2\,\text{Ge} && (8)\\
\text{GST523} &\longrightarrow \text{GST423} + \text{Ge} && (9)\\
\text{GST523} &\longrightarrow \text{GST221} + 2\,\text{GeTe} + \text{Ge} && (10)\\
\text{GST523} &\longrightarrow \text{GST213} + 3\,\text{Ge} + \text{Sb} && (11)\\
\text{GST523} &\longrightarrow \tfrac{1}{2}\,\text{GST243} + \tfrac{3}{2}\,\text{GeTe} + \tfrac{5}{2}\,\text{Ge} && (12)
\end{aligned}
$$

Since our 216-atom cell has a small deviation from stoichiometry reactions (1)-(12) in Sec. 3.2 actually are:

$$Ge_{108}Sb_{44}Te_{64} \longrightarrow 16GeSb_2Te_4 + 12Sb + 92Ge \quad (1')$$

$$Ge_{108}Sb_{44}Te_{64} \longrightarrow \tfrac{64}{5}Ge_2Sb_2Te_5 + \tfrac{92}{5}Sb + \tfrac{412}{5}Ge \quad (2')$$

$$Ge_{108}Sb_{44}Te_{64} \longrightarrow \tfrac{64}{6}Ge_3Sb_2Te_6 + \tfrac{136}{6}Sb + \tfrac{456}{6}Ge \quad (3')$$

$$Ge_{108}Sb_{44}Te_{64} \longrightarrow 64GeTe + 44Ge + 44Sb \quad (4')$$

$$Ge_{108}Sb_{44}Te_{64} \longrightarrow 21Sb_2Te_3 + 107Ge + 2Sb + GeTe \quad (5')$$

$$Ge_{108}Sb_{44}Te_{64} \longrightarrow Ge_{22}Sb_{44}Te_{64} + 86Ge \quad (6')$$

$$Ge_{108}Sb_{44}Te_{64} \longrightarrow Ge_{40}Sb_{40}Te_{58} + 2Sb_2Te_3 + 68Ge \quad (7')$$

$$Ge_{108}Sb_{44}Te_{64} \longrightarrow Ge_{63}Sb_{42}Te_{63} + GeTe + 44Ge + 2Sb \quad (8')$$

$$Ge_{108}Sb_{44}Te_{64} \longrightarrow Ge_{84}Sb_{42}Te_{63} + GeTe + 23Ge + 2Sb \quad (9')$$

$$Ge_{108}Sb_{44}Te_{64} \longrightarrow Ge_{43}Sb_{43}Te_{22} + 42GeTe + 23Ge + Sb \quad (10')$$

$$Ge_{108}Sb_{44}Te_{64} \longrightarrow Ge_{43}Sb_{43}Te_{22} + 42GeTe + 23Ge + Sb \quad (11')$$

$$Ge_{108}Sb_{44}Te_{64} \longrightarrow Ge_{43}Sb_{43}Te_{22} + 42GeTe + 23Ge + Sb \quad (12')$$

Finally, the reaction free energy for the exploratory study on the decomposition pathways of GST523 in the crystalline phase are reported in Tab. A.3.

Table A.2: Total DFT energy of the different GST alloys in the crystalline and amorphous phases. The ideal entropy of mixing for the crystalline phase is also given. The error bar is obtained by averaging over three different SQS models. Data taken from our previous work [109].

Compound	Energy (eV/atom)	S (meV/K/atom)	S (meV/K/f.u.)
Ge	-107.1350	-	-
Sb	-150.8936	-	-
GeTe	-164.8953	-	-
GeTe (amorphous)	-164.7736	-	-
Sb_2Te_3	-193.9511	-	-
$Ge_1Sb_2Te_{2.909}$	-178.749±0.004	0.05837	0.3891
$Ge_2Sb_2Te_{2.9}$	-168.325±0.002	0.05992	0.4394
$Ge_3Sb_2Te_3$	-161.366±0.001	0.04845	0.3876
$Ge_3Sb_2Te_3$ (amorphous)	-161.2696	-	-
$Ge_4Sb_2Te_3$	-155.3120±0.001	0.04244	0.3820
$Ge_4Sb_2Te_3$ (amorphous)	-155.2332	-	-
$Ge_{4.9095}Sb_2Te_{2.909}$	-150.204±0.003	0.02899	0.2899
$Ge_{4.9095}Sb_2Te_{2.909}$ (amorphous M1)	-150.13984	-	-
$Ge_{4.9095}Sb_2Te_{2.909}$ (amorphous M2)	-150.1334	-	-
$Ge_2Sb_2Te_1$	-148.015±0.001	0.05056	0.2528
$Ge_2Sb_2Te_1$ (amorphous)	-147.9471	-	-
$GeSb_2Te_3$	-172.1560		
$Ge_{1.83}Sb_4Te_{3.13}$	-166.9966		

Table A.3: Reaction energy, configurational and vibrational contributions to the reaction free energy and total reaction free energy for reactions (1)-(12) in the crystalline phase. A negative energy indicates an exothermic reaction. The reactions here are labeled by their main product. Data taken from our previous work [109]

Reaction/main product	Reaction energy 0 K (meV/atom)	Configurational reaction free energy at 300 K (meV/atom)	Vibrational reaction free energy at 300 K (meV/atom)	Total reaction free energy at 300 K (meV/atom)
(1) GST124 trig.	-76	8.7	-	-67
(2) GST225 trig.	-75	8.7	-	-66
(3) GST326 trig.	-74	8.7	-	-66
(4) GeTe trig.	-73	8.7	-	-65
(5) Sb_2Te_3 trig.	-73	8.7	-	-64
(6) GST123	-32	-1.8	-	-34
(7) GST223	-44	-3.8	-	-47
(8) GST323	-51	-2.9	2.5	-51
(9) GST423	-26	-2.8	1.1	-28
(10) GST221	-35	1.1	-	-32
(11) GST213	-55	1.1.8	-	-54
(12) GST243	-50	1	-	-50

Appendix B

Structural properties of amorphous GST212

As for the other Ge-rich GST alloys, a 216-atom SQS of the cubic metastable phase was chosen as the initial configuration for GST212. In this SQS the cationic (anionic) sublattice is occupied by 86 atoms of Ge (Te) and 22 atoms of Sb resulting in an actual composition of $Ge_2Sb_{1.02}Te_2$. The equilibrium density of the crystalline phase is 0.0345 atom/Å^3 which corresponds to a lattice parameter of 6.131 Å. To generate an amorphous model we first equilibrated a liquid model at a density of 0.0318 atoms/Å^3, which is 8% lower than the theoretical equilibrium density of the cubic phase. The amorphous model was generated by quenching from the melt at 1000 K to 300 K in NPT simulation in 100 ps. The equilibrium density at 300 K of 0.0313 atoms/Å^3 was obtained from a NPT simulation 6 ps long. The structural properties were computed over a 12 ps NVT simulation. Total and partial pair correlation functions are reported in Fig. B.1 while the bond angle distribution function is shown in Fig. B.2. The distribution of the coordination numbers, shown in Fig B.3, was obtained by integrating the pair correlation function up to the cutoff thresholds used for other alloys in Sec. 3 (as shown in Fig. B.1). Average coordination numbers for the different pairs of atoms are reported in Tab. B.1 while the fraction of the different types of bonds in the amorphous model is reported in Tab. B.2. Finally, the distribution of the local order parameter q for different atoms and different local environments is shown in Fig B.4. Regarding to the medium-range structure, we report the distribution of ring length in Fig. B.5.

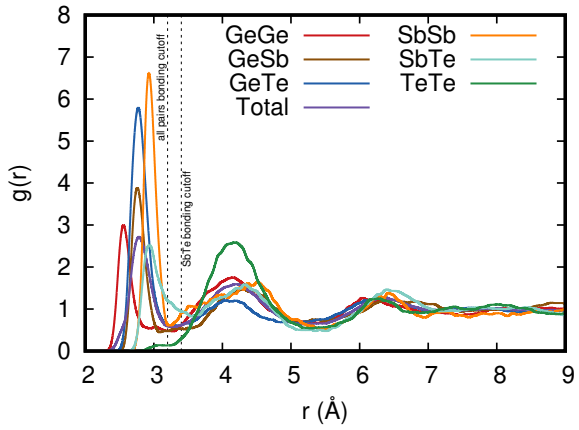

Figure B.1: Total and partial pair correlation functions in amorphous GST212. Vertical dashed lines indicate the bonding cutoff used to define the coordination numbers. Taken from our work [141].

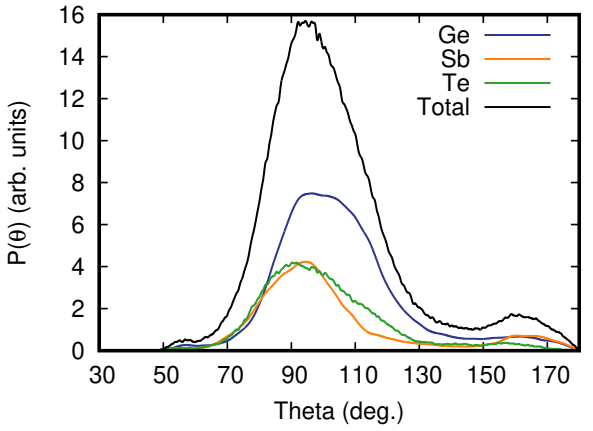

Figure B.2: Bond angle distribution function in amorphous GST212. Taken from our work [141].

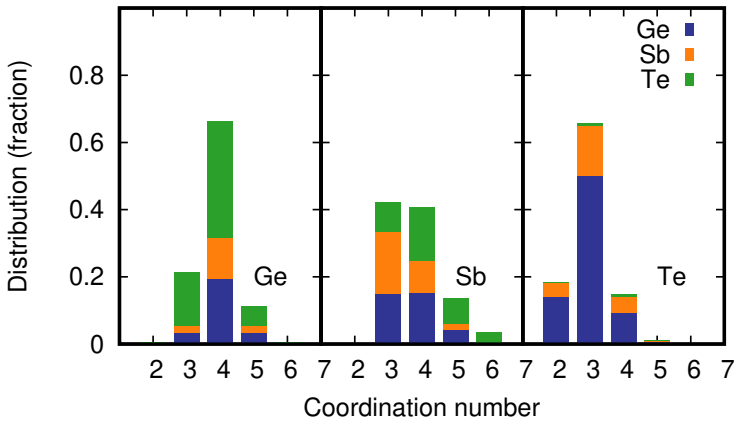

Figure B.3: Coordination numbers distribution in amorphous GST212 obtained by using the same bonding cutoff used for Ge-rich GST alloys as shown by the partial pair correlation functions in Fig B.1. Taken from our work [141].

Table B.1: Average coordination numbers for different pairs of atoms in amorphous GST212. Data taken from our work [141].

-	Total	With Ge	With Sb	With Te
Ge	3.90	1.06	0.66	2.18
Sb	3.78	1.29	1.03	1.46
Te	2.98	2.18	0.75	0.05

Table B.2: Percentage fraction (%) of the different types of bonds in amorphous GST212. Data taken from our work [141].

-	Ge	Sb	Te
Ge	12.0	-	-
Sb	15.0	6	-
Te	49.5	16.9	0.6

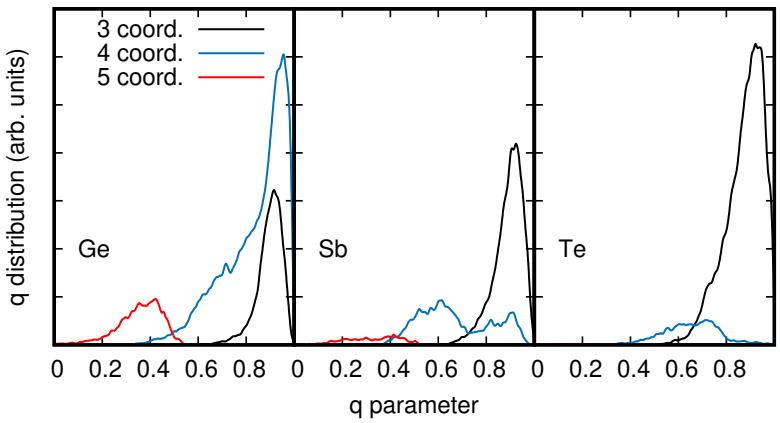

Figure B.4: Distribution of q-parameter resolved for atomic species and coordination number in amorphous GST212. Taken from our work [141].

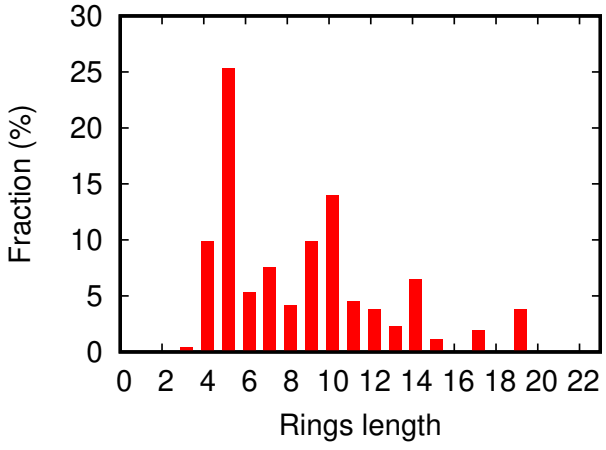

Figure B.5: Ring length distribution in amorphous GST212. Taken from our work [141].

Appendix C

Additional material on amorphous $Ge_2Sb_2Te_5$

In this appendix, we compare the structural properties of amorphous GST225 obtained from DFT MD simulations with two distinct GTH pseudopotentials for Ge. The first one, which was employed so far for all the simulations, treats explicitly only 4 valence electrons for Ge while the second one includes also the d-electrons of the core in the electronic problem.

To this end, we generated an amorphous model with the softcore pseudopotential by quenching from the melt following the same protocol used so far to generate amorphous models. As the new pseudopotential also treats core electrons, which are closer to the nucleus, we needed to increase the plane waves cutoff to 700 Ry to converge the forces acting on atoms.

Total and partial pair correlation functions obtained with the two pseudopotential are compared in Fig. C.1. A comparison of the bond angle distribution function is shown in Fig. C.2 while the distribution of the coordination numbers, obtained by integrating the pair correlation function up to the cutoff thresholds defined in Fig. C.1, is shown in Fig C.3. Finally, the distribution of the local order parameter q for different atoms and different local environments is shown in Fig C.4. By integrating the distribution of the q-parameter for four-coordinated Ge between 0.8 and 1 we can estimate the average fraction of Ge-atoms in tetrahedral geometry (see Sec. 3.1). This fraction is ranges between 23-33% in amorphous models generated with the four-electrons pseudopotential and to 17% in our model generated with the softcore pseudopotential. Finally, regarding the medium-range order, we compare the distribution of ring length in Fig. C.5.

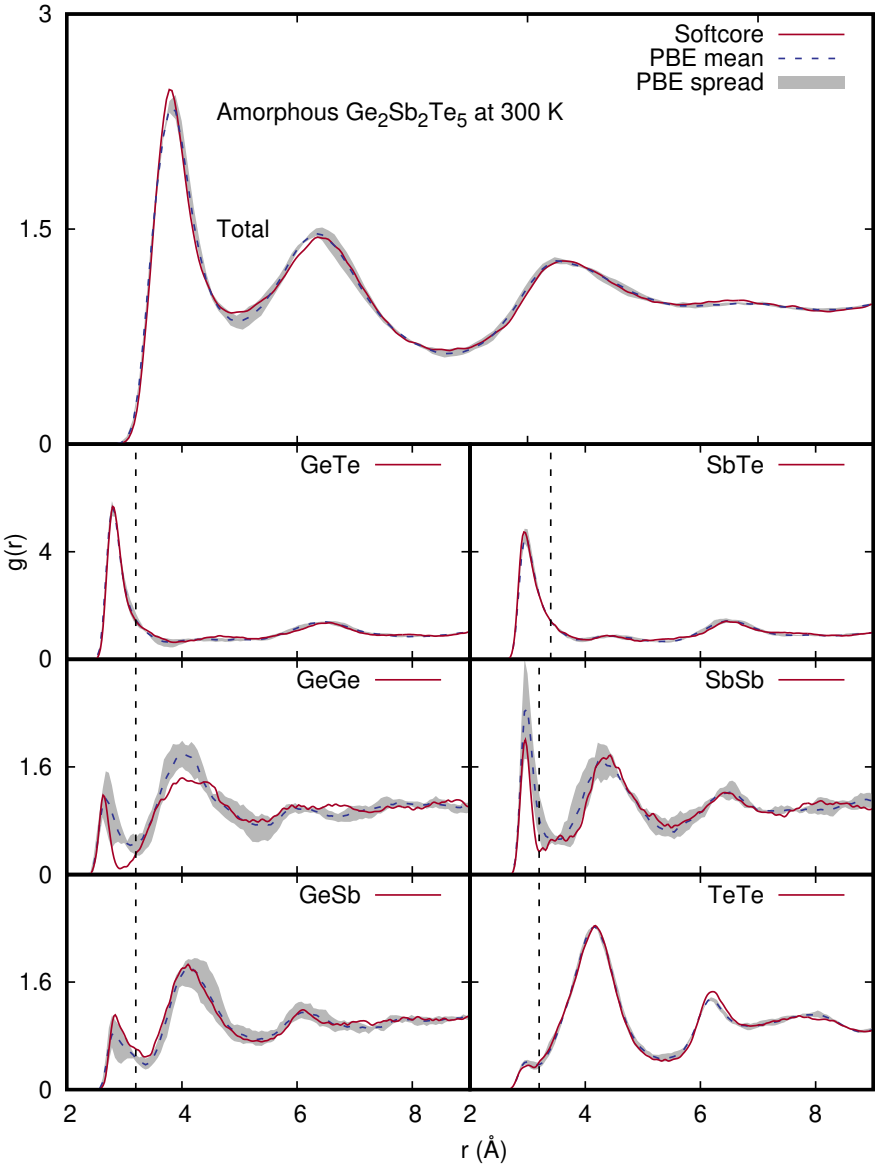

Figure C.1: Total and partial pair correlation functions in amorphous GST225 with the four-electrons pseudopotential (PBE) and the softcore one (softcore). Vertical dashed lines indicate the bonding cutoff used to define the coordination numbers.

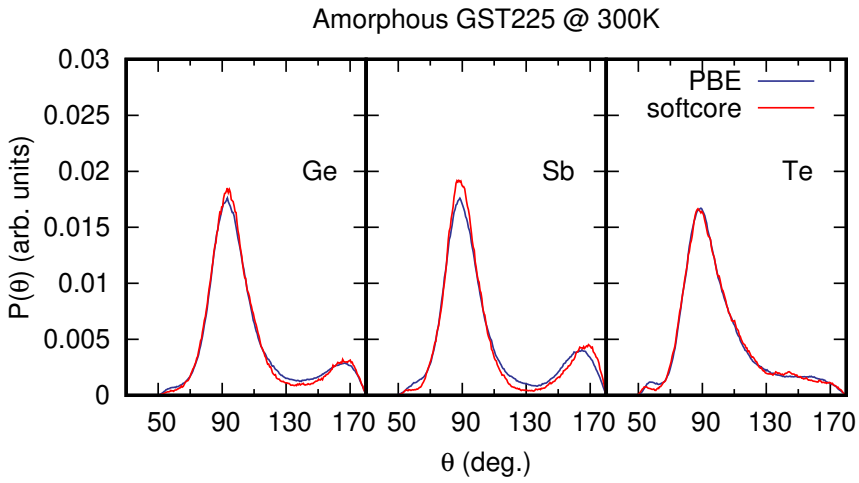

Figure C.2: A comparison of the bond angle distribution function in amorphous GST225 with the softcore pseudopotential and the four-electrons one.

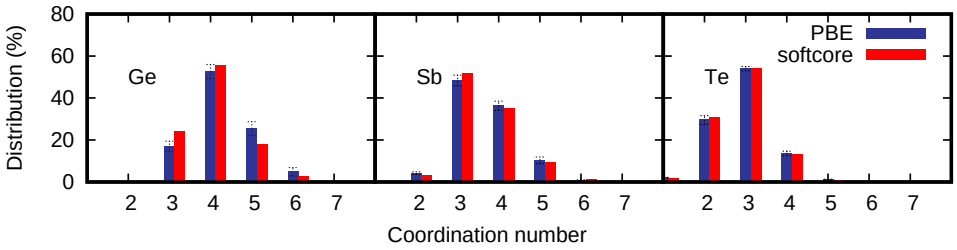

Figure C.3: Coordination numbers distribution in amorphous GST225 obtained by using the same bonding cutoff used for Ge-rich GST alloys as shown by the partial pair correlation functions in Fig C.1 with the two pseudopotentials.

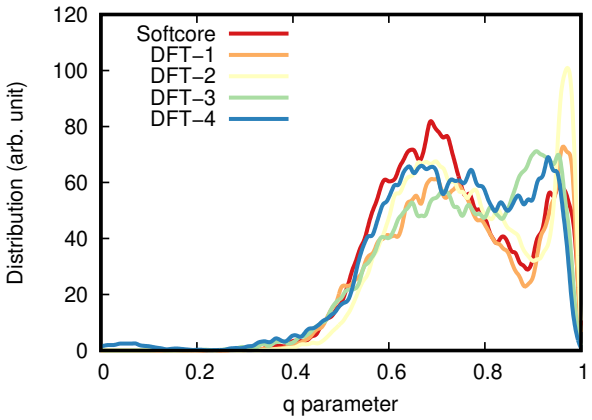

Figure C.4: Distribution of q-parameter for four-coordinated Ge in amorphous GST225 for the softcore model and for each of our four DFT models.

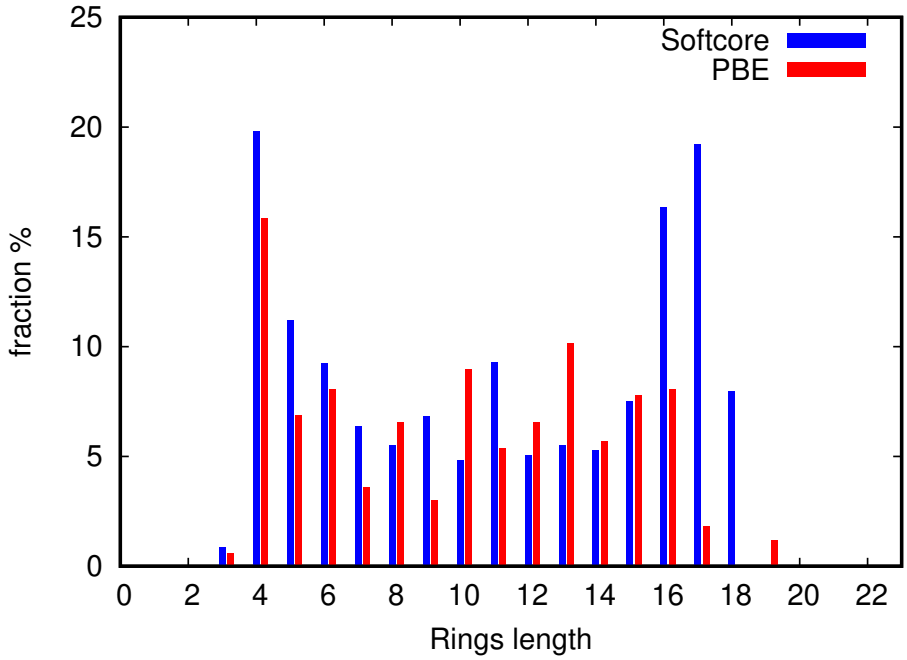

Figure C.5: A comparison of the distribution of ring length in amorphous GST225 with the softcore pseudopotential and the four-electrons one. four-electrons pseudopotential data are taken from Ref. [142]

Appendix D

Order parameter Q4

In order to study the crystallization process and to estimate the evolution of supercritical nuclei, we need to be able to distinguish between crystalline-like atoms and liquid-like atoms. To this end, we employed the Steinhardt order parameter Q_4 [188] which allows measuring the ordering degree of the first coordination shell for an atom which for the i-th atom is given by:

$$Q_{4,i} = \sqrt{\frac{2\pi}{9} \sum_{m=-4}^{4} q_{4m,i} q^*_{4m,i}} \tag{D.1}$$

where

$$q_{4m,i} = \sum_{j=1}^{N_i} Y_{4m}\left(\mathbf{r}_{ij}\right) \tag{D.2}$$

where j runs over the neighbors up to a given cutoff (3.6 Å in our case), Y_4^m is the fourth order spherical harmonic with degree m, $\mathbf{r}_{ij}$ is the vector connecting the two atoms and N_i is the number of neighbors of the i-th atom..

In general the distribution of q_4 in the cubic and the amorphous phase displays a large overlap which makes it not very suitable for quantitative analysis. Hence, we have employed the Q_4^{dot} which is defined as:

$$Q^{dot}_{4,i}(i) = \frac{1}{N_i} \sqrt{\sum_{j=1}^{N_i} \sum_{m=-4}^{4} q_{4m,i} q^*_{4m,j}} \tag{D.3}$$

where this new definition enhances the capability of this order parameter as it takes into account also the crystallinity of the local environment of the central atom.

In Fig. D.1 we report the distribution of Q_4^{dot} for the crystalline and supercooled liquid phase at 600K. There is a small overlap between these two distributions. We chose a threshold of Q_4^{dot}=0.87 to consider an atom a crystalline one.

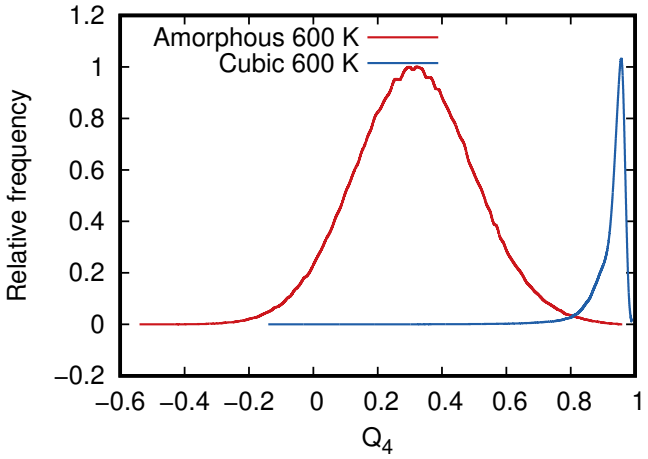

Figure D.1: Distribution of the Q_4^{dot} parameter for of the liquid and the cubic phase of GST225 at 600 K.

Appendix E

Additional material on the crystallization of $Ge_2Sb_2Te_5$

As we discussed in section 4.3, MD data on the crystal growth velocity can be reproduced by the phenomenological WF function only by fitting directly the kinetic prefactor on MD data. The use of the diffusion coefficient computed independently from MD simulations lead to a large overestimation of v_g at high temperature. This result might, however, suggest that the thermodynamics factor in WF formula could be not sufficiently accurate. We investigated the dependence of the thermodynamic factor on the choice of the parameters entering the expression of $\Delta\mu$. We show that by keeping the kinetic prefactor fixed to $4D/\lambda$ with λ= 3 Å and by changing T_m and ΔH_m parameters within a reasonable range, we can not improve the fit. This is shown in Fig. E.1 repeating the WF fitting by varying T_m in the range 860-940 K and ΔH_m in the range 120-240 meV/atom. From these comparisons, we can conclude that the inadequacy of the WF formula in reproducing the data can not be due to the uncertainties in our calculation of $\Delta\mu$.

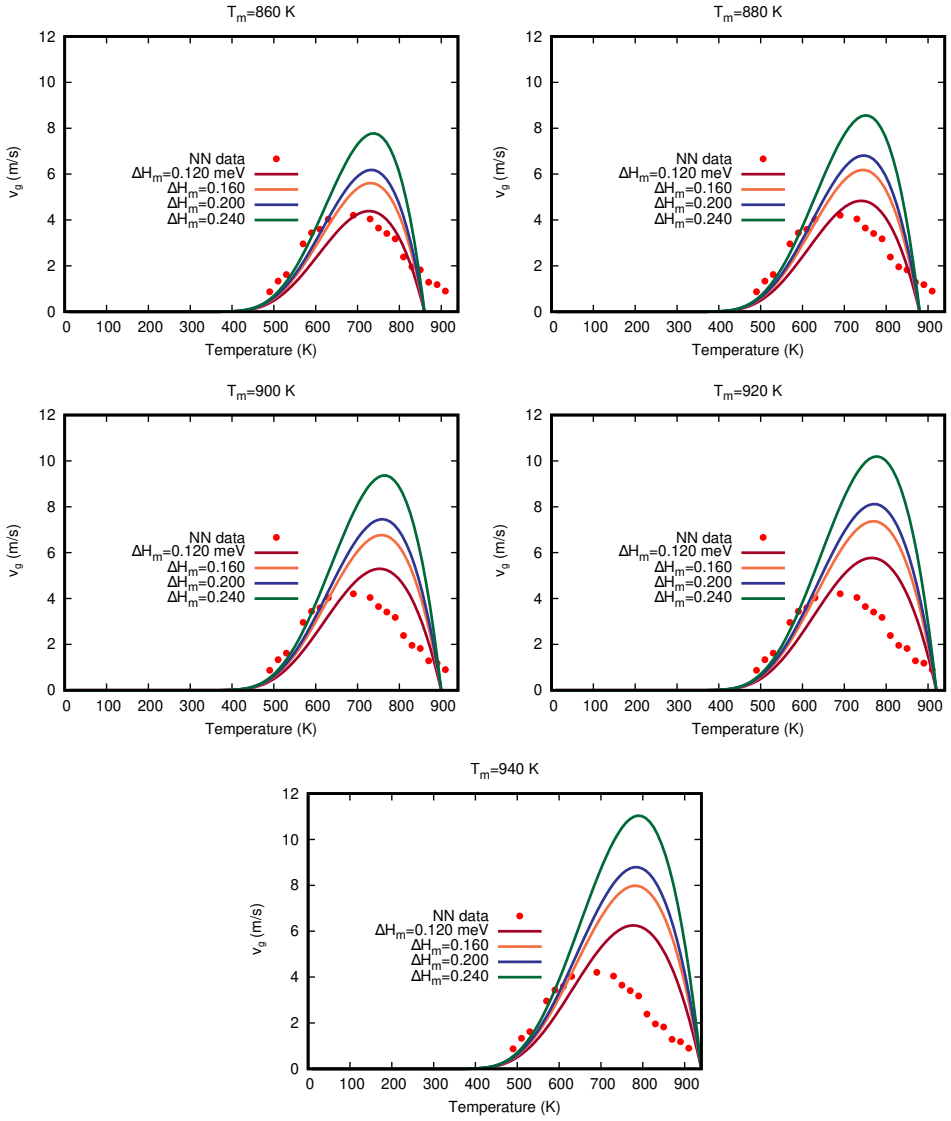

Figure E.1: Crystal growth velocity fitted with WF formula and the Thomas-Spaepen expression for $\Delta\mu$ with T_m and ΔH_m in the range 860-940 K and 160-240 meV. In each panel curves with different ΔH_m at fixed T_m are shown.

We also checked that the Thomson-Spaepen formula is fairly accurate in our case by computing $\Delta\mu$ from the integration of the specific heat as:

$$\Delta\mu(T) = \Delta H_m(1 - \frac{T}{T_m}) - \int_T^{T_m} \Delta C_p dT + T \int_T^{T_m} \frac{\Delta C_p}{T} dT \qquad \text{(E.1)}$$

where ΔC_p is the difference in C_p between the amorphous and the crystalline phases. We approximated ΔC_p with ΔC_v which was in turn computed from the caloric curve at fixed density. The resulting $\Delta\mu$ is compared to that obtained from Thomson-Spaepan approximation in Fig. E.2. The mild difference has a very marginal effect on the thermodynamic factor in the WF formula in the temperature range 600-900K.

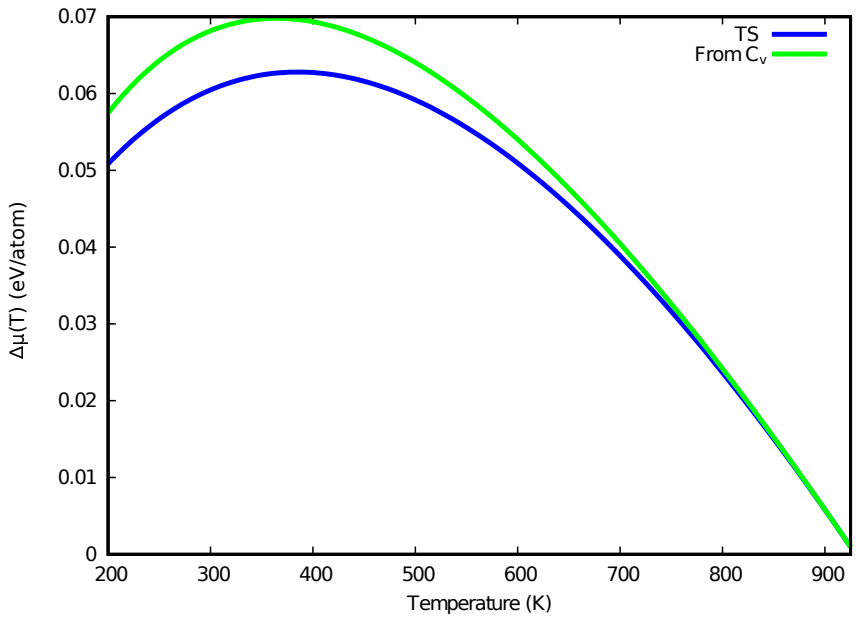

Figure E.2: $\Delta\mu$ as a function of temperature with Thomson-Spaepen (TS) and with the integration of the heat capacity C_v (formula D.1).

Bibliography

[1] M. Wuttig and N. Yamada, "Phase-change materials for rewriteable data storage," *Nat. Mater*, vol. 6, no. 11, p. 824, 2007.

[2] P. Noé, C. Vallée, F. Hippert, F. Fillot, and J.-Y. Raty, "Phase-change materials for non-volatile memory devices: from technological challenges to materials science issues," *Semiconductor Science and Technology*, vol. 33, no. 1, p. 013002, 2017.

[3] W. Zhang, R. Mazzarello, M. Wuttig, and E. Ma, "Designing crystallization in phase-change materials for universal memory and neuro-inspired computing," *Nat. Rev. Mater.*, vol. 4, no. 3, p. 150, 2019.

[4] J. Choe, "Intel 3D XPoint Memory Die Removed from Intel Optane™ PCM (Phase Change Memory)," 2017.

[5] T. Morikawa, K. Kurotsuchi, M. Kinoshita, N. Matsuzaki, Y. Matsui, Y. Fujisaki, S. Hanzawa, A. Kotabe, M. Terao, H. Moriya, *et al.*, "Doped In-Ge-Te phase change memory featuring stable operation and good data retention," in *2007 IEEE International Electron Devices Meeting*, IEEE, 2007.

[6] E. T. Kim, J. Y. Lee, and Y. T. Kim, "Investigation of electrical characteristics of the $In_3Sb_1Te_2$ ternary alloy for application in phase-change memory," *Phys. Status Solidi RRL*, vol. 3, no. 4, p. 103, 2009.

[7] H.-Y. Cheng, S. Raoux, and J. L. Jordan-Sweet, "The crystallization behavior of stoichiometric and off-stoichiometric Ga–Sb–Te materials for phase-change memory," *Appl. Phys. Lett.*, vol. 98, no. 12, p. 121911, 2011.

[8] Y. Kim, U. Hwang, Y. J. Cho, H. Park, M.-H. Cho, P.-S. Cho, and J.-H. Lee, "Change in electrical resistance and thermal stability of nitrogen incorporated $Ge_2Sb_2Te_5$ films," *Appl. Phys. Lett.*, vol. 90, no. 2, p. 021908, 2007.

[9] G. B. Beneventi, L. Perniola, V. Sousa, E. Gourvest, S. Maitrejean, J. Bastien, A. Bastard, B. Hyot, A. Fargeix, C. Jahan, *et al.*, "Carbon-doped GeTe: a promising material for phase-change memories," *Solid State Electron*, vol. 65, p. 197, 2011.

[10] H. Y. Cheng, T. H. Hsu, S. Raoux, J. Wu, P. Y. Du, M. Breitwisch, Y. Zhu, E. K. Lai, E. Joseph, S. Mittal, R. Cheek, A. Schrott, S. C. Lai, H. L. Lung, and C. Lam, "A high performance phase change memory with fast switching speed and high temperature retention by engineering the $Ge_xSb_yTe_z$ phase change material," in *2011 International Electron Devices Meeting*, p. 3.4.1, 2011.

[11] F. Disegni, A. Ventre, A. Molgora, P. Cappelletti, R. Badalamenti, P. Ferreira, G. Castagna, A. Cathelin, A. Gandolfo, A. Redaelli, D. Manfrè, A. Maurelli, C. Torti, F. Piazza, M. Carfì, F. Arnaud, M. Perroni, M. Caruso, S. Pezzini, R. Annunziata, G. Piazza, O. Weber, and M. Peri, "16MB high density embedded PCM macrocell for automotive-grade microcontroller in 28nm FD-SOI, featuring extension to 24MB for over-the-air software update," in *2021 Symposium on VLSI Circuits*, p. 1, 2021.

[12] P. Zuliani, E. Varesi, E. Palumbo, M. Borghi, I. Tortorelli, D. Erbetta, G. D. Libera, N. Pessina, A. Gandolfo, C. Prelini, L. Ravazzi, and R. Annunziata, "Overcoming temperature limitations in phase change memories with optimized $Ge_xSb_yTe_z$," *IEEE Transactions on Electron Devices*, vol. 60, no. 12, p. 4020, 2013.

[13] P. Zuliani, E. Palumbo, M. Borghi, G. Dalla Libera, and R. Annunziata, "Engineering of chalcogenide materials for embedded applications of phase change memory," *Solid State Electron*, vol. 111, p. 27, 2015.

[14] N. Ciocchini, E. Palumbo, M. Borghi, P. Zuliani, R. Annunziata, and D. Ielmini, "Modeling resistance instabilities of set and reset states in phase change memory with Ge-rich GeSbTe," *IEEE Transactions on Electron Devices*, vol. 61, no. 6, p. 2136, 2014.

[15] S. Caravati, M. Bernasconi, T. Kühne, M. Krack, and M. Parrinello, "Coexistence of tetrahedral-and octahedral-like sites in amorphous phase change materials," *Appl. Phys. Lett.*, vol. 91, no. 17, p. 171906, 2007.

[16] J. Akola and R. Jones, "Structural phase transitions on the nanoscale: The crucial pattern in the phase-change materials $Ge_2Sb_2Te_5$ and GeTe," *Phys. Rev. B*, vol. 76, no. 23, p. 235201, 2007.

[17] J. Hegedüs and S. Elliott, "Microscopic origin of the fast crystallization ability of Ge–Sb–Te phase-change memory materials," *Nat. Mater*, vol. 7, no. 5, p. 399, 2008.

[18] J. Behler and M. Parrinello, "Generalized neural-network representation of high-dimensional potential-energy surfaces," *Phys. Rev. Lett.*, vol. 98, p. 146401, 2007.

[19] G. C. Sosso, G. Miceli, S. Caravati, J. Behler, and M. Bernasconi, "Neural network interatomic potential for the phase change material GeTe," *Phys. Rev. B*, vol. 85, p. 174103, 2012.

[20] D. Dragoni, J. Behler, and M. Bernasconi, "Mechanism of amorphous phase stabilization in ultrathin films of monoatomic phase change material," *Nanoscale*, vol. 13, no. 38, p. 16146, 2021.

[21] G. C. Sosso, G. Miceli, S. Caravati, F. Giberti, J. Behler, and M. Bernasconi, "Fast crystallization of the phase change compound GeTe by large-scale molecular dynamics simulations," *J. Phys. Chem. Lett.*, vol. 4, no. 24, p. 4241, 2013.

[22] S. Gabardi, E. Baldi, E. Bosoni, D. Campi, S. Caravati, G. Sosso, J. Behler, and M. Bernasconi, "Atomistic simulations of the crystallization and aging of GeTe nanowires," *J. Phys. Chem. C*, vol. 121, no. 42, p. 23827, 2017.

[23] H. Wang, L. Zhang, J. Han, and E. Weinan, "Deepmd-kit: A deep learning package for many-body potential energy representation and molecular dynamics," *Comput. Phys. Commun.*, vol. 228, p. 178, 2018.

[24] L. Zhang, J. Han, H. Wang, R. Car, and W. E, "Deep potential molecular dynamics: A scalable model with the accuracy of quantum mechanics," *Phys. Rev. Lett.*, vol. 120, p. 143001, 2018.

[25] N. Yamada, E. Ohno, N. Akahira, K. Nishiuchi, K. Nagata, and M. Takao, "High speed overwritable phase change optical disk material," *Jpn J Appl Phys*, vol. 26, no. S4, p. 61, 1987.

[26] N. Yamada, "Origin, secret, and application of the ideal phase-change material GeSbTe," *Phys. Status Solidi B*, vol. 249, no. 10, p. 1837, 2012.

[27] A. Lacaita, "Phase change memories: State-of-the-art, challenges and perspectives," *Solid State Electron*, vol. 50, no. 1, p. 24, 2006.

[28] A. L. Lacaita and D. J. Wouters, "Phase-change memories," *Phys. Status Solidi A*, vol. 205, no. 10, p. 2281, 2008.

[29] S. R. Ovshinsky, "Reversible electrical switching phenomena in disordered structures," *Phys. Rev. Lett.*, vol. 21, p. 1450, 1968.

[30] N. Yamada, E. Ohno, K. Nishiuchi, N. Akahira, and M. Takao, "Rapid-phase transitions of GeTe-Sb_2Te_3 pseudobinary amorphous thin films for an optical disk memory," *J. Appl. Phys.*, vol. 69, no. 5, p. 2849, 1991.

[31] S. Lai and T. Lowrey, "OUM - A 180 nm nonvolatile memory cell element technology for stand alone and embedded applications," in *International Electron Devices Meeting. Technical Digest (Cat. No.01CH37224)*, p. 36.5.1, 2001.

[32] R. Neale, D. Nelson, and G. E. Moore, "Nonvolatile and reprogrammable, the read-mostly memory is here," *Electron.*, vol. 43, no. 20, p. 56, 1970.

[33] A. L. Lacaita and A. Redaelli, "The race of phase change memories to nanoscale storage and applications," *Microelectron. Eng.*, vol. 109, p. 351, 2013.

[34] S. W. Fong, C. M. Neumann, and H.-S. P. Wong, "Phase-change memory—towards a storage-class memory," *IEEE Transactions on Electron Devices*, vol. 64, no. 11, p. 4374, 2017.

[35] F. Rao, K. Ding, Y. Zhou, Y. Zheng, M. Xia, S. Lv, Z. Song, S. Feng, I. Ronneberger, R. Mazzarello, *et al.*, "Reducing the stochasticity of crystal nucleation to enable subnanosecond memory writing," *Science*, vol. 358, no. 6369, p. 1423, 2017.

[36] D.-H. Kwon, K. M. Kim, J. H. Jang, J. M. Jeon, M. H. Lee, G. H. Kim, X.-S. Li, G.-S. Park, B. Lee, S. Han, *et al.*, "Atomic structure of conducting nanofilaments in TiO_2 resistive switching memory," *Nat. Nanotechnol.*, vol. 5, no. 2, p. 148, 2010.

[37] M. Prezioso, F. Merrikh-Bayat, B. Hoskins, G. C. Adam, K. K. Likharev, and D. B. Strukov, "Training and operation of an integrated neuromorphic network based on metal-oxide memristors," *Nature*, vol. 521, no. 7550, p. 61, 2015.

[38] S. Mangin, D. Ravelosona, J. Katine, M. Carey, B. Terris, and E. E. Fullerton, "Current-induced magnetization reversal in nanopillars with perpendicular anisotropy," *Nat. Mater*, vol. 5, no. 3, p. 210, 2006.

[39] S. Zhang, Y. Zhao, P. Li, J. Yang, S. Rizwan, J. Zhang, J. Seidel, T. Qu, Y. Yang, Z. Luo, *et al.*, "Electric-field control of nonvolatile magnetization in $Co_{40}Fe_{40}B_{20}/Pb(Mg_{1/3}Nb_{2/3})_(0.7)Ti_{0.3}O_3$ structure at room temperature," *Phys. Rev. Lett.*, vol. 108, no. 13, p. 137203, 2012.

[40] B. Park, B. Kang, S. Bu, T. Noh, J. Lee, and W. Jo, "Lanthanum-substituted bismuth titanate for use in non-volatile memories," *Nature*, vol. 401, no. 6754, p. 682, 1999.

[41] A. Chanthbouala, V. Garcia, R. O. Cherifi, K. Bouzehouane, S. Fusil, X. Moya, S. Xavier, H. Yamada, C. Deranlot, N. D. Mathur, *et al.*, "A ferroelectric memristor," *Nat. Mater*, vol. 11, no. 10, p. 860, 2012.

[42] H.-S. P. Wong and S. Salahuddin, "Memory leads the way to better computing," *Nat. Nanotechnol.*, vol. 10, no. 3, p. 191, 2015.

[43] T. Rueckes, K. Kim, E. Joselevich, G. Y. Tseng, C.-L. Cheung, and C. M. Lieber, "Carbon nanotube-based nonvolatile random access memory for molecular computing," *Science*, vol. 289, no. 5476, p. 94, 2000.

[44] C. Liu, X. Yan, X. Song, S. Ding, D. W. Zhang, and P. Zhou, "A semi-floating gate memory based on van der waals heterostructures for quasi-non-volatile applications," *Nat. Nanotechnol.*, vol. 13, no. 5, p. 404, 2018.

[45] J. Ouyang, C.-W. Chu, C. R. Szmanda, L. Ma, and Y. Yang, "Programmable polymer thin film and non-volatile memory device," *Nat. Mater*, vol. 3, no. 12, p. 918, 2004.

[46] C. Mead, "Neuromorphic electronic systems," *Proceedings of the IEEE*, vol. 78, no. 10, p. 1629, 1990.

[47] J. J. Yang, D. B. Strukov, and D. R. Stewart, "Memristive devices for computing," *Nat. Nanotechnol.*, vol. 8, no. 1, p. 13, 2013.

[48] P. A. Merolla, J. V. Arthur, R. Alvarez-Icaza, A. S. Cassidy, J. Sawada, F. Akopyan, B. L. Jackson, N. Imam, C. Guo, Y. Nakamura, *et al.*, "A million spiking-neuron integrated circuit with a scalable communication network and interface," *Science*, vol. 345, no. 6197, p. 668, 2014.

[49] M. A. Zidan, J. P. Strachan, and W. D. Lu, "The future of electronics based on memristive systems," *Nat. Electron.*, vol. 1, no. 1, p. 22, 2018.

[50] T. Tuma, A. Pantazi, M. Le Gallo, A. Sebastian, and E. Eleftheriou, "Stochastic phase-change neurons," *Nat. Nanotechnol.*, vol. 11, no. 8, p. 693, 2016.

[51] D. Kuzum, R. G. Jeyasingh, B. Lee, and H.-S. P. Wong, "Nanoelectronic programmable synapses based on phase change materials for brain-inspired computing," *Nano Lett.*, vol. 12, no. 5, p. 2179, 2012.

[52] Y. Li, L. Xu, Y.-P. Zhong, Y.-X. Zhou, S.-J. Zhong, Y.-Z. Hu, L. O. Chua, and X.-S. Miao, "Associative learning with temporal contiguity in a memristive circuit for large-scale neuromorphic networks," *Adv. Electron. Mater.*, vol. 1, no. 8, p. 1500125, 2015.

[53] E. R. Meinders, A. V. Mijiritskii, L. van Pieterson, and M. Wuttig, *Optical data storage: phase-change media and recording*, vol. 4. Springer Science & Business Media, 2006.

[54] J. Goldak, C. S. Barrett, D. Innes, and W. Youdelis, "Structure of α-GeTe," *J Chem. Phys.*, vol. 44, no. 9, p. 3323, 1966.

[55] T. Chattopadhyay, J. X. Boucherle, and H. G. vonSchnering, "Neutron diffraction study on the structural phase transition in GeTe," *J Phys C Solid State Phys*, vol. 20, no. 10, p. 1431, 1987.

[56] P. Fons, A. V. Kolobov, M. Krbal, J. Tominaga, K. S. Andrikopoulos, S. N. Yannopoulos, G. A. Voyiatzis, and T. Uruga, "Phase transition in crystalline GeTe: Pitfalls of averaging effects," *Phys. Rev. B*, vol. 82, p. 155209, 2010.

[57] T. L. Anderson and H. B. Krause, "Refinement of the Sb_2Te_3 and Sb_2Te_2Se structures and their relationship to nonstoichiometric $Sb_2Te_{3-y}Se_y$ compounds," *Acta Crystallogr. B*, vol. 30, no. 5, p. 1307, 1974.

[58] K. Li, L. Peng, L. Zhu, J. Zhou, and Z. Sun, "Vacancy-mediated electronic localization and phase transition in cubic Sb_2Te_3," *Mater Sci Semicond Process*, vol. 135, p. 106052, 2021.

[59] T. Matsunaga, N. Yamada, and Y. Kubota, "Structures of stable and metastable $Ge_2Sb_2Te_5$, an intermetallic compound in GeTe-Sb_2Te_3 pseudobinary systems," *Acta Crystallogr. B*, vol. 60, no. 6, p. 685, 2004.

[60] I. Petrov, R. Imamov, and Z. Pinsker, "Electron-diffraction determination of the structures of $Ge_2Sb_2Te_5$ and $GeSb_4Te_7$," *Sov. Phys. Crystallogr.*, vol. 13, no. 3, p. 339, 1968.

[61] B. Kooi and J. T. M. De Hosson, "Electron diffraction and high-resolution transmission electron microscopy of the high temperature crystal structures of $Ge_xSb_2Te_{3+x}$ (x= 1, 2, 3) phase change material," *J. Appl. Phys.*, vol. 92, no. 7, p. 3584, 2002.

[62] G. Sosso, S. Caravati, C. Gatti, S. Assoni, and M. Bernasconi, "Vibrational properties of hexagonal $Ge_2Sb_2Te_5$ from first principles," *J. Phys. Condens. Matter*, vol. 21, no. 24, p. 245401, 2009.

[63] A. V. Kolobov, P. Fons, A. I. Frenkel, A. L. Ankudinov, J. Tominaga, and T. Uruga, "Understanding the phase-change mechanism of rewritable optical media," *Nat. Mater*, vol. 3, no. 10, p. 703, 2004.

[64] Y. M. Y. Maeda and M. W. M. Wakagi, "Ge K-edge extended X-ray absorption fine structure study of the local structure of amorphous GeTe and the crystallization," *Jpn J Appl Phys*, vol. 30, no. 1R, p. 101, 1991.

[65] K. Hirota, K. Nagino, and G. Ohbayashi, "Local structure of amorphous GeTe and PdGeSbTe alloy for phase change optical recording," *J. Appl. Phys.*, vol. 82, no. 1, p. 65, 1997.

[66] A. Kolobov, P. Fons, J. Tominaga, A. Ankudinov, S. Yannopoulos, and K. Andrikopoulos, "Crystallization-induced short-range order changes in amorphous GeTe," *J. Phys. Condens. Matter*, vol. 16, no. 44, p. S5103, 2004.

[67] S. Kohara, K. Kato, S. Kimura, H. Tanaka, T. Usuki, K. Suzuya, H. Tanaka, Y. Moritomo, T. Matsunaga, N. Yamada, *et al.*, "Structural basis for the fast phase change of $Ge_2Sb_2Te_5$: Ring statistics analogy between the crystal and amorphous states," *Appl. Phys. Lett.*, vol. 89, no. 20, p. 201910, 2006.

[68] M. Krbal, A. Kolobov, P. Fons, J. Tominaga, S. Elliott, J. Hegedus, and T. Uruga, "Intrinsic complexity of the melt-quenched amorphous $Ge_2Sb_2Te_5$ memory alloy," *Phys. Rev. B*, vol. 83, no. 5, p. 054203, 2011.

[69] J. Akola and R. Jones, "Density functional study of amorphous, liquid and crystalline $Ge_2Sb_2Te_5$: homopolar bonds and/or ab alternation?," *J. Phys. Condens. Matter*, vol. 20, no. 46, p. 465103, 2008.

[70] S. Caravati, M. Bernasconi, T. Kühne, M. Krack, and M. Parrinello, "First-principles study of crystalline and amorphous $Ge_2Sb_2Te_5$ and the effects of stoichiometric defects," *J. Phys. Condens. Matter*, vol. 21, no. 25, p. 255501, 2009.

[71] V. L. Deringer, W. Zhang, M. Lumeij, S. Maintz, M. Wuttig, R. Mazzarello, and R. Dronskowski, "Bonding nature of local structural motifs in amorphous GeTe," *Angew. Chem. Int. Ed.*, vol. 53, no. 40, p. 10817, 2014.

[72] J. Kalikka, J. Akola, J. Larrucea, and R. O. Jones, "Nucleus-driven crystallization of amorphous $Ge_2Sb_2Te_5$: A density functional study," *Phys. Rev. B*, vol. 86, no. 14, p. 144113, 2012.

[73] I. Ronneberger, W. Zhang, H. Eshet, and R. Mazzarello, "Crystallization properties of the $Ge_2Sb_2Te_5$ phase-change compound from advanced simulations," *Adv. Funct. Mater.*, vol. 25, no. 40, p. 6407, 2015.

[74] D. Lencer, M. Salinga, M. Wuttig, D. Lencer, M. Salinga, and M. Wuttig, "Design rules for phase-change materials in data storage applications," *Adv. Mater.*, vol. 23, p. 2030, 2011.

[75] B.-S. Lee, J. R. Abelson, S. G. Bishop, D.-H. Kang, B.-k. Cheong, and K.-B. Kim, "Investigation of the optical and electronic properties of $Ge_2Sb_2Te_5$ phase change material in its amorphous, cubic, and hexagonal phases," *J. Appl. Phys.*, vol. 97, no. 9, p. 093509, 2005.

[76] J.-J. Kim, K. Kobayashi, E. Ikenaga, M. Kobata, S. Ueda, T. Matsunaga, K. Kifune, R. Kojima, and N. Yamada, "Electronic structure of amorphous and crystalline $(GeTe)_{1-x}(Sb_2Te_3)_x$ investigated using hard x-ray photoemission spectroscopy," *Phys. Rev. B*, vol. 76, no. 11, p. 115124, 2007.

[77] B. Huang and J. Robertson, "Bonding origin of optical contrast in phase-change memory materials," *Phys. Rev. B*, vol. 81, p. 081204, 2010.

[78] M. Wuttig, V. L. Deringer, X. Gonze, C. Bichara, and J.-Y. Raty, "Incipient metals: functional materials with a unique bonding mechanism," *Adv. Mater.*, vol. 30, no. 51, p. 1803777, 2018.

[79] M. Zhu, O. Cojocaru-Mirédin, A. M. Mio, J. Keutgen, M. Küpers, Y. Yu, J.-Y. Cho, R. Dronskowski, and M. Wuttig, "Unique bond breaking in crystalline phase change materials and the quest for metavalent bonding," *Adv. Mater.*, vol. 30, no. 18, p. 1706735, 2018.

[80] J.-Y. Raty, M. Schumacher, P. Golub, V. L. Deringer, C. Gatti, and M. Wuttig, "A quantum-mechanical map for bonding and properties in solids," *Adv. Mater.*, vol. 31, no. 3, p. 1806280, 2019.

[81] B. J. Kooi and M. Wuttig, "Chalcogenides by design: Functionality through metavalent bonding and confinement," *Adv. Mater.*, vol. 32, no. 21, p. 1908302, 2020.

[82] T. H. Lee and S. R. Elliott, "Chemical bonding in chalcogenides: the concept of multicenter hyperbonding," *Adv. Mater.*, vol. 32, no. 28, p. 2000340, 2020.

[83] T. H. Lee and S. R. Elliott, "Multi-center hyperbonding in phase-change materials," *Phys. Status Solidi RRL*, vol. 15, no. 3, p. 2000516, 2021.

[84] T. Lee and S. Elliott, "Hypervalency in amorphous chalcogenides," *Nat. Commun.*, vol. 13, no. 1, p. 1, 2022.

[85] H. W. Wilson, "Xx. on the velocity of solidification and viscosity of supercooled liquids," *Lond. Edinb. Dublin philos. mag. j. sci.*, vol. 50, no. 303, p. 238, 1900.

[86] P. G. Debenedetti, "Metastable liquids," in *Metastable Liquids*, Princeton university press, 2021.

[87] A. Onuki, *Phase transition dynamics*. Cambridge University Press, 2002.

[88] V. I. Kalikmanov, "Classical nucleation theory," in *Nucleation theory*, p. 17, Springer, 2013.

[89] J. Orava, A. á. Greer, B. Gholipour, D. Hewak, and C. Smith, "Characterization of supercooled liquid $Ge_2Sb_2Te_5$ and its crystallization by ultrafast-heating calorimetry," *Nat. Mater*, vol. 11, no. 4, p. 279, 2012.

[90] T. H. Lee and S. R. Elliott, "Ab initio computer simulation of the early stages of crystallization: Application to $Ge_2Sb_2Te_5$ phase-change materials," *Phys. Rev. Lett.*, vol. 107, p. 145702, 2011.

[91] T. H. Lee and S. R. Elliott, "Structural role of vacancies in the phase transition of $Ge_2Sb_2Te_5$ memory materials," *Phys. Rev. B*, vol. 84, p. 094124, 2011.

[92] J. Kalikka, J. Akola, and R. Jones, "Simulation of crystallization in $Ge_2Sb_2Te_5$: A memory effect in the canonical phase-change material," *Phys. Rev. B*, vol. 90, no. 18, p. 184109, 2014.

[93] J. Kalikka, J. Akola, and R. Jones, "Crystallization processes in the phase change material $Ge_2Sb_2Te_5$: Unbiased density functional/molecular dynamics simulations," *Phys. Rev. B*, vol. 94, no. 13, p. 134105, 2016.

[94] I. Ronneberger, W. Zhang, and R. Mazzarello, "Crystal growth of $Ge_2Sb_2Te_5$ at high temperatures," *MRS Communications*, vol. 8, no. 3, p. 1018, 2018.

[95] P. Cappelletti, R. Annunziata, F. Arnaud, F. Disegni, A. Maurelli, and P. Zuliani, "Phase change memory for automotive grade embedded NVM applications," *J. Phys. D*, vol. 53, no. 19, p. 193002, 2020.

[96] A. Kiouseloglou, G. Navarro, V. Sousa, A. Persico, A. Roule, A. Cabrini, G. Torelli, S. Maitrejean, G. Reimbold, B. De Salvo, F. Clermidy, and L. Perniola, "A novel programming technique to boost low-resistance state performance in ge-rich gst phase change memory," *IEEE Transactions on Electron Devices*, vol. 61, no. 5, p. 1246, 2014.

[97] F. Arnaud, P. Ferreira, F. Piazza, A. Gandolfo, P. Zuliani, P. Mattavelli, E. Gomiero, G. Samanni, J. Jasse, C. Jahan, J. P. Reynard, R. Berthelon, O. Weber, A. Villaret, B. Dumont, J. C. Grenier, R. Ranica, C. Gallon, C. Boccaccio, A. Souhaite, L. Desvoivres, D. Ristoiu, L. Favennec, V. Caubet, S. Delmedico, N. Cherault, R. Beneyton, S. Chouteau, P. O. Sassoulas, L. Clement, P. Boivin, D. Turgis, F. Disegni, J. L. Ogier, X. Federspiel, O. Kermarrec, M. Molgg, A. Viscuso, R. Annunziata, A. Maurelli, P. Cappelletti, and E. Ciantar, "High density embedded PCM cell in 28nm FDSOI technology for automotive microcontroller applications," in *2020 IEEE International Electron Devices Meeting (IEDM)*, p. 24.2.1, 2020.

[98] V. Sousa, G. Navarro, N. Castellani, M. Coue, O. Cueto, C. Sabbione, P. Noe, L. Perniola, S. Blonkowski, P. Zuliani, *et al.*, "Operation fundamentals in 12mb phase change memory based on innovative Ge-rich GST materials featuring high reliability performance," in *2015 Symposium on VLSI Technology (VLSI Technology)*, p. T98, IEEE, 2015.

[99] E. Palumbo, P. Zuliani, M. Borghi, and R. Annunziata, "Forming operation in Ge-rich $Ge_xSb_yTe_z$ phase change memories," *Solid State Electron*, vol. 133, p. 38, 2017.

[100] G. Navarro, M. Coué, A. Kiouseloglou, P. Noé, F. Fillot, V. Delaye, A. Persico, A. Roule, M. Bernard, C. Sabbione, *et al.*, "Trade-off between set and data retention performance thanks to innovative materials for phase-change memory," in *2013 IEEE International Electron Devices Meeting*, p. 21, IEEE, 2013.

[101] M. A. Luong, M. Agati, N. Ratel Ramond, J. Grisolia, Y. Le Friec, D. Benoit, and A. Claverie, "On some unique specificities of Ge-rich

GeSbTe phase-change material alloys for nonvolatile embedded-memory applications," *Phys. Status Solidi RRL*, vol. 15, no. 3, p. 2000471, 2021.

[102] S. Privitera, V. Sousa, C. Bongiorno, G. Navarro, C. Sabbione, E. Carria, and E. Rimini, "Atomic diffusion in laser irradiated ge rich GeSbTe thin films for phase change memory applications," *J. Phys. D*, vol. 51, no. 14, p. 145103, 2018.

[103] M. Agati, M. Vallet, S. Joulié, D. Benoit, and A. Claverie, "Chemical phase segregation during the crystallization of Ge-rich GeSbTe alloys," *J. Mater. Chem. C*, vol. 7, pp. 8720–8729, 2019.

[104] S. Privitera, I. López García, C. Bongiorno, V. Sousa, M. Cyrille, G. Navarro, C. Sabbione, E. Carria, and E. Rimini, "Crystallization properties of melt-quenched Ge-rich GeSbTe thin films for phase change memory applications," *J. Appl. Phys.*, vol. 128, no. 15, p. 155105, 2020.

[105] Y.-H. Lee, P. Liao, V. Hou, D. Heh, C.-H. Nien, W.-H. Kuo, G. T. Chen, S.-M. Yu, Y.-S. Chen, J.-Y. Wu, X. Bao, and C. H. Diaz, "Composition segregation of Ge-rich GST and its effect on reliability," in *2021 IEEE International Reliability Physics Symposium (IRPS)*, p. 1, 2021.

[106] E. Rahier, S. Ran, N. Ratel Ramond, S. Ma, L. Calmels, S. Saha, C. Mocuta, D. Benoit, Y. Le Friec, M. A. Luong, *et al.*, "Crystallization of Ge-rich GeSbTe alloys: The riddle is solved," *ACS Appl. Electron. Mater.*, 2022.

[107] B. Kooi, W. Groot, and J. T. M. De Hosson, "In situ transmission electron microscopy study of the crystallization of $Ge_2Sb_2Te_5$," *J. Appl. Phys.*, vol. 95, no. 3, p. 924, 2004.

[108] L. Sun, Y.-X. Zhou, X.-D. Wang, Y.-H. Chen, V. L. Deringer, R. Mazzarello, and W. Zhang, "Ab initio molecular dynamics and materials design for embedded phase-change memory," *Npj Comput. Mater.*, vol. 7, no. 1, p. 1, 2021.

[109] O. Abou El Kheir, D. Dragoni, and M. Bernasconi, "Density functional simulations of decomposition pathways of Ge-rich GeSbTe alloys for phase change memories," *Phys. Rev. Mater.*, vol. 5, p. 095004, 2021.

[110] M. Born and R. Oppenheimer, "Zur quantentheorie der molekeln," *Ann. Phys.*, vol. 389, no. 20, p. 457, 1927.

[111] P. Hohenberg and W. Kohn, "Inhomogeneous electron gas," *Phys. Rev.*, vol. 136, p. B864, 1964.

[112] W. Kohn and L. J. Sham, "Self-consistent equations including exchange and correlation effects," *Phys. Rev.*, vol. 140, p. A1133, 1965.

[113] D. C. Langreth and M. J. Mehl, "Beyond the local-density approximation in calculations of ground-state electronic properties," *Phys. Rev. B*, vol. 28, p. 1809, 1983.

[114] A. D. Becke, "Density-functional exchange-energy approximation with correct asymptotic behavior," *Phys. Rev. A*, vol. 38, p. 3098, 1988.

[115] J. P. Perdew, K. Burke, and M. Ernzerhof, "Generalized gradient approximation made simple," *Phys. Rev. Lett.*, vol. 77, p. 3865, 1996.

[116] D. R. Hamann, M. Schlüter, and C. Chiang, "Norm-conserving pseudopotentials," *Phys. Rev. Lett.*, vol. 43, p. 1494, 1979.

[117] G. Lippert, J. Hutter, and M. Parrinello, "A hybrid gaussian and plane wave density functional scheme," *Mol. Phys.*, vol. 92, no. 3, p. 477, 1997.

[118] S. Goedecker and M. Teter, "Separable dual-space Gaussian pseudopotentials," *Phys. Rev. B Condens. Matter*, vol. 54, p. 1703, 1996.

[119] M. Krack, "Pseudopotentials for H to Kr optimized for gradient-corrected exchange-correlation functionals," *Theor. Chem. Acc.*, vol. 114, p. 145, 2005.

[120] H. J. Monkhorst and J. D. Pack, "Special points for brillouin-zone integrations," *Phys. Rev. B*, vol. 13, p. 5188, 1976.

[121] S. Go, H. Bilz, and M. Cardona, "Bond charge, bond polarizability, and phonon spectra in semiconductors," *Phys. Rev. Lett.*, vol. 34, p. 580, 1975.

[122] G. C. Sosso, S. Caravati, R. Mazzarello, and M. Bernasconi, "Raman spectra of cubic and amorphous $Ge_2Sb_2Te_5$ from first principles," *Phys. Rev. B*, vol. 83, p. 134201, 2011.

[123] D. Frenkel and B. Smit, *Understanding molecular simulation: from algorithms to applications*, vol. 1. Elsevier, 2001.

[124] W. C. Swope, H. C. Andersen, P. H. Berens, and K. R. Wilson, "A computer simulation method for the calculation of equilibrium constants for the formation of physical clusters of molecules: Application to small water clusters," *J Chem. Phys.*, vol. 76, no. 1, p. 637, 1982.

[125] K. Hornik, M. Stinchcombe, and H. White, "Multilayer feedforward networks are universal approximators," *Neural Netw.*, vol. 2, no. 5, p. 359, 1989.

[126] W. S. McCulloch and W. Pitts, "A logical calculus of the ideas immanent in nervous activity," *Bull. Math. Biol.*, vol. 5, no. 4, p. 115, 1943.

[127] A. P. Bartók, M. C. Payne, R. Kondor, and G. Csányi, "Gaussian approximation potentials: The accuracy of quantum mechanics, without the electrons," *Phys. Rev. Lett.*, vol. 104, p. 136403, 2010.

[128] W. Press, S. Teukolsky, W. Vetterling, and B. Flannery, *Numerical Recipes 3rd Edition: The Art of Scientific Computing*. Cambridge University Press, 2007.

[129] J. Ischtwan and M. A. Collins, "Molecular potential energy surfaces by interpolation," *J Chem. Phys.*, vol. 100, no. 11, p. 8080, 1994.

[130] D. P. Kingma and J. Ba, "Adam: A method for stochastic optimization," *arXiv*, 2014.

[131] K. He, X. Zhang, S. Ren, and J. Sun, "Deep residual learning for image recognition," in *2016 IEEE Conference on Computer Vision and Pattern Recognition (CVPR)*, p. 770, 2016.

[132] T. B. Blank, S. D. Brown, A. W. Calhoun, and D. J. Doren, "Neural network models of potential energy surfaces," *J Chem. Phys.*, vol. 103, no. 10, p. 4129, 1995.

[133] S. Hobday, R. Smith, and J. Belbruno, "Applications of neural networks to fitting interatomic potential functions," *Model Simul Mat Sci Eng*, vol. 7, p. 397, 1999.

[134] J. Tersoff, "Empirical interatomic potential for carbon, with applications to amorphous carbon," *Phys. Rev. Lett.*, vol. 61, p. 2879, 1988.

[135] A. P. Bartók, R. Kondor, and G. Csányi, "On representing chemical environments," *Phys. Rev. B*, vol. 87, p. 184115, 2013.

[136] J. Behler, "Perspective: Machine learning potentials for atomistic simulations," *J Chem. Phys.*, vol. 145, no. 17, p. 170901, 2016.

[137] L. Zhang, J. Han, H. Wang, W. A. Saidi, R. Car, and W. E, "End-to-end symmetry preserving inter-atomic potential energy model for finite and extended systems," *Arxiv*, 2018.

[138] D. Lu, H. Wang, M. Chen, L. Lin, R. Car, E. Weinan, W. Jia, and L. Zhang, "86 pflops deep potential molecular dynamics simulation of 100 million atoms with ab initio accuracy," *Comput. Phys. Commun.*, vol. 259, p. 107624, 2021.

[139] X. Wang, Y. Wang, L. Zhang, F. Dai, and H. Wang, "A tungsten deep neural-network potential for simulating mechanical property degradation under fusion service environment," *Nucl. Fusion*, vol. 62, no. 12, p. 126013, 2022.

[140] H. Weyl, *The classical groups: their invariants and representations*. Princeton university press, 1946.

[141] C. Chèze, F. Righi Riva, G. Di Bella, E. Placidi, S. Prili, M. Bertelli, A. Diaz Fattorini, M. Longo, R. Calarco, M. Bernasconi, *et al.*, "Interface formation during the growth of phase change material heterostructures based on Ge-rich Ge-Sb-Te alloys," *Nanomaterials*, vol. 12, no. 6, p. 1007, 2022.

[142] S. Gabardi, S. Caravati, M. Bernasconi, and M. Parrinello, "Density functional simulations of Sb-rich GeSbTe phase change alloys," *J. Phys. Condens. Matter*, vol. 24, no. 38, p. 385803, 2012.

[143] W. K. Njoroge, H.-W. Wöltgens, and M. Wuttig, "Density changes upon crystallization of $Ge_2Sb_{2.04}Te_{4.74}$ films," *J. Vac. Sci. Technol. A*, vol. 20, no. 1, p. 230, 2002.

[144] J. Hutter, M. Iannuzzi, F. Schiffmann, and J. Vandevondele, "CP2k: Atomistic simulations of condensed matter systems," *Wiley Interdiscip. Rev. Comput. Mol. Sci.*, vol. 4, 15, 2014.

[145] S. Grimme, J. Antony, S. Ehrlich, and H. Krieg, "A consistent and accurate ab initio parametrization of density functional dispersion correction (DFT-D) for the 94 elements H-Pu," *J. Chem. Phys.*, vol. 132, 154104, 2010.

[146] H. Weber, M. Schumacher, P. Jóvári, Y. Tsuchiya, W. Skrotzki, R. Mazzarello, and I. Kaban, "Experimental and ab initio molecular dynamics study of the structure and physical properties of liquid GeTe," *Phys. Rev. B*, vol. 96, p. 054204, 2017.

[147] M. Schumacher, H. Weber, P. Jóvári, Y. Tsuchiya, T. G. Youngs, I. Kaban, and R. Mazzarello, "Structural, electronic and kinetic properties of the phase-change material $Ge_2Sb_2Te_5$ in the liquid state," *Sci. Rep.*, vol. 6, no. 1, p. 1, 2016.

[148] F. Birch, "Finite elastic strain of cubic crystals," *Phys. Rev.*, vol. 71, p. 809, 1947.

[149] P. Giannozzi, S. Baroni, N. Bonini, M. Calandra, R. Car, C. Cavazzoni, D. Ceresoli, G. L. Chiarotti, M. Cococcioni, I. Dabo, *et al.*, "Quantum espresso: a modular and open-source software project for quantum simulations of materials," *J. Phys. Condens. Matter*, vol. 21, no. 39, p. 395502, 2009.

[150] J. R. Errington and P. G. Debenedetti, "Relationship between structural order and the anomalies of liquid water," *Nature*, vol. 409, no. 6818, p. 318, 2001.

[151] D. S. Franzblau, "Computation of ring statistics for network models of solids," *Phys. Rev. B*, vol. 44, p. 4925, 1991.

[152] M. Luo and M. Wuttig, "The dependence of crystal structure of Te-based phase-change materials on the number of valence electrons," *Adv. Mater.*, vol. 16, no. 5, p. 439, 2004.

[153] A. V. Krukau, O. A. Vydrov, A. F. Izmaylov, and G. E. Scuseria, "Influence of the exchange screening parameter on the performance of screened hybrid functionals," *J Chem. Phys.*, vol. 125, no. 22, p. 224106, 2006.

[154] A. Zunger, S.-H. Wei, L. G. Ferreira, and J. E. Bernard, "Special quasirandom structures," *Phys. Rev. Lett.*, vol. 65, p. 353, 1990.

[155] O. Abou El Kheir and M. Bernasconi, "High-throughput calculations on the decomposition reactions of off-stoichiometry GeSbTe alloys for embedded memories," *Nanomaterials*, vol. 11, no. 9, p. 2382, 2021.

[156] D. Hildebrandt and D. Glasser, "Predicting phase and chemical equilibrium using the convex hull of the Gibbs free energy," *Chem. Eng. J. Biochem. Eng. J.*, vol. 54, no. 3, p. 187, 1994.

[157] S. Curtarolo, D. Morgan, and G. Ceder, "Accuracy of ab initio methods in predicting the crystal structures of metals: A review of 80 binary alloys," *Calphad*, vol. 29, no. 3, p. 163, 2005.

[158] C. Nyshadham, C. Oses, J. E. Hansen, I. Takeuchi, S. Curtarolo, and G. L. Hart, "A computational high-throughput search for new ternary superalloys," *Acta Mater.*, vol. 122, p. 438, 2017.

[159] T. Matsunaga, R. Kojima, N. Yamada, K. Kifune, Y. Kubota, and M. Takata, "Structural features of $Ge_1Sb_4Te_7$, an intermetallic compound in the GeTe-Sb_2Te_3 homologous series," *Chem. Mater.*, vol. 20, no. 18, p. 5750, 2008.

[160] T. Matsunaga, H. Morita, R. Kojima, N. Yamada, K. Kifune, Y. Kubota, Y. Tabata, J.-J. Kim, M. Kobata, E. Ikenaga, *et al.*, "Structural characteristics of GeTe-rich GeTe-Sb_2Te_3 pseudobinary metastable crystals," *J. Appl. Phys.*, vol. 103, no. 9, p. 093511, 2008.

[161] K. Govaerts, M. Sluiter, B. Partoens, and D. Lamoen, "Stability of Sb-Te layered structures: First-principles study," *Phys. Rev. B*, vol. 85, no. 14, p. 144114, 2012.

[162] C. B. Barber, D. P. Dobkin, and H. Huhdanpaa, "The quickhull algorithm for convex hulls," *ACM Transactions on Mathematical Software (TOMS)*, vol. 22, no. 4, p. 469, 1996.

[163] V. Evang and R. Mazzarello, "Point defects in disordered and stable GeSbTe phase-change materials," *Mater Sci Semicond Process*, vol. 133, p. 105948, 2021.

[164] D. T. Yimam, A. Van Der Ree, O. Abou El Kheir, J. Momand, M. Ahmadi, G. Palasantzas, M. Bernasconi, and B. J. Kooi, "Phase separation in Ge-rich GeSbTe at different length scales: Melt-quenched bulk versus annealed thin films," *Nanomaterials*, vol. 12, no. 10, p. 1717, 2022.

[165] M. Agati, M. Vallet, S. Joulié, D. Benoit, and A. Claverie, "Chemical phase segregation during the crystallization of Ge-rich GeSbTe alloys," *J. Mater. Chem. C*, vol. 7, no. 28, p. 8720, 2019.

[166] J. Kalikka, J. Akola, and R. O. Jones, "Crystallization processes in the phase change material $Ge_2Sb_2Te_5$: Unbiased density functional molecular dynamics simulations," *Phys. Rev. B*, vol. 94, p. 134105, 2016.

[167] S. Cecchi, I. Lopez Garcia, A. M. Mio, E. Zallo, O. Abou El Kheir, R. Calarco, M. Bernasconi, G. Nicotra, and S. M. Privitera, "Crystallization and electrical properties of Ge-rich GeSbTe alloys," *Nanomaterials*, vol. 12, no. 4, p. 631, 2022.

[168] E. P. Donovan, F. Spaepen, D. Turnbull, J. Poate, and D. Jacobson, "Calorimetric studies of crystallization and relaxation of amorphous Si and Ge prepared by ion implantation," *J. Appl. Phys.*, vol. 57, no. 6, p. 1795, 1985.

[169] S. Bordas, M. Clavaguer-Mora, B. Legendre, and C. Hancheng, "Phase diagram of the ternary system Ge-Sb-Te: Ii. the subternary Ge-GeTe-Sb_2Te_3-Sb," *Thermochim. Acta*, vol. 107, p. 239, 1986.

[170] F. C. Mocanu, K. Konstantinou, T. H. Lee, N. Bernstein, V. L. Deringer, G. Csányi, and S. R. Elliott, "Modeling the phase-change memory material, $Ge_2Sb_2Te_5$, with a machine-learned interatomic potential," *J. Phys. Chem. B*, vol. 122, no. 38, p. 8998, 2018.

[171] L. Bonati and M. Parrinello, "Silicon liquid structure and crystal nucleation from ab initio deep metadynamics," *Phys. Rev. Lett.*, vol. 121, no. 26, p. 265701, 2018.

[172] H. Niu, L. Bonati, P. M. Piaggi, and M. Parrinello, "Ab initio phase diagram and nucleation of gallium," *Nat. Commun.*, vol. 11, no. 1, p. 1, 2020.

[173] A. P. Thompson, H. M. Aktulga, R. Berger, D. S. Bolintineanu, W. M. Brown, P. S. Crozier, P. J. in 't Veld, A. Kohlmeyer, S. G. Moore, T. D. Nguyen, R. Shan, M. J. Stevens, J. Tranchida, C. Trott, and S. J. Plimpton, "LAMMPS - a flexible simulation tool for particle-based materials modeling at the atomic, meso, and continuum scales," *Comp. Phys. Comm.*, vol. 271, p. 108171, 2022.

[174] M. Rizzi, N. Ciocchini, S. Caravati, M. Bernasconi, P. Fantini, and D. Ielmini, "Statistics of set transition in phase change memory (PCM) arrays," in *2014 IEEE International Electron Devices Meeting*, p. 29.6.1, 2014.

[175] S. Grimme, "Semiempirical GGA-type density functional constructed with a long-range dispersion correction," *J. Comput. Chem.*, vol. 27, no. 15, p. 1787, 2006.

[176] H. Flores-Ruiz and M. Micoulaut, "From elemental tellurium to $Ge_2Sb_2Te_5$ melts: High temperature dynamic and relaxation properties in relationship with the possible fragile to strong transition," *J Chem. Phys.*, vol. 148, no. 3, p. 034502, 2018.

[177] Y.-X. Zhou, H.-Y. Zhang, V. L. Deringer, and W. Zhang, "Structure and dynamics of supercooled liquid $Ge_2Sb_2Te_5$ from machine-learning-driven simulations," *Phys. Status Solidi RRL*, vol. 15, no. 3, p. 2000403, 2021.

[178] M. H. Cohen and G. Grest, "Liquid-glass transition, a free-volume approach," *Phys. Rev. B*, vol. 20, no. 3, p. 1077, 1979.

[179] M. P. Allen and D. J. Tildesley, *Computer simulation of liquids*. Oxford university press, 2017.

[180] G. C. Sosso, J. Behler, and M. Bernasconi, "Breakdown of Stokes-Einstein relation in the supercooled liquid state of phase change materials," *Phys. Status Solidi B*, vol. 249, no. 10, p. 1880, 2012.

[181] S. Senkader and C. D. Wright, "Models for phase-change of $Ge_2Sb_2Te_5$ in optical and electrical memory devices," *J. Appl. Phys.*, vol. 95, no. 2, p. 504, 2004.

[182] J. Zhao, J. Hui, Z. Ye, T. Lai, M. Y. Efremov, H. Wang, and L. H. Allen, "Exploring "no man's land"—Arrhenius crystallization of thin-film phase change material at 1 000 000 K s^{-1} via nanocalorimetry," *Adv. Mater. Interfaces*, vol. 9, no. 23, p. 2200429, 2022.

[183] J. Pries, S. Wei, M. Wuttig, and P. Lucas, "Switching between crystallization from the glassy and the undercooled liquid phase in phase change material ge2sb2te5," *Advanced materials*, vol. 31, no. 39, p. 1900784, 2019.

[184] C. A. Angell, "Formation of glasses from liquids and biopolymers," *Science*, vol. 267, no. 5206, p. 1924, 1995.

[185] D. Campi, L. Paulatto, G. Fugallo, F. Mauri, and M. Bernasconi, "First-principles calculation of lattice thermal conductivity in crystalline phase change materials: GeTe, Sb_2Te_3 and $Ge_2Sb_2Te_5$," *Phys. Rev. B*, vol. 95, p. 024311, 2017.

[186] A. Togo and I. Tanaka, "First principles phonon calculations in materials science," *Scr. Mater.*, vol. 108, pp. 1–5, Nov 2015.

[187] D. G. Cahill, S. K. Watson, and R. O. Pohl, "Lower limit to the thermal conductivity of disordered crystals," *Phys. Rev. B*, vol. 46, no. 10, p. 6131, 1992.

[188] W. Mickel, S. C. Kapfer, G. E. Schröder-Turk, and K. Mecke, "Shortcomings of the bond orientational order parameters for the analysis of disordered particulate matter," *J Chem. Phys.*, vol. 138, no. 4, p. 044501, 2013.

[189] C. V. Thompson and F. Spaepen, "On the approximation of the free energy change on crystallization," *Acta Metall.*, vol. 27, no. 12, p. 1855, 1979.

[190] A. Van de Walle, P. Tiwary, M. De Jong, D. Olmsted, M. Asta, A. Dick, D. Shin, Y. Wang, L.-Q. Chen, and Z.-K. Liu, "Efficient stochastic generation of special quasirandom structures," *Calphad*, vol. 42, p. 13, 2013.

List of publications

1. Abou El Kheir, O; Dragoni, D.; and Bernasconi, M. Density functional simulations of decomposition pathways of Ge-rich GeSbTe alloys for phase change memories. Phys. Rev. Materials 5(9), 095004 (2021).

2. Abou El Kheir, O.; Bernasconi, M. High-Throughput Calculations on the Decomposition Reactions of Off-Stoichiometry GeSbTe Alloys for Embedded Memories. Nanomaterials 11(9), 2382 (2021).

3. Cecchi, S.; Lopez Garcia, I.; Mio, A.M.; Zallo, E.; Abou El Kheir, O.; Calarco, R.; Bernasconi, M.; Nicotra, G.; Privitera, S.M.S. Crystallization and Electrical Properties of Ge-Rich GeSbTe Alloys. Nanomaterials 12(9), 631 (2022).

4. Chèze, C.; Righi Riva, F.; Di Bella, G.; Placidi, E.; Prili, S.; Bertelli, M.; Diaz Fattorini, A.; Longo, M.; Calarco, R.; Bernasconi, M.; Abou El Kheir, O.; Arciprete, F. Interface Formation during the Growth of Phase Change Material Heterostructures Based on Ge-Rich Ge-Sb-Te Alloys. Nanomaterials 12(6), 1007 (2022).

5. Yimam, D.T.; Van Der Ree, A.J.T.; Abou El Kheir, O.; Momand, J.; Ahmadi, M.; Palasantzas, G.; Bernasconi, M.; Kooi, B.J. Phase Separation in Ge-Rich GeSbTe at Different Length Scales: Melt-Quenched Bulk versus Annealed Thin Films. Nanomaterials 12(10), 1717 (2022).

Acknowledgement

First and foremost, I would like to express my gratefulness to Prof. Marco Bernasconi for guiding me in this experience with his knowledge, patience and support and for the way in which he, humanely, taught me several fascinating concepts and ideas.

The part of my Phd project on the development of the NN potential for GST225 was carried out thanks to a very precious collaboration with the group of Prof. Michele Parrinello who kindly hosted me for a few months during which I had the chance to learn about Machine learning and enhanced sampling techniques. I would like to express my deep thankfulness to him and to all the great people I met on the last floor of The Laboratory in Lugano.

Next, I would like to thank Luigi Bonati ("Il professore" as Prof. Michele Parrinello would call him) for his guidance and for always being available for long calls on the phone, skype, zoom, teams and several other platforms.

Finally, I would also like to express special thanks to Chiara, Daniele, Dario, Giulia F., Giulia T., Manyi, and Sara for the long and useful conversations and for sharing with me their helpful tricks and ideas.